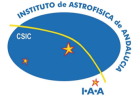


GALANTE: Photometric System and Galactic Plane Survey



**UNIVERSIDAD
DE GRANADA**



**EXCELENCIA
SEVERO
OCHOA**



Antonio Lorenzo Gutiérrez

Supervisor: Prof. Emilio J. Alfaro

Prof. Jesús Maíz Apellániz

Radioastronomy and galactic structure department, IAA-CSIC
Programa de Doctorado en Física y Ciencias del Espacio

This dissertation is submitted for the degree of

Philosophiae Doctor (PhD)

IAA-CSIC

November 2019

Editor: Universidad de Granada. Tesis Doctorales
Autor: Antonio Lorenzo Gutiérrez
ISBN: 978-84-1117-163-2
URI: <http://hdl.handle.net/10481/71854>

A mis padres y a Marta.

Agradecimientos

La consecución de esta tesis viene precedida de muchas personas que han estado y están a mi lado, haciendo posible que llegue hasta este día. No quiero olvidarme de todos vosotros que habéis estado en mi camino, haciendo que sea más fácil de lo que en realidad ha sido.

Quiero agradecer a mi familia por su apoyo en este camino, en especial a mi madre, que me ha hecho llegar hasta donde he querido. Gracias por la educación que me diste y por no ponerme trabas por nada, sin importar el esfuerzo que harás. A mi padre, que seguro estaría orgulloso de verme donde estoy. A ti también tengo mucho que agradecerte Marta, gracias por estar siempre a mi lado y entrar en mi vida, ayudándome a superar cada barrera.

No quiero olvidarme de mis compañeros del IAA, especialmente a Paco, Salva, Javi, Lali, Mayte, Alejandro, Antonio, Estefanía, Naím y Laura, con los que he compartido muchos momentos durante la tesis, escuchándome y ayudándome sin necesidad de pedíroslo. Quiero resaltar la ayuda incondicional también de César y Pique, que con una sonrisa siempre han dedicado su tiempo para resolver cualquier duda que le he planteado.

A mis amigos de siempre, en especial Juanma, Titos y Germán, que cada semana me hacían recargar las pilas para continuar.

Guardo un especial recuerdo de mi estancia en el CEFCFA (Teruel), donde los estudiantes de allí me acogieron como un integrante más. Gracias Rafa, Sidd, Gonzalo y Jonás, por estar siempre ahí. Del centro también quiero dar

las gracias a todo el staff que hicieron mi estancia más fácil, en especial a Jesús Varela por su paciencia para explicarme todo lo que no entendía.

Por supuesto agradezo a mis directores, Emilio y Jesús, la oportunidad que me dieron de realizar esta tesis, y en especial a Emilio por dedicarme su tiempo al enseñarme y ayudarme a comprender lo que desconocía.

Resumen

El trabajo plasmado en esta tesis se desarrolla dentro del proyecto GALANTE, el cual tiene como objetivo principal realizar un cartografiado fotométrico de una banda de 6° de anchura centrada en el disco galáctico norteño de la Vía Láctea de la vecindad solar, definido por $\delta \geq 0^\circ$ y $|\text{bl}| \leq 3^\circ$. El sistema fotométrico GALANTE consta de 7 bandas que cubren el rango óptico desde los 3000 Å hasta los 9000 Å con el fin de optimizar la clasificación espectral y la determinación de las variables físicas (T_{eff} , $\log(g)$, $[\text{Fe}/\text{H}]$ y extinción) para las estrellas observadas (Maíz Apellániz & Barbá, 2018a; Maíz Apellániz & Sota, 2008; Maíz Apellániz et al., 2014).

GALANTE nace a partir de la iniciativa del observatorio de Javalambre del Centro de Estudios de Física del Cosmos de Aragón (CEFCA) en Teruel para desarrollar 2 proyectos astronómicos como lo son J-PLUS (Cenarro et al., 2019) y J-PAS (Benitez et al., 2014), con 2 telescopios de 80 cm y 250 cm respectivamente, abrió un nicho para la realización del proyecto GALANTE. El objetivo principal del proyecto J-PAS es cosmológico, buscando medir el espectro de las Oscilaciones de Bariones Acústicos (BAOs) mediante estimaciones fotométricas del *redshift* (Benitez et al., 2014), mientras que J-PLUS nació con la idea de hacer un cartografiado auxiliar para calibrar J-PAS (Cenarro et al., 2018). Ya que las observaciones para el proyecto J-PLUS no pueden realizarse en las noches de Luna llena y necesitan de una calidad de cielo elevada, se pensó en realizar el proyecto GALANTE centrado en la observación de estrellas brillantes del disco galáctico. Las observaciones

para este proyecto se realizan en modo de cola, en las noches brillantes y/o con una nitidez de imagen inferior a la seleccionada por el proyecto J-PLUS. Los 7 filtros de este proyecto son una combinación de bandas intermedias y estrechas, de los cuales 4 son comunes con J-PLUS (F348M, F515N, F660N y F861M) y 3 son de diseño propio (F420N, F450N y F665N), customizados por el equipo de GALANTE. Esta selección de filtros componen un sistema óptimo para cumplir los objetivos propuesto por [Maíz Apellániz \(2017\)](#), pudiendo determinarse de manera óptima la temperatura efectiva para estrellas calientes, así como la gravedad y metalicidad (para las estrellas tardías más frías que 10 000 K). permitiéndonos discriminar entre gigantes, supergigantes, enanas y metalicidad solar o superior (SMC).

Dentro del marco del proyecto GALANTE, en esta tesis nos hemos centrado en el estudio de la asociación de Cygnus OB2 ya que estos fueron los primeros datos completos que hemos tenido para la misma. Para ello, se ha descrito el sistema fotométrico GALANTE y su caracterización, con el fin de estudiar y conocer la particularidad de sus filtros. La disposición del filtro F348M nos permite medir el continuo del salto de Balmer, mientras que, combinado con los filtros F420N y F450N, podemos medir este salto desde ambos lados, pudiendo derivar así la temperatura efectiva de las estrellas. La banda que cubre el filtro F515N se sitúa en una zona libre de líneas, siendo este similar al V de Strömgren. Los filtros F660N y F665N se utilizan para medir el continuo de H_{α} , estimando así la gravedad superficial de las estrellas, incluyendo las más calientes. Por último, el filtro F861M nos permite medir las líneas del triplete del calcio, sirviendo como filtro de detección de objetos.

Tras esta descripción caracterización fotométrica de GALANTE, obtenemos las ecuaciones de transformación entre GALANTE y *Sloan Digital Sky Survey (SDSS)* ([Fukugita et al., 1996](#); [Smith et al., 2002](#)) mediante fotometría sintética GALANTE a partir de los catálogos observacionales *Next Generation Spectral Library (NGSL)* ([Gregg et al., 2006](#); [Heap & Lindler, 2016](#)) y MAW ([Maíz Apellániz & Weiler, 2018](#)). Con estas ecuaciones, usamos

una pequeña región de Cygnus OB2 para obtener los puntos cero con una calibración preliminar usando el catálogo de *SDSS* por un lado y el *ATLAS All-Sky Stellar Reference Catalog (RefCat2)* (Tonry et al., 2018) por otro, concluyendo que la mejor calibración se obtiene con *RefCat2* debido a su precisión interna y bajos errores sistemáticos (Lorenzo-Gutiérrez et al., 2019). Con la llegada y reducción de los primeros datos GALANTE, obtuvimos la fotometría instrumental de una pequeña región de Cygnus OB2, gracias al tratamiento previo de estas imágenes por parte del CEFCA y con un algoritmo creado en *Python* a partir de paquetes de *IRAF* con los cuales obtenemos el flujo de los objetos en las imágenes del T-80. Aquí obtenemos una calibración de puntos cero preliminar usando nuestras ecuaciones de transformación.

De acuerdo con los objetivos de GALANTE, paralelamente elaboramos un algoritmo que fuese capaz de derivar los parámetros físicos estelares a partir de la fotometría GALANTE, al que llamamos MASTER (Monte Carlo Astrophysics Studio for galanTE colourS), haciendo uso de 6 bandas normalizadas por la banda central F515N, utilizando como figura de mérito el estadístico χ^2 . Para probar cómo funciona nuestra metodología, hacemos unos test con los catálogos de modelos de Kurucz (Castelli et al., 1997), TLUSTY (Lanz & Hubeny, 2003), Coelho (Coelho, 2014) and KOESTER (Koester, 2010) para analizar los errores sistemáticos e internos de MASTER. Además, utilizamos estos catálogos de modelos combinados, realizando un test con el catálogo observacional *Next Generation Spectral Library* (NGSL) y haciendo un análisis de los valores obtenidos para las variables físicas estelares de las estrellas que lo componen tras introducirlo en MASTER.

Una vez habíamos estudiado el comportamiento de MASTER con el catálogo observacional NGSL, obtuvimos la fotometría de todos los campos observados para Cyg OB2, calibrando esta vez con un método más refinado, un total de 5.6 grados cuadrados en esta región, obteniendo un total de 6765 estrellas. Seguidamente, introducimos nuestro catálogo del Cisne en MASTER para derivar los parámetros físicos de esas estrellas. A la vista de los

resultados obtenidos, tanto en los valores de χ^2 como de temperaturas efectivas, repasamos la bibliografía en esta región, tanto espectrométricos como fotométricos. El uso del catálogo de Gaia DR2 (Evans et al., 2018; Gaia Collaboration et al., 2016, 2018) nos permite hacer uso de distancias con las que, además de permitirnos estudiar cómo se distribuye la extinción en nuestro cono de observaciones, podemos representar diferentes isocronas con las que llegar a obtener la edad de las estrellas que observamos y obtener interesantes resultados de su evolución.

Abstract

GALANTE project has the goal to observe the Northern Hemisphere, 6 degrees wide, in the optical range. To reach this goal, 7 photometric bands have been selected to obtain the most complete information about the stellar physical variables. The new photometric system GALANTE has been designed using 4 J-PLUS bands in addition with 3 home-made filters. In this thesis, we present the characterization of the GALANTE photometric system and transformation equations derived from synthetic photometry adopting the observational library of the NGSL. With the support of the theoretical catalogues of Kurucz, Coelho, TLUSTY and KOESTER, we elaborate an algorithm called MASTER which uses the GALANTE colours to derive the physical stellar parameters. We apply MASTER to the NGSL as a test of this methodology before applying it to our observations. We also develop a pipeline using aperture photometry to obtain the first GALANTE catalogue from the observational region to study in this work, Cygnus OB2. After we derive the physical parameters of each star in our catalogue, we compare with spectroscopic and photometric catalogues from literature, obtaining novel results in this region.

Table of contents

List of figures	xix
List of tables	xxv
1 Introduction	1
2 The T-80 telescope	17
2.1 The <i>Observatorio Astrofísico de Javalambre</i> (OAJ)	19
2.2 T-80 technical description	19
3 The GALANTE Project	25
3.1 Observational strategy	27
4 GALANTE photometric system	37
4.1 Description and characterization	38
4.2 Standard stars system: The Next Generation Spectral Library (NGSL) and Maíz Apellániz & Weiler (2018) catalogue . . .	48
4.3 Transformation equations from standard stars system	53
4.4 Calibration of the GALANTE photometry	60
4.4.1 Calibration using SDSS	60
4.4.2 Calibration using RefCat2	64
4.4.3 Conclusions	68

5	MASTER: Monte-Carlo Astrophysics Studio for galanTE colourS	71
5.1	Data and methods	74
5.1.1	Libraries	74
5.1.2	Magnitudes and colour calculation	76
5.2	Fitting SEDs with MASTER	84
5.2.1	Reduced χ^2 statistic	91
5.3	Theoretical libraries test	92
5.3.1	Reddening free	93
5.3.2	With reddening	95
5.4	Observational tests: NGSL	99
5.4.1	NGSL test with K+T theoretical libraries	100
5.4.2	NGSL test with C+T theoretical libraries	102
5.4.3	NGSL test adding Ko theoretical libraries	106
5.4.4	Results with NGSL without noise	114
5.5	Summary and conclusions	119
6	GALANTE photometry of Cygnus OB2: observation, reduction and calibration	121
6.1	Why Cyg OB2?	122
6.2	Observations	125
6.2.1	Image reduction and photometry	125
6.3	GALANTE calibration of instrumental photometry	132
7	Deriving physical properties of Cygnus OB2 with MASTER	139
7.1	Models in MASTER to study Cygnus OB2	142
7.2	Physical stellar derived from K+T theoretical libraries	142
7.2.1	Comparison with previous results	149
7.2.2	Reddening estimation with Gaia DR2	153
7.3	Physical stellar derived from C+T theoretical libraries	160
7.4	Gaia DR2 comparison	167

8 Summary and conclusions

References

List of figures

1.1	Normalized spectral sensitivity of the human eye.	3
1.2	<i>UBV</i> transmission curves.	5
1.3	<i>RGU</i> transmission curves.	5
1.4	<i>VBLUW</i> transmission curves.	6
1.5	<i>ubvy</i> transmission curves.	7
1.6	<i>DDO</i> transmission curves.	7
1.7	<i>SDSS</i> transmission curves.	8
1.8	ALHAMBRA transmission curves.	9
1.9	<i>Gaia</i> transmission curves.	9
1.10	J-PAS transmission curves.	10
1.11	J-PLUS transmission curves.	11
1.12	GALANTE transmission curves.	12
1.13	The $[m_1]$ - $[c_1]$ Strömgen diagram from Strömgen (1966)	13
1.14	Bracket-line diagram using the GALANTE filter set.	14
2.1	OAJ observatory.	20
2.2	Ritchey-Chrétien schema.	21
2.3	Picture of the T-80 telescope.	22
2.4	Pictures of the CCD and filter wheel.	23
3.1	Footprint of the GALANTE fields divided by hemisphere.	28

3.2	Example image of low air mass for a field with different exposure times for GALANTE filters.	29
3.3	Real three-field GALANTE mosaic of Cyg OB2. Filters F861M, F660N, and F515N are represented in red, green, and blue, respectively.	33
3.4	Aladdin caption showing the observed stars.	35
4.1	Response functions of the J-PLUS and the GALANTE photometric system filters with Vega.	39
4.2	Response curves of the J-PLUS and the GALANTE with CCD, mirror, and atmospheric transmission.	40
4.3	SEDs for main-sequence hot stars normalized to the flux at 4000 Å and sensitivity curves of the three bluest GALANTE filters.	42
4.4	Bracket-like diagram using the GALANTE filter set.	43
4.5	Colour-colour diagram using <i>SDSS</i> synthetic photometry for NGSL and MAW catalogues.	54
4.6	Residual fitting errors for NGSL and MAW catalogues.	57
4.7	Residual errors from the fitting depending on the T_{eff} and A_v	59
4.8	Differences for stars observed with the T-80 telescope in Cyg OB2 and their <i>SDSS</i> DR8 and DR12 photometry.	61
4.9	GALANTE photometry histograms for differences between <i>SDSS</i> DR8 and DR12.	63
4.10	Differences for stars observed with the T-80 telescope in Cyg OB2 and their <i>RefCat2</i> and <i>SDSS</i> DR12 photometry.	65
4.11	Histograms for differences between instrumental AB magnitudes minus <i>RefCat2</i> and <i>SDSS</i> DR12.	66
4.12	Bracket diagram for Cyg OB2 using GALANTE filter set.	67
5.1	Range of physical stellar parameters for the theoretical libraries.	75
5.2	Two NGSL spectra in normalized magnitudes.	77

5.3	Red dots represent differences between C and K libraries in normalized magnitudes.	78
5.4	Normalized magnitude difference for a MS star.	79
5.5	Differences between GALANTE normalized magnitudes for each pair of models (C and K).	81
5.6	Differences between GALANTE normalized magnitudes for each pair of models (K and T).	82
5.7	Differences of normalized magnitudes for each GALANTE colour between C and K common models.	83
5.8	Differences of normalized magnitudes for each GALANTE colour between K and T common models.	84
5.9	Flux diagram for MASTER algorithm.	87
5.10	Differences between input and output physical parameters derived by MASTER, for different photometric errors.	95
5.11	Graphic summary of the results listed in Table 5.5.	98
5.12	χ^2 histogram comparing results with NGSL using 21 GALANTE no-normalized and 6 normalized colours.	100
5.13	NGSL and K+T theoretical stellar models in the plane of the physical variables T_{eff} and $\log(g)$	101
5.14	Results of deriving physical variables for NGSL stars based on theoretical libraries K+T.	103
5.15	NGSL and C+T theoretical stellar models in the plane of the physical variables T_{eff} and $\log(g)$	104
5.16	NGSL and C+T theoretical stellar models in the plane of the physical variables $\log(g)$ and metallicity.	104
5.17	Results of deriving physical variables for NGSL stars based on theoretical libraries C+T.	105
5.18	GALANTE normalized colours of different models with T_{eff} from 20 000 K to 50 000 K for different surface gravity values.	107

5.19	Results of deriving physical variables for NGSL stars based on theoretical libraries K+T+Ko.	108
5.20	Results of deriving physical variables for NGSL stars based on theoretical libraries C+T+Ko.	109
5.21	Diagram of the best fitting model for BD 442 051.	113
5.22	Diagram of the best fitting model for HD 126 327.	114
5.23	Results of deriving effective temperature for NGSL stars based on theoretical libraries C+T+Ko without noise.	115
5.24	Results of deriving $\log g$ for NGSL stars based on theoretical libraries C+T+Ko without noise.	116
5.25	Results of deriving $[\text{Fe}/\text{H}]$ for NGSL stars based on theoretical libraries C+T+Ko without noise.	117
5.26	Results of deriving reddening for NGSL stars based on theoretical libraries C+T+Ko without noise.	118
6.1	Urania's Mirror card (1825), showing Lacerta, Cygnus, Lyra and Vulpecula constellations and Anser star (α -vulp) illustration card.	122
6.2	Example of a raw science image in F515N for a 50 s exposure of Cygnus OB2.	127
6.3	Example of the detection objects with DAOSStarFinder.	130
6.4	Example of the flux extraction with aperture photometry.	131
6.5	Differences between GALANTE calibration and <i>RefCat2</i>	136
6.6	Differences between our GALANTE calibration, u (<i>SDSS</i> DR12), and <i>griz</i> (<i>RefCat2</i>).	137
6.7	Bracket diagram using the GALANTE filters.	138
7.1	Differences between $E(4405-5495)$ and $E(\text{B}-\text{V})$ as a function of $E(4405-5495)$	141
7.2	Output physical parameters for Cyg OB2 stars from MASTER using K+T theoretical libraries with Geneva isochrones.	143

7.3	PMS evolutionary tracks and GALANTE results.	144
7.4	A_V extinction map extracted from MASTER using K+T theoretical libraries.	145
7.5	Voronoi extinction map for Cyg OB2. Figure from Wright et al. (2015)	146
7.6	A_V extinction map, using K+T theoretical libraries, before and after 1 kpc.	147
7.7	A_V histogram of stars observed in the GALANTE region, whose values has been derived from MASTER.	148
7.8	Our pointing in the Local Arm.	150
7.9	A_G/A_V as a function of the amount of extinction $E(4405 - 5495)$	154
7.10	A_V comparison between the three catalogues using MASTER with K+T theoretical libraries.	155
7.11	Degeneracy between temperature and extinction using the Kurucz (red dots) and Coelho (blue dots) models.	157
7.12	A_V differences between GOSSS and GALANTE (K+T), Gaia DR2, and Wright et al. (2015)	159
7.13	Relative differences between T_{eff} from MASTER (K+T models), Wright et al. (2015) (blue dots) and the GOSSS (red dots) catalogues.	160
7.14	A_V density map extracted from MASTER using C+T theoretical libraries.	161
7.15	A_V extinction map, using C+T theoretical libraries, before and after 1 kpc.	162
7.16	A_V differences of common stars between GALANTE observations, Wright et al. (2015) and Gaia DR2 for the Cyg OB2 region.	163
7.17	A_V differences between GOSSS and GALANTE (C+T), Gaia DR2, and Wright et al. (2015)	164

7.18	Relative differences between T_{eff} from MASTER (C+T models), Wright et al. (2015) (blue dots) and the GOSSS (red dots) catalogues.	165
7.19	T_{eff} , $\log g$ and E(B-V) comparison histograms for Cygnus OB2 in this work, using MASTER with K+T and C+T theoretical libraries.	167
7.20	Gaia DR2 colour-magnitude diagram with T_{eff} from MASTER using K+T theoretical libraries.	168
7.21	Unreddened Gaia DR2 colour-magnitude diagram.	170
7.22	Unreddened Gaia colour-magnitude diagram with $\log g$ from MASTER.	171
7.23	Colour-absolute magnitude diagram for Gaia DR2 using reddening from MASTER, distances from Bailer-Jones et al. (2018) and extinction conversion from Wang & Chen (2019)	172
7.24	Distance-absolute magnitude diagram for Gaia DR2 using reddening from MASTER, distances from Bailer-Jones et al. (2018) and extinction conversion from Wang & Chen (2019)	174
7.25	Results for the Cyg OB2 stars using Gaia DR2.	177
7.26	Results of this study for T_{eff} and $\log g$ histograms in Cygnus OB2.	178

List of tables

2.1	JAST/T80 technical specifications.	23
4.1	Representative Photometric Parameters.	44
4.2	Representative Parameters of the filters of the GALANTE Photometric System.	46
4.3	Representative Parameters of the additional J-PLUS filters. . .	47
4.4	Description of the three spectral gratings for the NGSL obser- vations.	49
4.5	GALANTE and J-PLUS AB magnitudes example of the 378 NGSL stars.	51
4.6	GALANTE photometric ZPs from <i>SDSS</i> DR8 and DR12. . .	62
5.1	Colour code.	84
5.2	Number of cells of each model mesh used in this work, for both the first run and the second run.	86
5.3	Effective wavelength of the GALANTE photometric system filter set.	89
5.4	Summary of the results obtained using C and K libraries as observational input data with different photometric errors in flux.	94

5.5	Summary of the results obtained using C and K libraries as observational input data with different photometric errors in flux, adding E(B-V) in the observational catalogue.	97
5.6	Summary of the results we obtain for each block of models using the NGSL as input catalogue.	111
5.7	Comparison of example stars covering the range of each stellar physical parameters of the NGSL empirical library. We tabulate nine NGSL stars by way of example.	112
5.8	Summary of the results we obtain for each block of models (without noise) using the NGSL as input catalogue.	119
6.1	Zero Points calibration directly using <i>griz</i> from <i>RefCat2</i> and <i>u</i> band from <i>SDSS DR12</i> for common filters with <i>SDSS</i> and <i>GALANTE</i> transformation equations for the rest of the bands.	134
7.1	Values obtained from T_{eff} , $\log g$ and E(B-V) using the C+T and K+T models in this study for common stars with the <i>GOSSS</i> and Wright et al. (2015) catalogues.	151

“Llegué de noche, lloviendo y sin conocer el idioma.”

Pío Baroja al llegar a Motril. (1925)

1

Introduction

Since its inception, man has been curious about everything around him, and the objects in the sky are no exception. This interest continues today, reaching us daily in the form of images or videos either in the news, Facebook, or specialized media, being taken by both amateur cameras and powerful telescopes. To understand what we are seeing there, we need to study what is shown in them, and it is just at this moment that we talk about the measurements taken from those images. In this way, we can quantify and classify the objects captured by the telescope, obtaining data with which to work, as are the energy we receive from each object in images. The study of this density of electromagnetic radiation, known as flux, allows us to conclude how far the

object is from us, its temperature, and/or its age. To do this, we take fluxes collected by the detector of a telescope when passing through a filter. If we think of a glass that we are filling with water as if we were counting molecules that accumulate in it, we can make an analogy with an observation of this kind. Our counting system would in this case be a photon detector, while the water molecules would be the photons that we receive from space. The study of these data is what we call photometry. This process has been refined throughout history, beginning with the observation of objects in the sky that have been viewed since the origin of humanity.

The definition of stellar magnitude in astronomy marked the way to classify stars. The first catalogue of listed stars dates back to the era of Ptolemy and Hipparchus, setting a scale with which to classify sky objects visible from the Earth. This kind of magnitude is known as apparent visual magnitude (m_V), giving a value 6 to limit the visibility of a star by the naked human eye, while the brightest stars would have a magnitude of 1. In this way, brighter stars have a magnitude of between 1 and 2, and stars almost perceptible have a magnitude of 5 or 6. These astronomers were already representing the logarithmic eye response to light that human vision has. This system of magnitude is defined from the visual capability of the eye. Maximum human eye sensitivity is placed between 450 and 600 nm (see Figure 1.1), just where two of our three cones reach their highest excitation to light spectrum.

What they were doing was quantifying star fluxes and how eyes react to light. We can define the flux of a star as the number of photons (energy) that are received per second, per unit area, and per unit wavelength (f_λ) or per frequency (f_ν). Both fluxes are related by:

$$f_\lambda = (c/\lambda^2) f_\nu \tag{1.1}$$

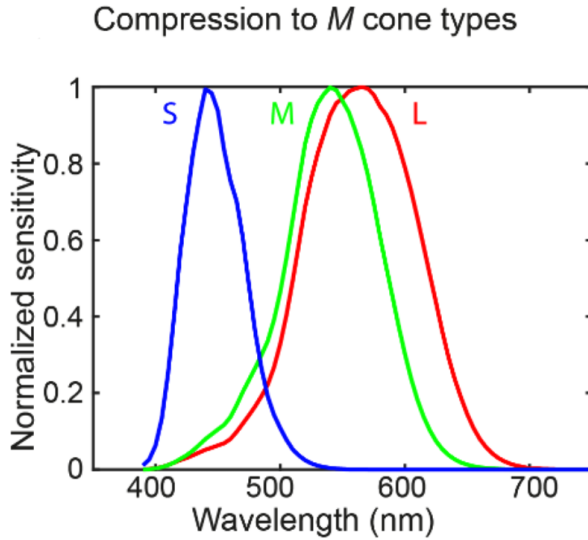


Fig. 1.1 Normalized spectral sensitivity of the human eye. Response of the eye to colour is plotted in human 3 cone types-labelled "S" for short wavelengths, "M" for medium, and "L" for long. [Gundlach et al. \(2018\)](#).

c being the speed of light. Suppose now that we observe two stars whose difference in magnitude is 1 unit. If we arrange F_1 and F_2 to their fluxes, being $m_1 > m_2$, we can write:

$$\begin{aligned}
 m_1 &= -2.5 \log_{10}(F_1) \\
 m_2 &= -2.5 \log_{10}(F_2) \\
 m_1 - m_2 &= 2.5 \log_{10}(F_2/F_1) = 1 \\
 \log_{10}(F_2/F_1) &= 1/2.5 = 0.4
 \end{aligned}
 \tag{1.2}$$

Or what is the same, a difference of a magnitude between one star and another is equivalent to having a flux 2.5 times higher.

If we want to calculate how much brighter a star is than another, or, equally, what magnitude one star has with respect to another, it is necessary to take a reference value, or zero point (ZP), depending on the magnitude system. Depending on this system, we can work with m_{ST} magnitudes (using flux in wavelength unit), m_{AB} (using flux in frequency unit), or m_{VEGA} , which uses the Vega flux to calibrate this system. We define the monochromatic m_{ST} system as:

$$m_{ST}(\lambda) = -2.5 \log(f_\lambda) + ZP_\lambda \quad (1.3)$$

where a constant flux $f_\lambda^0 = 3.631 \cdot 10^{-9} \text{ erg s}^{-1} \text{ cm}^{-2} \text{ \AA}^{-1}$ is used to have $m_{ST}=0$, which implies a $ZP_\lambda = -21.10$. Analogously to the ST magnitude system, the AB system is defined as

$$m_{AB}(\lambda) = -2.5 \log(f_\nu) + ZP_\nu \quad (1.4)$$

where to get the ZP in this system, we apply Equation 1.1 to define a flux in frequencies $f_\nu^0 = 3.631 \cdot 10^{-20} \text{ erg s}^{-1} \text{ cm}^{-2} \text{ Hz}^{-1}$, giving a zero point $ZP_\nu = -48.60$ for $m_{AB}=0$.

The design of the filters in order to obtain any property or physical parameter of the observed objects causes different configurations of photometric bands, depending on the scientific goal. We define a photometric system as a set of filters and a detector capable of obtaining information from the spectral energy distribution (SED) of the observed objects, from which their intrinsic and extrinsic physical properties is derived. The *UBV* system (Johnson & Morgan, 1953), based on the spectral response of the human eye (*V*) and the photographic plate (*B*), added a *U* filter to measure the Balmer jump. This addition made it possible to establish a first quantitative relationship between photometric colours and spectral properties. The *UBV* system aimed to take advantage of historical catalogues (visible and photographic) to establish a photometric database with the addition of a new filter (Figure 1.2).

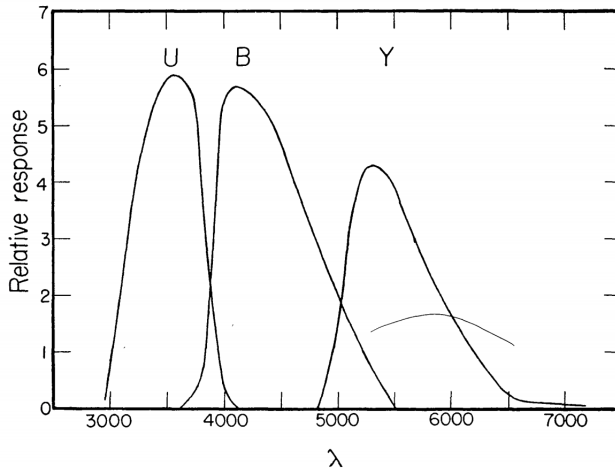


Fig. 1.2 *UBV* transmission curves from [Johnson & Morgan \(1951\)](#).

Another 3-band system was defined ([Becker, 1946](#)) with photographic detectors that disregarded the historical catalogues and focused more on the properties of the emitter than on those of the receiver (Figure 1.3).

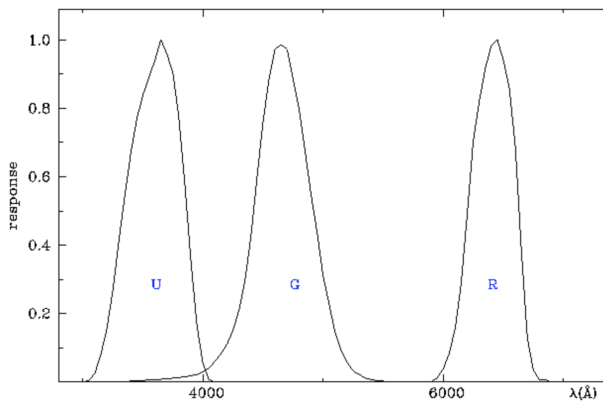


Fig. 1.3 *RGU* transmission curves. Image extracted from The Asiago Database on Photometric Systems ([Mermilliod et al., 1997](#)). Y means for the yellow colour, corresponding to the central region in the visible range.

On paper, the *RGU* system allowed a better stellar classification than the *UBV*, but the fact that it was based on the photographic plate, with a non-linear response, and depended on transformation equations between the *RGU* and the *UBV* greatly limited its development and nowadays it is rarely used. Walraven & Walraven (1960) introduced a photometric system with five bands, *VBLUW*, allowing the measurement of temperatures for early-type stars. The *W* and *L* bands in the ultraviolet region made it possible to estimate the Balmer jump with better precision for hot stars, in addition to the Johnson bands (Figure 1.4).

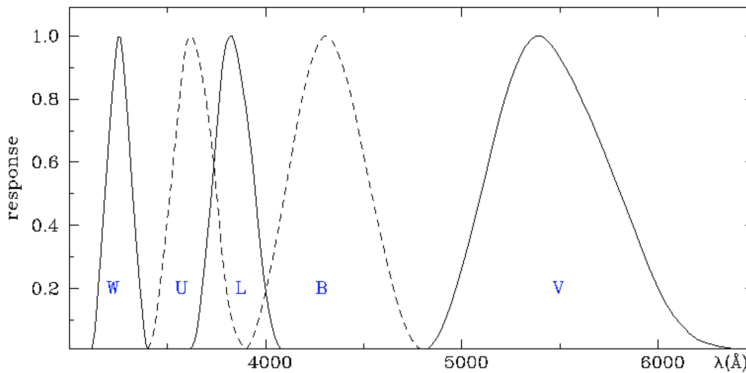


Fig. 1.4 *VBLUW* transmission curves. Image extracted from The Asiago Database on Photometric Systems (Mermilliod et al., 1997).

Strömgren (1966) developed a new approach to the photometric system based on narrower filters that not only provided information from the stellar continuum, but also allowed a quantitative measurement of some spectral lines. This fact enabled the possibility of estimating parameters such as metallicity ($[Fe/H]$) for the most common range of temperature we can find in the solar neighbourhood. He also obtained two indices, m_1 and c_1 , to measure the spectral features associated to some metal lines and the Balmer discontinuity respectively (Figure 1.5).

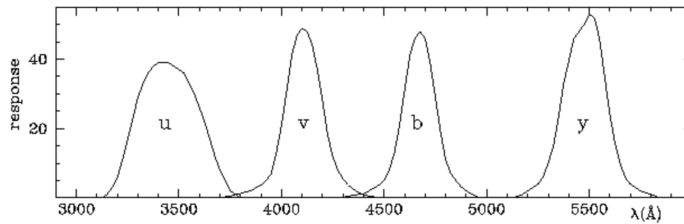


Fig. 1.5 *ubvy* transmission curves from [Strömgren \(1966\)](#).

The *DDO* system ([McClure & van den Bergh, 1968](#)) is another intermediate five-band photometric system designed to measure temperature and metallicity in late-type stars with a high precision in comparison with previous photometric systems (Figure 1.6).

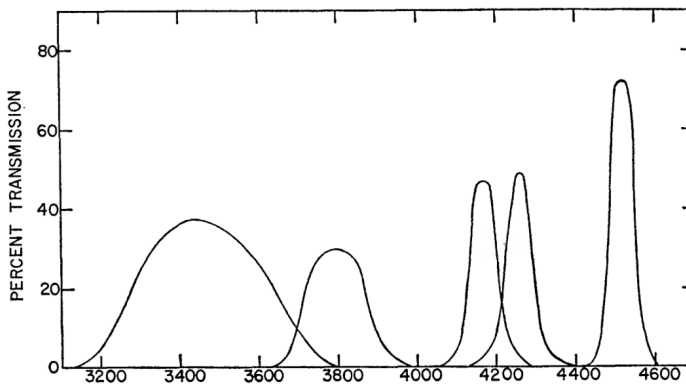


Fig. 1.6 *DDO* transmission curves from [McClure & van den Bergh \(1968\)](#).

Since the introduction of the CCD, the development of new photometric systems suffered an inflationary process, reaching its peak with the Sloan Digital Sky Survey (*SDSS*) ([Fukugita et al., 1996](#)), which combined the design of a photometric system in five bands, covering the visible range, with an industrial aspect of the observation (Figure 1.7). We show in Figure 1.8 another example is the ALHAMBRA photometric system based on 23 bands ([Aparicio](#)

Villegas et al., 2010), 20 in the visible range and 3 in the near infrared (NIR), which can actually be considered a low-resolution spectroscopy (Moles et al., 2008b).

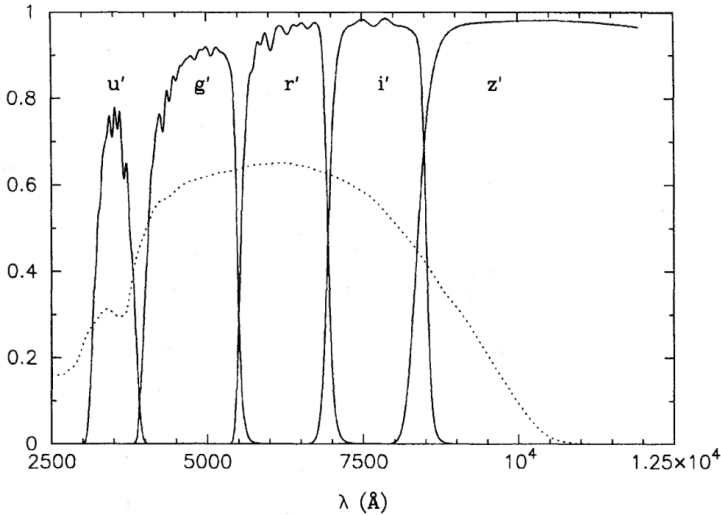


Fig. 1.7 SDSS transmission curves from Fukugita et al. (1996). The dotted line is the response curve of the UV-coated SiTe CCD.

Observational strategy in astronomy has undergone a drastic change and the number of large photometric surveys specifically designed to obtain singular information about different types of celestial objects has increased significantly. Recently, Gaia DR2 provided a whole-sky optical photometric survey using three very broad bands G , G_{BP} , and G_{RP} (Evans et al., 2018; Gaia Collaboration et al., 2018). The coverage, uniformity and dynamic range of Gaia photometry will undoubtedly be a gold standard for optical photometry in the future. More specifically, Maíz Apellániz & Weiler (2018) (hereinafter MAW) have shown that Gaia DR2 photometry can be calibrated without significant systematic biases and with photometric residuals of one hundredth of a magnitude or better (Figure 1.9).

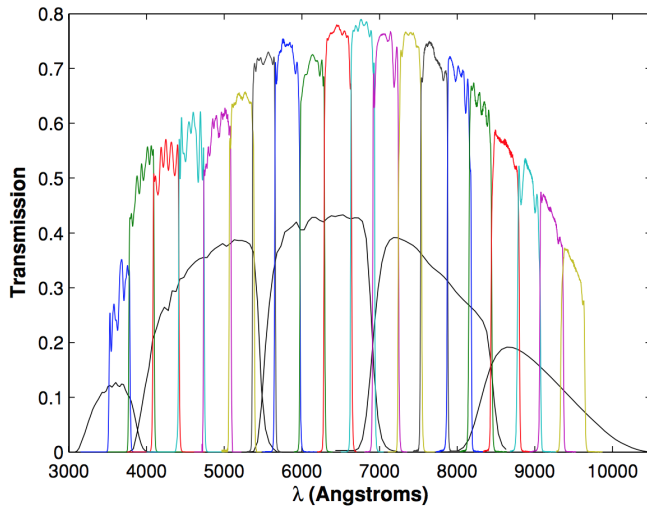


Fig. 1.8 ALHAMBRA and *SDSS* transmission curves from Aparicio Villegas et al. (2010).

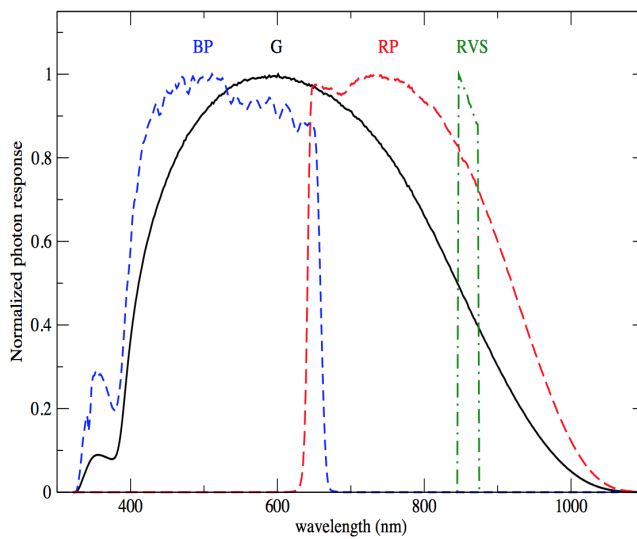


Fig. 1.9 *Gaia* transmission curves from Pancino et al. (2012).

Examples of these kinds of astronomical projects are J-PLUS and J-PAS, which are currently being developed in a new observatory in Javalambre (Teruel, Spain) with two telescopes of 80 cm and 250 cm, respectively. The main scientific objective of J-PAS (Figure 1.10) is cosmological, trying to measure the spectrum of Baryonic Acoustic Oscillations (BAOs) with photometric redshift estimations (Benitez et al., 2014), while J-PLUS (Figure 1.11) was originally planned to be an auxiliary survey for J-PAS calibration purposes (Cenarro et al., 2019). Given the observational restrictions of these programmes in terms of sky darkness and seeing, we designed a new monitoring programme, which we called GALANTE, focused on the brighter stars of the Galactic disk. This programme would be carried out on those clear nights where J-PLUS were not observable.

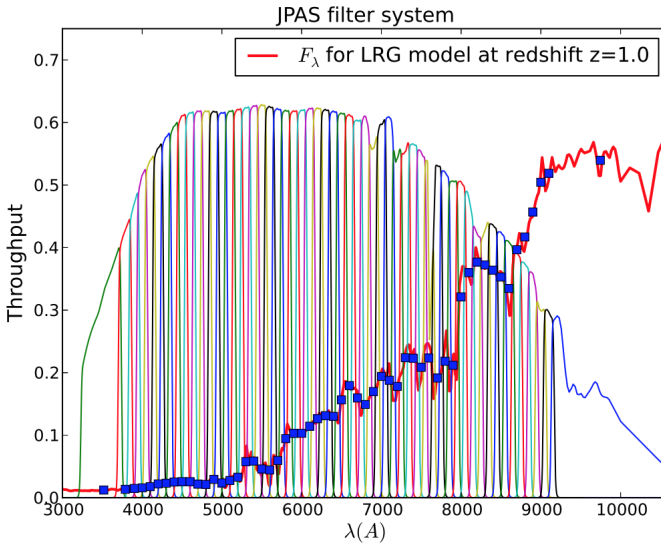


Fig. 1.10 J-PAS transmission curves from Benitez et al. (2014).

The GALANTE project is a photometric survey that will cover the Northern Galactic plane defined by $\delta \geq 0^\circ$ and $|l| \leq 3^\circ$. This project uses seven intermediate+narrow band filters aimed at measuring all stars of that region

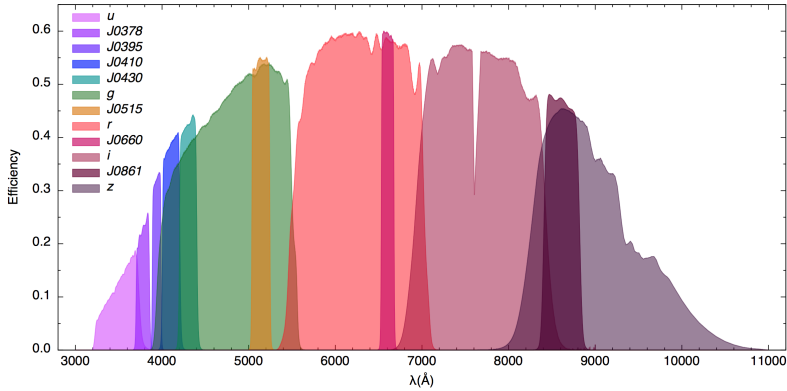


Fig. 1.11 J-PLUS transmission curves from [Cenarro et al. \(2019\)](#).

of the sky with AB magnitudes ≤ 17 (Figure 1.12). These seven filters are four J-PLUS filters (F348M, F515N, F660N, and F861M) and three new customized filters developed by the GALANTE team (F420N, F450N, and F665N). The number, width and effective wavelength of the filters compose an optimal system to accomplish those objectives proposed by [Maíz Apellániz et al. \(2019a\)](#). A Southern version of the GALANTE program has been proposed to be performed with the twin Cerro Tololo 80 cm telescope developed for the S-PLUS project ([Saito et al., 2018](#)).

In order to classify stars using their photometry, Strömberg developed $[m_1]$ and $[c_1]$ indices, based on bands $uvby$ with wavelengths centred in 3500, 4110, 4670, and 5470 Å. Equation 1.5 describes both colour indices, being dependent on reddening ([Strömberg, 1966](#)).

$$\begin{aligned} c_1 &= (u - v) - (v - b) \\ m_1 &= (v - b) - (b - y) \end{aligned} \tag{1.5}$$

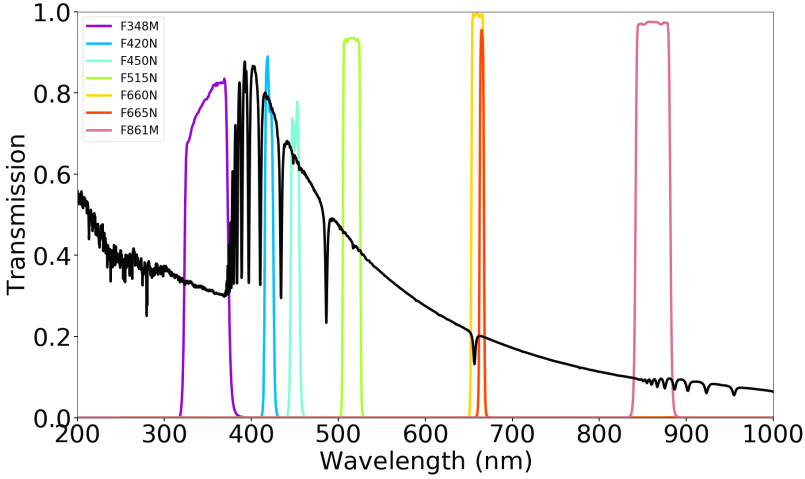


Fig. 1.12 GALANTE transmission curves from [Lorenzo-Gutiérrez et al. \(2019\)](#). The Vega spectrum is superimposed onto the GALANTE filters.

To remove dependent colour excess from photometry, brackets in Equation 1.6 are defined, giving great capability to observational photometry ([Strömgen, 1966](#)).

$$\begin{aligned} [c_1] &= c_1 - 0.20(b - y) \\ [m_1] &= m_1 + 0.18(b - y) \end{aligned} \tag{1.6}$$

With these two indices, it is possible to classify stars by spectral class, being independent from interstellar reddening. In Figure 1.13 we represent how, using the Balmer jump, this photometric system can make a spectral classification supported by a two-dimensional diagram with $[m_1]$ and $[c_1]$.

Following similar reasoning, it is possible to develop a colour combination from GALANTE photometry (Lorenzo-Gutiérrez et al., 2019; Maíz Apellániz et al., 2019a), which is analogous to $[m_1]$ and $[c_1]$ indices. This will allow us to visually classify observed stars from their photometry in GALANTE bands.

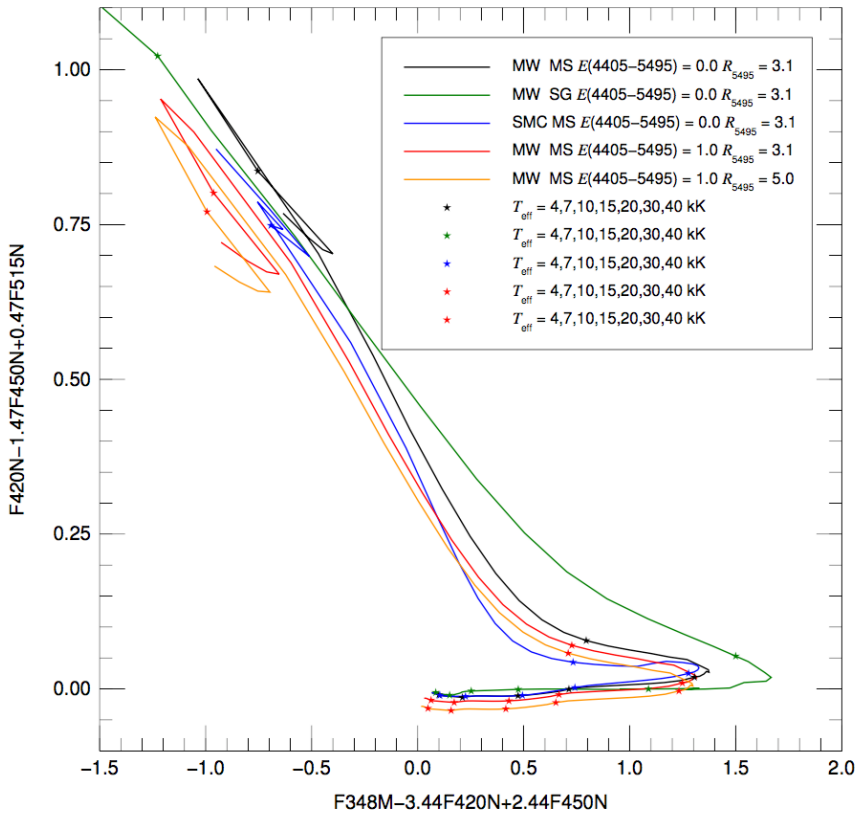


Fig. 1.14 Bracket-line diagram using the GALANTE filter set (Maíz Apellániz et al., 2019a). It shows how, for a fixed metallicity and extinction law, it is possible to classify the stars by T_{eff} independently of reddening.

Figure 1.14 shows a bracket-line diagram using 4 GALANTE bands for stars from 4000 K to 40 000 K with different colour excess $E(4405-5495)$ and extinction type R_{5495} .

"A scientist in his laboratory is not a mere technician: he is also a child confronting natural phenomena that impress him as though they were fairy tales."

Marie Curie (1867-1934)

2

The T-80 telescope

Contents

2.1	The <i>Observatorio Astrofísico de Javalambre</i> (OAJ) . . .	19
2.2	T-80 technical description	19

This thesis could not have been possible without observations. The building of a new observatory in Javalambre (Teruel, Spain) gave us a great opportunity to develop GALANTE. In this new facility, there are two telescopes, one is an 80 cm for the J-PLUS project (Cenarro et al., 2019), and the large one with 250 cm for the J-PAS project (Benitez et al., 2014). The big one, the T-250, is a 250 cm telescope that has a 4.7 deg^2 panoramic camera with 14 large-format CCDs forming a mosaic, amounting to 1.2 Gpix. This J-PAS project will observe around 8500 deg^2 in the Northern Galactic plane, using a set of 54 contiguous narrow-band filters in the optical range, adding two broad-band filters placed at the blue and red sides of the visible, plus three *SDSS* filters (Cenarro et al., 2017). Using this set of narrow-band filters, J-PAS will provide the SED of every object up to $AB < 21 \text{ mag}$, generating a 3D map image with high astronomical applications. The major goal of the 80 cm is to calibrate the cosmological observations from the J-PLUS project in order to use them in the calibration of the 250 cm. The J-PLUS project was created as a multi-filter survey to support the J-PAS in the technical and scientific scenarios, using the T-80 telescope with a set of 12 narrow, intermediate, and broad photometric bands. This photometric system form the basis of J-PAS, building a systematic technical developments of data reduction, pipelines, calibration procedures, scientific software, and storage hardware in the same way that J-PAS will be. The main goal of the J-PLUS project is to observe the most J-PAS targets as possible in order to support and complement the J-PAS photometric calibration (Varela et al., 2014). The GALANTE project is possible because J-PLUS cannot use the Javalambre Auxiliary Survey Telescope (T-80) on near fullmoon nights, or on nights with bad seeing. Those conditions give GALANTE, at least three nights before and after fullmoons, so the 80 cm in Teruel was the perfect telescope for this purpose.

2.1 The *Observatorio Astrofísico de Javalambre* (OAJ)

The construction of the *Observatorio Astrofísico de Javalambre* (OAJ), whose main projects are J-PLUS and J-PAS, opened a niche for the development of the GALANTE project. OAJ is located on *El Pico del Buitre* ($40^{\circ} 02' 28.67''$ North, $01^{\circ} 00' 59.10''$ West) in Teruel, with an altitude of 1957 meters above the sea level. It was conceived, constructed, and is operated by the *Centro de Estudios de Física del Cosmos de Aragón* (CEFCA) with different funding agencies (*Gobierno de Aragón, Ministerio de Ciencia, Innovación y Universidades, Fondo de Inversiones de Teruel, Feder, and ERC*). This place has an annual median extinction of 0.22 mag in the V-band, becoming 0.18 mag on photometric nights. The median value of seeing is variable according to the season of the year, becoming 0.69" in summer and 0.77" in winter. The seeing is also stable for long periods, for example a constant value of 0.8" was obtained during several entire nights (Moles et al., 2010). Figure 2.1 is a real picture of OAJ showing the two domes for the T-250 and T-80 telescopes, the Residence and Control building (which includes the control room, laboratories, data archiving/storage room, and the residence area), the General services plant (room for water and fuel tanks, power generators, dry air pumps, etc.), the Monitor building (small building to measure the seeing, extinction and clouds coverage), and the Aluminizing plant (to clean and aluminize mirrors).

2.2 T-80 technical description

The T-80 is an 80 cm telescope, with a focal number of 4.5. It has a German-equatorial mount and the optical configuration is a Ritchey-Chrétien with 1.7 degrees of field of view (FOV) in full optical performance, reaching 2 degrees diameter with a slightly degraded image quality ($< 1\%$). The T-80 has a Cassegrain layout focal plane with a field corrector of three spherical lenses with 115 - 140 mm diameters. The distance between M1 and M2 is

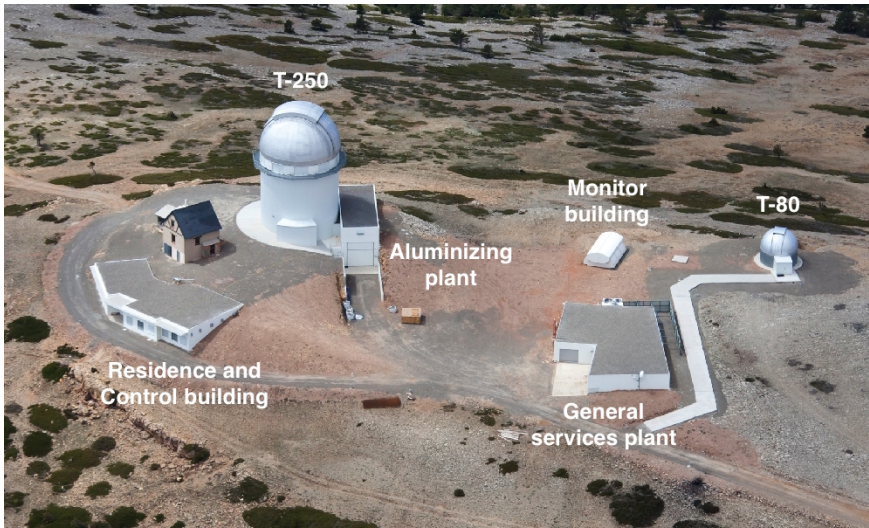


Fig. 2.1 OAJ observatory.

0.83 m, and the back focal distance is 160 mm. It is provided with a 3 conical baffles system. Table 2.1 summarizes all these technical specifications while Figure 2.3 shows a picture of the T-80 taken in my three-month internship at CEFCA.

The camera in the T-80 telescope installed for J-PLUS which is also used for GALANTE, is the T-80Cam. It is a wide-field camera placed in the Cassegrain focus. This camera has a high efficiency CCD with a 9.2k-by-9.2k, $10\ \mu\text{m}$ pixel, with a read-out noise of 3.4 electrons (RMS). This CCD almost covers the telescope's total FOV with a pixel scale of $0.55''/\text{pixel}$, reading 16 ports simultaneously, which allows read-out times of 12 s with that good RMS. The CCD response is optimized from 380 to 850 nm (Ederoclite et al., 2017).

T-80Cam consists of two main systems: the filter and shutter unit (FSU), and the cryogenic camera. The FSU contains two filter wheels and a shutter. The cryogenic camera takes care of the cooling and vacuum for the whole system, including the CCD and the detector electronics. Figure 2.4 shows a

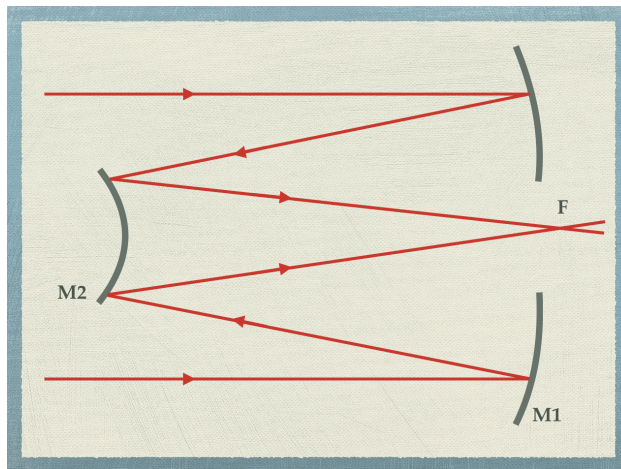


Fig. 2.2 Ritchey-Chrétien schema. This kind of telescopes are Cassegrain designed without third order coma and spherical aberration, allowing a large FOV.

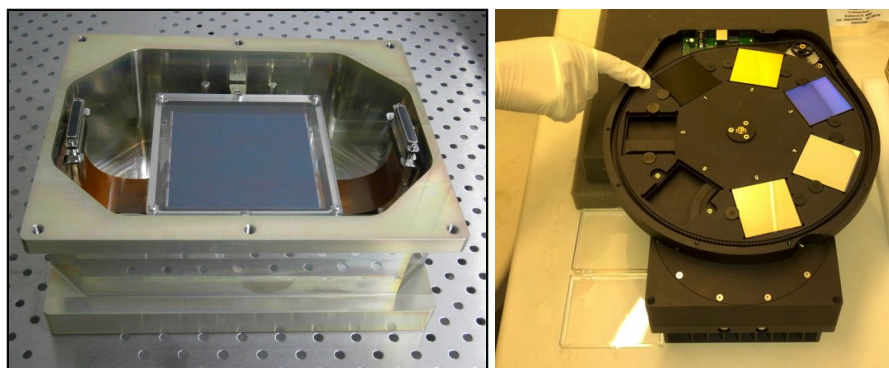
picture of the CCD from the T-80Cam (left) and a filter wheel (right) with 5 filters.



Fig. 2.3 Picture of the T-80 telescope taken during the three-month internship at CEFC.

Table 2.1 JAST/T80 technical specifications.

Optical configuration	Ritchey-Chrétien
M1 diameter	83 cm
FOV diameter	2 deg (130 mm physical size)
Effective collecting area	0.44 m ²
Etendue	1.5 m ² deg ²
Focal length	3712 mm
F number	4.5
Plate scale	55.56 arcsec/mm
Mount	German equatorial
Focus	Cassegrain

**Fig. 2.4** Pictures of the CCD from the T-80Cam (left) and a filter wheel (right) with 5 filters, taking from CEFCA website (www.cefca.es).

"Many of life's failures are people who did not realize how close they were to success when they gave up."

Thomas A. Edison (1847-1931)

3

The GALANTE Project

Contents

3.1	Observational strategy	27
------------	-------------------------------	-----------

Nowadays there are many photometric systems in the complete optical range, so one may ask why we need a new one. In this chapter we are going to explain why we need GALANTE.

The GALANTE Project was born with a clear main goal: homogeneously cover the stars of the Galactic disk in the optical range, including the brightest, up to a limit of magnitude 17-18. There is currently only one existing optical CCD photometric survey that covers the northern Galactic plane, from the

brightest stars to a given magnitude limit: Tycho-2. That survey has an exceptionally good absolute calibration (Maíz-Apellániz, 2005; Maíz Apellániz, 2006, 2007) but it provides only 2 filters (B_T and V_T), only reaching magnitudes down to 11-12. When combined with 2MASS NIR photometry it yields a first approximation to the optical+NIR SED of a star but that information is quite limited: it cannot be used to distinguish between, for example, O and B stars, and it does not cover faint objects. A number of ongoing projects (IPHAS, VPHAS, SEGUE, etc.) are extending the filter coverage of the northern Galactic plane and reach much fainter magnitudes. However, they all saturate at around 10-13 magnitudes, hence providing little or no overlap with Tycho-2 and ignoring the reference objects of many studies but not having uniformly measured photometry in the same system as most of the (faint) members of their population. All of the above surveys use broadband filters. However, as the experience with Strömgren photometry, and more recently with ALHAMBRA, clearly shows, an especially tuned set of intermediate- and narrow-band filters can provide more precise information about stellar effective temperatures, gravities, and metallicities and also better measurements of the amount and type of extinction (Aparicio Villegas et al., 2010, 2011; Maíz Apellániz et al., 2014; Moles et al., 2008a). In this context the GALANTE survey is proposed to map the northern Galactic plane with a set of 7 carefully selected intermediate- and narrow-band filters, observing all stars (including bright stars) down to AB mag = 18 with SNR between 70 and 500. With these figures, the expected number of objects in the final catalogue is over 5 millions entries, which will include 90% of Galactic O-type stars up to the selected limiting magnitude. In this way, we attain a balance between total observing time as driven by Galactic latitude width (6 degrees) and the sample completeness of O-type stars.

Other surveys are using filter sets that are not capable of taking advantage of the Balmer jump (SDSS *ugriz*, Tycho-2 *BV*, or 2MASS *JHK*), this being the only way to obtain T_{eff} for hot stars (Maíz Apellániz & Barbá, 2018a; Maíz

Apellániz et al., 2014; Sota et al., 2014). Furthermore, this is the first survey that includes two narrow filters (on-band and off-band) for H_α in order to obtain photometry from that line for stars (in absorption or emission).

The observation of a northern Galactic disk band, 6 degrees wide, on 7 photometric bands covering the entire optical range is, in itself, a first-quality astronomical product with a great impact on a wide range of cutting-edge scientific objectives. GALANTE has access to the best and most complete collection of astronomical data to perform an accurate and detailed calibration of stellar physical parameters. This makes it an ideal tool for further Galactic studies focused on weaker objects.

With the achievement of this project, we will determine preliminary stellar physical parameters such as, T_{eff} , $\log g$ and metallicity for most stars in the sample, but with coverage and uncertainties very dependent on the spectral type and luminosity class of the targets. For late-type stars we estimate an average uncertainty of 10%, 25%, and 30% for T_{eff} , $\log g$ and $[\text{Fe}/\text{H}]$, respectively. For earlier spectral types the expected uncertainty in T_{eff} is even better than 10%. With about 5 million stars observed in a homogeneous way, the photometric information provided by GALANTE will be split and averaged in bins of different spectral types, luminosity classes and metallicities. It will thus constitute a set of standards, very accurate photometric optical SEDs that will be used as a reference for improving the flux calibration of existing and future empirical stellar libraries, as well as for transforming the continuum shape of theoretical stellar libraries to the observational plane.

3.1 Observational strategy

GALANTE NORTE started taking data in 2016 and GALANTE SUR in 2018 (fields in Figure 3.1). To date, 74 fields have been observed for the 7 GALANTE bands (including Cyg OB2, North America Nebula, Berkeley 59, M31, and M37 among others), which corresponds to ~ 125 square degrees,

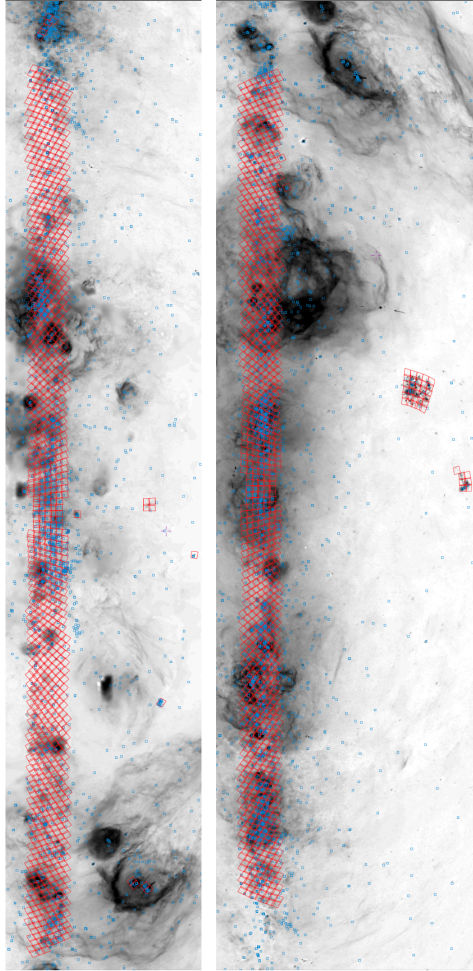


Fig. 3.1 Footprint (red) of the GALANTE fields divided by hemisphere (left: north, right: south). Blue symbols are stars from the Galactic O-Star Catalog (GOSC, [Maíz Apellániz \(2017\)](#); [Maíz-Apellániz et al. \(2004\)](#); [Maíz Apellániz et al. \(2012\)](#); [Sota et al. \(2008\)](#), <http://gosc.cab.inta-csic.es>), which are mostly O+B+WR stars. The background is an H_{α} image ([Finkbeiner, 2003](#)) in a log scale aligned with Galactic coordinates using an Aitoff projection. The off-plane fields include the LMC, the SMC (right), M31, and M33 (left).

with another 114 fields already observed in at least 3 bands. If the weather behaves, we should complete the northern survey in 2021 and the southern in 2023. For the long-term future several extensions are possible: deep surveys of interesting regions, multiple epochs, and additional filters are some of the new improvements.

Focusing on the northern GALANTE project of this thesis, we explain how we fill the observing blocks for data petition with the T-80 telescope. The GALANTE has been awarded around 65 hours per semester from the "OAJ Open Time". These hours are dedicated to GALANTE in those three nights before and after fullmoon in queue observation mode. Since J-PLUS and GALANTE having common filters, GALANTE can also be observed in those J-PLUS nights with bad seeing, where seeing is between 1.2" to 1.5" and a maximum airmass value of 2.

Time (sec)	Exposures	Standar Flag	Offset RA (Arcsec.)	Offset DEC (Arcsec.)	Filter
100.0	2	SCIENCE	0	0	G0420
10.0	2	SCIENCE	0	0	G0420
1.0	2	SCIENCE	0	0	G0420
0.1	2	SCIENCE	0	0	G0420
100.0	2	SCIENCE	0	0	G0450
10.0	2	SCIENCE	0	0	G0450
1.0	2	SCIENCE	0	0	G0450
0.1	2	SCIENCE	0	0	G0450
100.0	2	SCIENCE	0	0	G0665
10.0	2	SCIENCE	0	0	G0665
1.0	2	SCIENCE	0	0	G0665
0.1	2	SCIENCE	0	0	G0665

24 Image(s), 12 Row(s) Close

Fig. 3.2 Example image of low air mass for a field in Cygnus OB2 where we request different exposure times for customized GALANTE filters.

Thanks to the OAJ, which designed a specific GALANTE application to account for our target fields, we include each observing block individually. In this application tool, we fill each GALANTE filter for low and high air mass in each exposure time. Figure 3.2 is an example caption of low air mass for a field in Cygnus OB2 where we request different exposure times for customized GALANTE filters.

Once we have defined the object to be analyzed, we have chosen three fields of GALANTE mapping that encompass Cyg OB2, and which generally cover the region delimited by $306.87 < RA < 309.30$ and $39.97 < DE < 42.32$.

The observations carried out by the OAJ for the GALANTE project can be divided into 2 types: those made with the common filters with J-PLUS and those observed with the 3 custom GALANTE filters. The first ones are observed on those nights of the J-PLUS project in the conditions of the night are above the upper limit for their objectives, while GALANTE's filter wheel is prioritized in the guaranteed time to this project, which we remember it is seen in the 3 nights before and after the full-moon of each month. Thus, the GALANTE Core Team proposes to divide the observations for each field into two blocks:

- Observations with the four common J-PLUS filters: The GALANTE observations with these filters are carried out during "J-PLUS time" when J-PLUS is not being observed as part of an agreement between teams. J-PLUS will observe in dark/grey sky conditions and when the atmospheric seeing is lower than 1.5 arcsec. In this context, it has been agreed with the J-PLUS team that GALANTE observations with these four filters will have high priority during the nights, or fractions of nights, when the sky background or the atmospheric seeing are not acceptable for J-PLUS, if not in conflict with other OAJ planned operations. GALANTE represents a good opportunity to take scientific

data with the JAST/T80 when other projects, more demanding in terms of observing conditions, cannot be executed.

- Observations with the three GALANTE customized filters are carried out using part of the “OAJ Open Time”, and each petition is our long-term observational proposal for this case.

After the first campaigns, we saw the need to observe the fields with another strategy: the four common J-PLUS filters will be observed using guaranteed time on different nights. Note that the three GALANTE customized filters cannot be easily observed using guaranteed time because their use requires a change of filter wheel (which can only be carried out during the day) and a large fraction of our guaranteed time will take place on nights when the two standard filter wheels are required. Therefore, our requests for observation are only focused on these 3 GALANTE filters. The current comment strategy followed for the observation time request is detailed below:

- Four exposures of 100 s each (“long” exposures, for magnitudes ~ 13.0 - 18.0) at two different air masses. Here the observing time has been modified from 50 to 100, according to the experience acquired with the previous observations.
- Two exposures of 10 s each (“intermediate” exposures, for magnitudes ~ 11.0 - 13.0).
- Two exposure of 1 s each (“short” exposure, for magnitudes ~ 8.5 - 11.0).
- Two exposures of 0.1 s each (“very short” exposure, for magnitudes ~ 6.0 - 8.5 , only for about 40% fields).

This leads to a total observing time of 500 hours, which would be split into four semesters. All the fields will be observed with the four types of exposures (long, intermediate, short, and very short) exposures, thus providing

a S/N between 70 and 500 for the whole 6-18 magnitude range. The brightest stars (starting around magnitude 6, there are ~ 200 in the studied region) are expected to saturate even in the 0.1 s exposures. In these cases we have used test exposures to confirm that PSF fitting of the profile wings is good enough to obtain accurate photometry. For the long exposures, the fields will be observed twice during the night at different air masses to provide an accurate photometric calibration (note that we are requesting non-standard filters so they will not have the standard OAJ calibration). The photometric calibration will be carried out using different independent methods to check its consistency. The use of multiple exposures for the long and intermediate integration times is required for the elimination of cosmic rays in field with a large number of sources. The shorter integration times can be done with a single exposure because of the small number of significant sources. The limiting magnitude has been chosen according to the following criteria: a) More than 3 magnitudes overlapping other deeper surveys in such a way that we get a high stellar density in common with those surveys; and b) Complete GALANTE photometry for a high proportion of disk stars, taking into account that GALANTE filters enable the best photometric stellar classification so far, in particular for young and massive objects.

GALANTE observations of Cygnus cover 6 square degrees on the sky, but we have to distinguish between observations with J-PLUS - GALANTE and customized GALANTE filters. In Figure 3.3 we show a real three-field GALANTE mosaic of Cyg OB2. Filters F861M, F660N, and F515N are represented in red, green, and blue respectively. The result combines four different exposure times so that all pixels have at least one non-saturated image. The field is 1.850×2.405 square degrees with N towards the top and E towards the left.

Figure 3.4 represents an Aladdin picture (Bonnarel et al., 2000) which shows in red dots stars observed by the T-80 telescope with four of the seven GALANTE filters (F348M, F515N, F660N and F861M), and with four *SDSS*

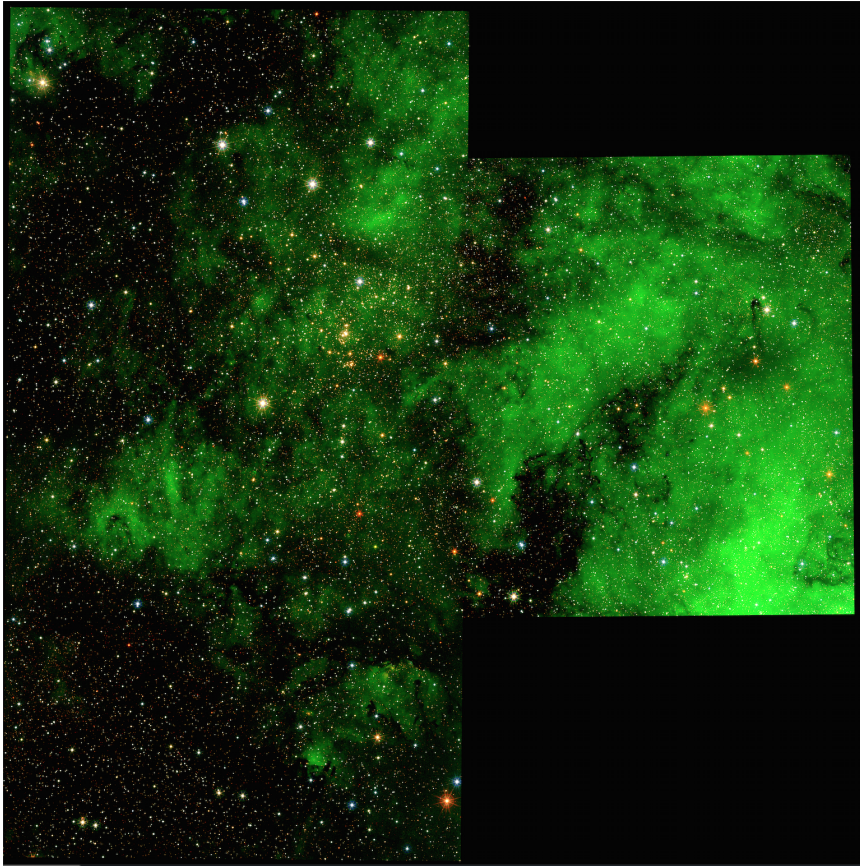


Fig. 3.3 Real three-field GALANTE mosaic of Cyg OB2. Filters F861M, F660N, and F515N are represented in red, green, and blue, respectively. The result combines four different exposure times so that all pixels have at least one non-saturated image. The field is 1.850×2.405 square degrees with N towards the top and E towards the left. Credits: Jesús Maíz Apellániz.

ones ($gSDSS$, $rSDSS$, $iSDSS$, and $zSDSS$). The blue contour represents the area covered by the 11 filters used in this study (F420N, F450N, and F665N added), that cover a total of 5.6 square degrees observed in all bands. Since we want to include all bright stars and our magnitude limit is not too deep, g

$(AB) \leq 17$ mag, we need to establish a compromise between the total number of exposures per field and the minimum and maximum exposure times. In this way, we first chose four exposures per filter of 100 s, 10 s, 1 s, and 0.1 s to 2 different air masses, but changing the maximum exposure time of the three custom filters from 100s to 50. The choice of two sets of observations to different air masses was advised by the need to obtain an assessment of the night estimation coefficient, however, the experience gained throughout the first observation campaigns led to a change of strategy, where custom filters had a maximum exposure time of 100s.

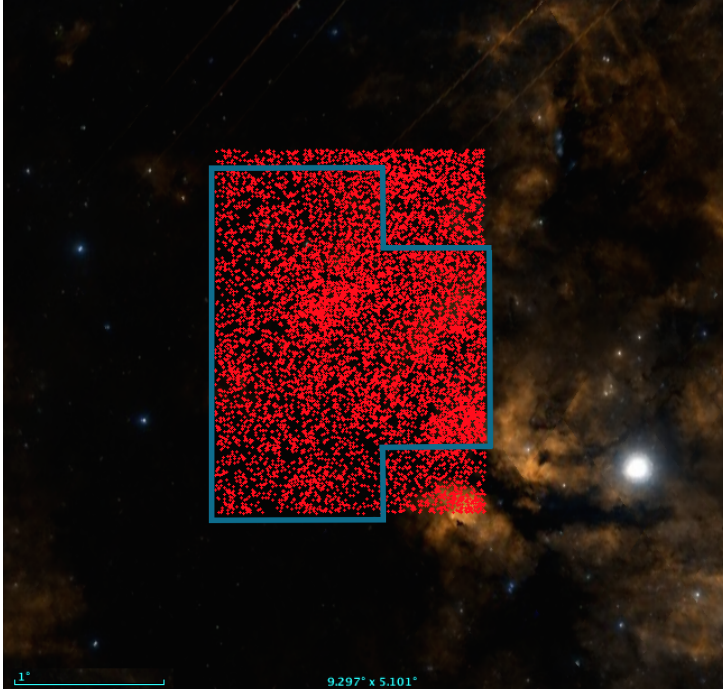


Fig. 3.4 Aladdin caption showing in red dots the observed stars with 4 GALANTE filters (F348M, F515N, F660N, and F861M), and with other *SDSS* ones (*gSDSS*, *rSDSS*, *iSDSS*, and *zSDSS*) in addition. The blue contour represents the area covered by the 11 filters used in this study (F420N, F450N, and F665N added). This give us 5.6 square degrees observed on each filter for 11 bands with a total of 6765 stars.

"Mmmm... Two bucks and it only transports matter?!"

Homer J. Simpson

4

GALANTE photometric system

Contents

4.1	Description and characterization	38
4.2	Standard stars system: The Next Generation Spectral Library (NGSL) and Maíz Apellániz & Weiler (2018) catalogue	48
4.3	Transformation equations from standard stars system	53
4.4	Calibration of the GALANTE photometry	60
4.4.1	Calibration using SDSS	60
4.4.2	Calibration using RefCat2	64
4.4.3	Conclusions	68

4.1 Description and characterization

Deriving physical stellar (or galaxy) parameters is the main goal of every photometric system. In our case, we achieve this aim with a new filter set designed to plug some gaps found in previous surveys. The GALANTE photometric system has been defined using 4 J-PLUS filters (Cenarro et al., 2017) and 3 purpose-built filters. This composition of intermediate and narrow band filters covers the optical range from 3000 Å to 9000 Å. This filter set has been selected with a direct goal: deriving stellar effective temperatures for hot stars in an optimal way (Maíz Apellániz & Barbá, 2018a; Maíz Apellániz & Sota, 2008; Maíz Apellániz et al., 2014). We will also be able to obtain the gravity and metallicity (the latter for stars cooler than 10 000 K), allowing us to discriminate between giants, supergiants, dwarfs, and between solar or SMC metallicities.

In Figures 4.1 and 4.2 we present the setup of the filters. Figures 4.1 (a) and (b) show the layout of the J-PLUS and GALANTE filters respectively, leaning on the Vega spectrum. Note that in this case we only plot the transmission curves of the filters, allowing to the reader a visual location of each one. Focusing on GALANTE, Figure 4.1 (b) plots the configuration of the selected GALANTE filters, which enable us to measure the key zones in the spectra to derive physical parameters. In Figure 4.2 we plot the response functions of the J-PLUS and the GALANTE photometric system filters. In discontinuous grey we represent the response curve of the CCD and mirror, while discontinuous green is the CCD, mirror and atmospheric transmission at 1.3 air mass curve. The *SDSS* response curves are represented in continuous black, and the other continuous curves are the GALANTE and J-PLUS filter response curves convolved with CCD, mirror and atmospheric transmission at 1.3 air mass.

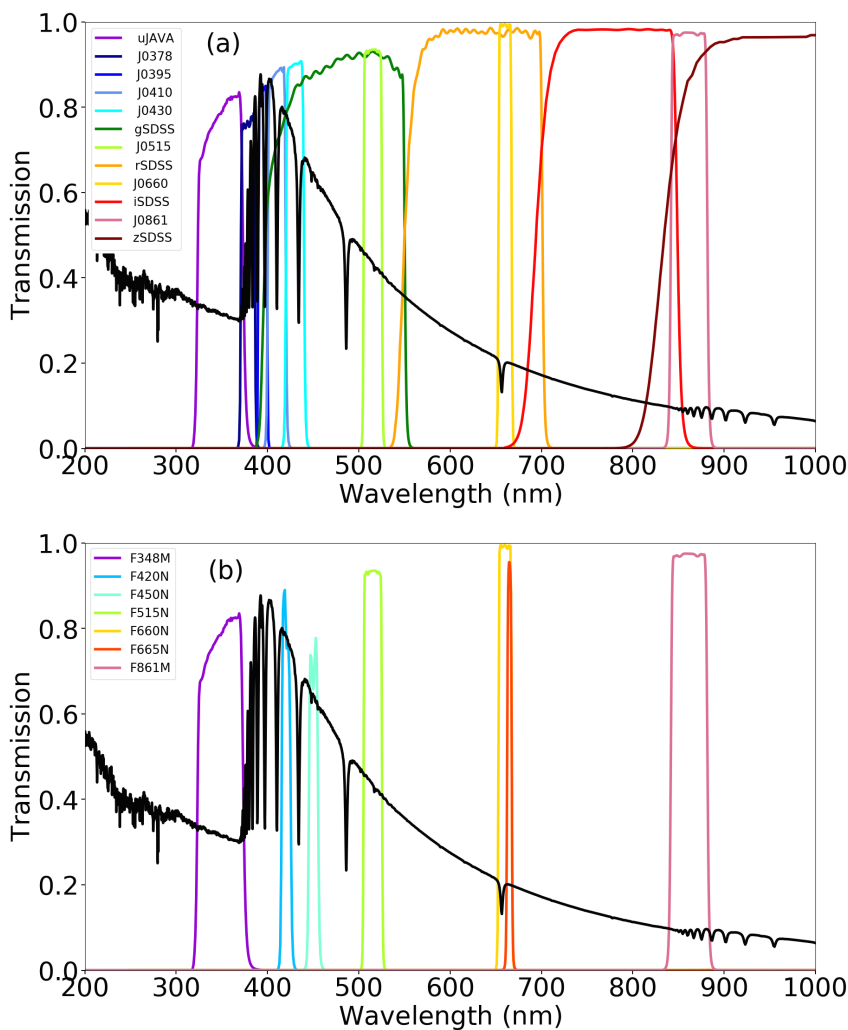


Fig. 4.1 Response functions of the J-PLUS and the GALANTE photometric system filters. In both pictures we only took into account filter transmission curves to visualize their positions. Figure (a) represents the Vega spectrum superimposed onto J-PLUS filters transmission curves. Figure (b) represents the Vega spectrum superimposed onto GALANTE filters transmission curves. To make the graphic possible, the flux of Vega has been normalized and scaled properly.

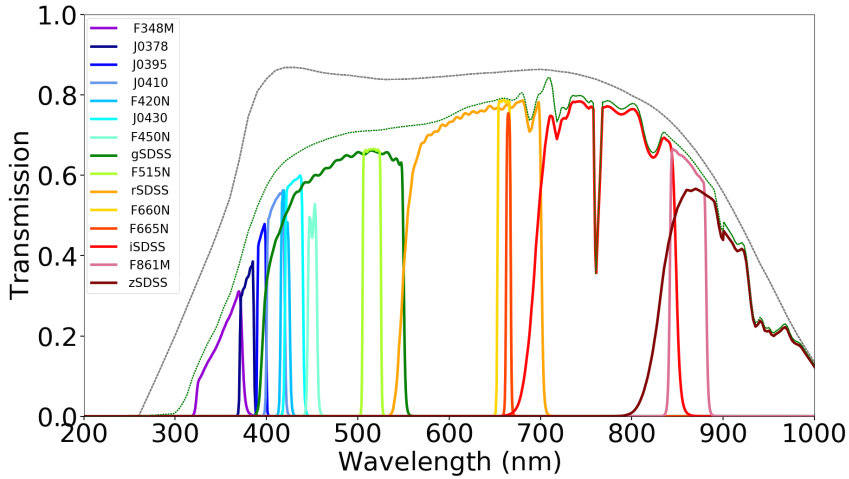


Fig. 4.2 Response functions of the J-PLUS and the GALANTE photometric system filters. In discontinuous grey we represent the response curve of the CCD and mirror, while discontinuous green is the CCD, mirror and atmospheric transmission at 1.3 air mass curve. The *SDSS* response curves are represented by thick colored lines with the other continuous curves are the GALANTE and J-PLUS filter response curves convolved with CCD, mirror and atmospheric transmission at 1.3 air mass.

Using Figure 4.3, we can also explain the function of each GALANTE filter with greater accuracy. Filter F348M is a *u*-like filter disposed to measure the continuum from the left of the Balmer jump. We can combine this one with F420N and F450N to measure the Balmer jump on both sides and derive the T_{eff} of stars. Both filters of our design, F420N and F450N, are the most original (compared to other large-scale recent photometric surveys) of the setup. They have been created to fill the gaps between $H\delta$ and $H\gamma$ and between $H\gamma$ and $H\beta$ respectively. These are the bluest wide regions of the spectrum to the right of the Balmer jump without absorption lines and they provide a measurement of the blue continuum. Another J-PLUS filter used in GALANTE is F515N. It is a Strömgen *y*-like filter positioned in a region free of lines. It can be seen as a V filter for this survey. The next pair of filters, namely F660N (from

J-PLUS) and F665N (own-design), allow us to measure the red continuum, estimate the gravity of hot stars, and flag objects with $H\alpha$ emission. These are two narrow filters centered on $H\alpha$. Specifically, F660N includes the line and F665N just the continuum. The last filter is F861M (from J-PLUS). This is an intermediate filter in the Calcium triplet. It will be used as a detection filter, to obtain the maximum number of stars. We can also use a combination of some GALANTE filters, for a fixed metallicity and extinction law, to obtain effective temperature T_{eff} independently of reddening. Figure 4.4 shows a GALANTE colour-colour diagram using F348M, F420N, F450N, and F515N for stars from 4000 K to 40 000 K with different colour excess $E(4405 - 5495)$ and extinction type R_{5495} .

With our GALANTE configuration, we can describe the system using a response curve defined by the three different transmission curves. Figure 4.1 shows the graphic representation of the optical GALANTE+J-PLUS photometric systems. In order to characterize the GALANTE filter set, we need to describe the filter with some quantitative parameters such as: their isophotal wavelengths, wavelength-weighted average, frequency-weighted average, effective wavelength, root mean square, effective band width, and flux sensitivity. Thus, we define the total response of a photometric system (S_λ) by

$$S_\lambda = T_t(\lambda)T_f(\lambda)T_a(\lambda) \quad (4.1)$$

Here T_t is the mirror+detector throughput; the filter response transmission is T_f ; and the atmospheric curve transmission at 1.3 airmass is T_a .

If the SED received at the the detector, E_λ , is continuous, and the total response S_λ is also continuous and not negative over a range of wavelengths (Golay, 1974), using Equation 4.1 and the mean value theorem, we can say that λ_i exists and has the form of:

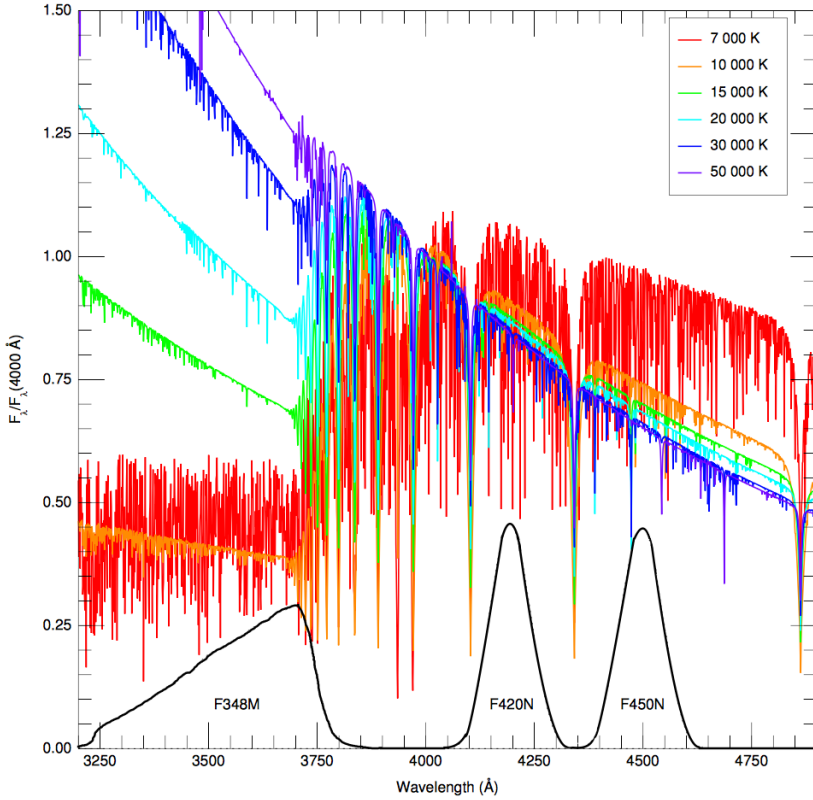


Fig. 4.3 SEDs for main-sequence hot stars normalized to the flux at 4000 Å and sensitivity curves of the three bluest GALANTE filters. F420N and F450N have been approximated by gaussians while F348M has been represented by a rectangular filter with a linear atmospheric absorption effect. Note how F348M measures the continuum to the left of the Balmer jump while F420N and F450N are located at the gaps between the Balmer lines.

$$E_{\lambda_i} \int_{\lambda_a}^{\lambda_b} S_{\lambda} d\lambda = \int_{\lambda_a}^{\lambda_b} E_{\lambda} S_{\lambda} d\lambda \quad (4.2)$$

If we rearrange this equation:

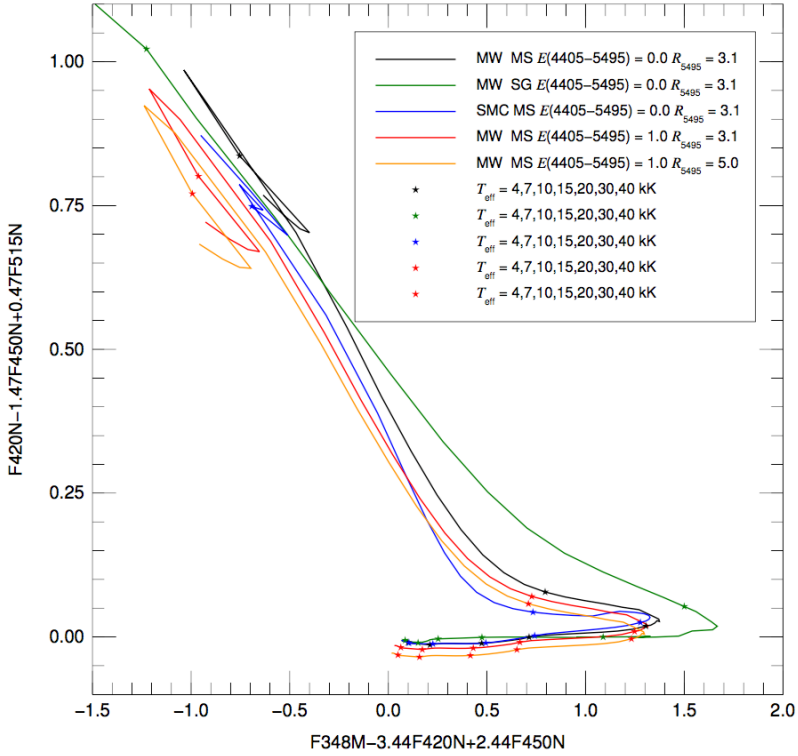


Fig. 4.4 Bracket-like diagram using the GALANTE filter set. It shows how, for a fixed metallicity and extinction law, it is possible to classify the stars by T_{eff} independently of reddening.

$$E_{\lambda_i} = \langle E_{\lambda} \rangle = \frac{\int_{\lambda_a}^{\lambda_b} E_{\lambda} S_{\lambda} d\lambda}{\int_{\lambda_a}^{\lambda_b} S_{\lambda} d\lambda} \quad (4.3)$$

where λ_i is the *isophotal wavelength* and $\langle E_{\lambda} \rangle$ is the mean value of the intrinsic flux above the atmosphere (see also Tokunaga & Vacca, 2005). We show the isophotal wavelengths for Vega using GALANTE+J-PLUS filters in Table 4.2. These values were obtained from Equation 4.3 using the Vega

Table 4.1 Representative Photometric Parameters.

Parameter	Description	Formula
λ_m	Wavelength-weighted average	$\int \frac{\lambda S_\lambda d\lambda}{S_\lambda d\lambda}$
ν_m	Frequency-weighted average	$\int \frac{\nu S_\nu d(\ln\nu)}{S_\nu d(\ln\nu)}$
λ_{eff}	Effective wavelength	$\exp \left[\frac{\int d(\ln\nu) S_\nu \ln\lambda}{\int d(\ln\nu) S_\nu} \right]$
σ	Root Mean Square (rms) of the filters	$\sqrt{\frac{\int d(\ln\nu) S_\nu \left[\ln\left(\frac{\lambda}{\lambda_{\text{eff}}}\right) \right]^2}{\int d(\ln\nu) S_\nu}}$
δ	Effective band width (with n=0)	$2(2\ln 2)^{\frac{1}{2}} \sigma \lambda_{\text{eff}}$
Q	Flux sensitivity	$\int d(\ln\nu) S_\nu$

spectrum provided by [Bohlin \(2007\)](#) and available at ftp://ftp.stsci.edu/cdbs/calspec/alpha_lyr_stis_003.fits, for the optical range.

The isophotal wavelength depends on the Spectral Energy Distribution (SED); thus, for each kind of star it will be different for the same filter. Then we need to define several photometric parameters, as shown in [Table 4.1](#), depending only on the photometric system.

We calculated all those parameters and they are collected in [Table 4.2](#) and [Table 4.3](#) in order to give a precise description of the GALANTE and J-PLUS filters. Note that the GALANTE photometric system is composed of F348M, F420N, F450N, F515N, F660N, F665N, and F861M. In this way,

we put all the 7 GALANTE filters together in Table 4.2, adopting a different nomenclature, but some of them are the same filters used in J-PLUS. The first column shows their GALANTE names, while the second one shows the J-PLUS nomenclature.

Table 4.2 Representative Parameters of the filters of the GALANTE Photometric System.

Filter	$m_{AB}(\text{Vega})$ (mag)	$E_{\lambda_i}(\text{Vega})$ ($\text{erg s}^{-1} \text{cm}^{-2} \text{\AA}^{-1}$)	λ_{iso} (nm)	λ_m (nm)	cV_m^{-1} (nm)	λ_{eff} (nm)	σ	δ	Q	
GALANTE	J-PLUS									
F348M	u/JAVA	1.071	3,215e-09	354.6	354.8	348.5	355.1	0.0422	35.3	0.0286
F420N		-0.238	8,626e-09	420.5	421.5	421.6	421.9	0.0257	25.6	0.0125
F450N		-0.180	8,502e-09	450.5	451.0	451.0	451.2	0.0185	19.7	0.0116
F515N	J0515	-0.049	4,301e-09	515.2	515.4	515.0	515.5	0.0115	13.9	0.0260
F660N	J0660	0.318	1,981e-09	660.4	660.1	660.0	660.1	0.0066	10.3	0.0175
F665N		0.238	1,979e-09	664.7	665.2	665.2	665.2	0.0174	27.2	0.0061
F861M	J0861	0.560	8,185e-10	861.1	861.2	861.0	861.2	0.0137	27.7	0.0296

Table 4.3 Representative Parameters of the additional J-PLUS filters.

Filter	$m_{AB}(\text{Vega})$ (mag)	$E_{\lambda_i}(\text{Vega})$ ($\text{erg s}^{-1} \text{cm}^{-2} \text{\AA}^{-1}$)	λ_{iso} (nm)	λ_{m} (nm)	cv_m^{-1} (nm)	λ_{eff} (nm)	σ	δ	Q
J0378	0.419	6.164e-09	380.1	379.0	378.5	379.1	0.0145	13.0	0.0142
J0395	-0.027	8.052e-09	394.8	395.1	395.0	395.1	0.0102	9.5	0.0115
J0410	-0.165	5.472e-09	410.2	410.4	410.0	410.5	0.0144	14.0	0.0261
J0430	-0.125	7.067e-09	429.7	430.4	430.0	430.4	0.0154	15.6	0.0274
<i>gSDSS</i>	-0.090	5.352e-09	468.7	478.6	480.3	477.0	0.0880	105.3	0.1108
<i>rSDSS</i>	0.163	2.497e-09	618.0	627.6	625.4	622.2	0.0652	104.6	0.1015
<i>iSDSS</i>	0.404	1.301e-09	761.1	769.7	766.8	763.2	0.0592	108.4	0.0766
<i>zSDSS</i>	0.536	9.015e-10	891.7	896.9	911.4	904.9	0.0586	119.8	0.0354

4.2 Standard stars system: The Next Generation Spectral Library (NGSL) and Maíz Apellániz & Weiler (2018) catalogue

To obtain the GALANTE transformation equations, we use two observational catalogues: NGSL (Gregg et al., 2006) and MAW (Maíz Apellániz & Weiler, 2018). The NGSL library comprises of 378 high signal-to-noise stellar spectra. This catalogue has all these stars with a good spectral resolution, all of them homogeneously flux calibrated, covering a large range of spectral types, gravities, and metallicities ($3100 \text{ K} \leq T_{\text{eff}} \leq 32500 \text{ K}$, $0.45 \leq \log(g) \leq 5.4$, $-2.0 \leq [\text{Fe}/\text{H}] \leq 0.5$ and a range of $E(\text{B}-\text{V})$ from 0 to 0.75). The wavelength coverage of these spectra is from 2000 \AA to $10\,200 \text{ \AA}$ at resolution $R \sim 1000$.

NGSL spectra were obtained in the long-slit, first order spectroscopy mode. To cover the optical range of this catalogue, they used 3 gratings (G230LB, G430L, and G750L). Technical description is collected in Table 4.4. At the observations time, STIS has been working during 5 years, so it had a small damage in the CCD detector because of the radiation. After they tried to solve this problem, a systematic error in the flux is estimated in about 10-15%, but applying aperture corrections, it was reduced to 2-3% (Heap & Lindler, 2016).

For this work, we selected the Version 2 of this NGSL catalogue. In that version, they derived the atmospheric parameters with spectral fitting from theoretical models. They normalized the model and spectrum fluxes in the range of 450 and 700 nm to an average of 1.0, minimizing the root mean square. MARCS (Gustafsson et al., 2008) and the Castelli et al. (1997) were the theoretical catalogues selected for the fitting. MARCS catalogue covers temperatures in the range of $2500 \text{ K} \leq T_{\text{eff}} \leq 8000 \text{ K}$ meanwhile models from Castelli et al. (1997) cover $3500 \text{ K} \leq T_{\text{eff}} \leq 50000 \text{ K}$. That is the reason why they applied both grid of models for stars with a $T_{\text{eff}} \leq 8000 \text{ K}$, and Castelli et al. (1997) in $T_{\text{eff}} > 8000 \text{ K}$. In this fitting, they only selected those models

Table 4.4 Description of the three spectral gratings for the NGSL observations from (Heap & Lindler, 2016).

	G230LB	G430L	G750L
Detector	STIS CCD	STIS CCD	STIS CCD
Spectral Range (μ)	0.16-0.32	0.29-0.57	0.52-1.10
Spectral Dispersion ($\text{\AA}/\text{pix}$)	1.35	2.73	4.92
$R = \lambda/\Delta\lambda$	500-1000	530-1040	535-1170
Aperture	52-0.2E1	52-0.2E1	52-0.2E1
Slit Width (arcsec)	0.20	0.20	0.20
Pixel Size (arcsec)	0.05	0.05	0.05

in concordance with the BASTI isochrones (Pietrinferni et al., 2004, 2006). Furthermore, they used for distances the Hipparcos catalogue (van Leeuwen, 2007) updated with a higher precision than in their previous version. Thus, they corrected distances to estimate properly the surface gravities in NGSL stars. In addition, they compared their new atmospheric parameters derived in this way with the common NGSL stars with the Elodie (Prugniel et al., 2007) and with the MILES observational spectral libraries (Sánchez-Blázquez et al., 2006). Heap & Lindler (2016) advice in this paper that even after resolving the absolute measurement of the fluxes, UV spectral region must be corrected. Fortunately, GALANTE only applies into the optical region, being this version of NGSL a perfect candidate to develop this work.

We also take advantage of the new MAW catalogue. It includes stars from CALSPEC, HOTSTAR, and Massa libraries, adding M-type SEDs from Weiler (2018), and Hosey et al. (2015) to complete a 122 stars library. This selection provides us a complete library of hot stars with high extinction, covering a wide range of colours that could be defined by their intrinsic colour or their reddening.

These two catalogues complement each other in the sense of covering the whole range of stellar temperatures observed in an ample grade of extinction, in such a way that the same colour, for example $(g-r)$, could represent an unreddened intermediate-type star or a very reddened early-type object. This complementarity will be crucial when estimating the transformation equations between GALANTE and *SDSS* systems. Once we have obtained synthetic magnitudes from these catalogues, we present some examples of AB magnitudes stars in Table 4.5.

Table 4.5 GALANTE and J-PLUS AB magnitudes example of the 378 Primary Standard Stars from the NGSL.

Star	F348M	J0378	J0395	J0410	F420N	J0430	F450N	gSDSS
G 115-58	13.323	12.973	12.821	12.577	12.519	12.505	12.391	12.329
G 196-48	11.577	11.233	11.143	10.839	10.781	10.761	10.614	10.237
G 202-65	12.564	12.220	12.007	11.771	11.704	11.717	11.622	11.619
HD 002 857	11.725	10.882	10.469	10.294	10.214	10.296	10.229	10.280
HD 008 724	10.720	10.215	10.148	9.528	9.426	9.374	9.015	8.802

Star	F515N	rSDSS	F660N	F665N	iSDSS	F861M	zSDSS
G 115-58	12.205	12.033	12.022	11.982	11.979	12.006	12.020
G 196-48	10.393	10.179	10.152	10.122	10.072	10.062	10.055
G 202-65	11.547	11.529	11.568	11.519	11.575	11.629	11.623
HD 002 857	10.272	10.405	10.491	10.426	10.537	10.586	10.572
HD 008 724	8.510	7.973	7.861	7.832	7.627	7.503	7.461

The AB magnitude system defined by (Oke & Gunn, 1983) has been chosen to set the magnitudes in the GALANTE photometric system.

$$AB_V = -2.5 \cdot \log f_V - 48.60 \quad (4.4)$$

where f_V is the flux per unit frequency of an object in $\text{erg cm}^{-2} \text{s}^{-1} \text{Hz}^{-1}$. The constant is extracted setting AB magnitude equal to V magnitude of the Vega flux:

$$48.60 = -2.5 \cdot \log F_0 \quad (4.5)$$

being $F_0 = 3.63 \times 10^{-20} \text{ erg cm}^{-2} \text{ s}^{-1} \text{ Hz}^{-1}$ the flux of Vega at $\lambda = 5500 \text{ \AA}$ used by those authors. Thus we can write the AB_V magnitudes by:

$$AB_V = -2.5 \log \frac{\int f_V S_V d(\log \nu)}{\int S_V d(\log \nu)} - 48.60 \quad (4.6)$$

where S_V is the total response of the atmosphere, filter, detector, and mirror transmission. Another way to construct this magnitude is using the m_{ST} system to derive a m_{AB} equation as a wavelength function. We adopted the formulation proposed by Casagrande & Vandenberg (2014):

$$m_{AB} = -2.5 \cdot \log \frac{\int_{\lambda_i}^{\lambda_f} \lambda f_\lambda S_\lambda d\lambda}{F_0 \cdot c \int_{\lambda_i}^{\lambda_f} \frac{S_\lambda}{\lambda} d\lambda} \quad (4.7)$$

where c is the speed of light in \AA s^{-1} and f_λ being the flux per unit of wavelength in $\text{erg cm}^{-2} \text{s}^{-1} \text{\AA}^{-1}$. Equation 4.7 is used to obtain AB synthetic magnitudes.

The choice of a spectrophotometric library to perform the calibration of a new photometric system is still a topic open to discussion (i.e. Aparicio Villegas et al., 2010; Bessell, 2011; Koleva & Vazdekis, 2012; Maíz Apellániz & Weiler, 2018; Weiler, 2018). Maíz Apellániz & Weiler (2018) identify differences of zero-point (ZP) between the MAW and NGSL stellar libraries

that can reach up to 0.05 magnitudes for some objects and that on average present an rms of 0.03 magnitudes. However, these differences do not seem to depend on the colour of the stars (Weiler, 2018). For the first calibration of GALANTE photometry we will use both libraries although there could be spurious differences of up to 0.05 mag between the two catalogues.

4.3 Transformation equations from standard stars system

Since the GALANTE project is an optical photometric survey in the optical range, we can think of another useful and well known optical survey to transform GALANTE AB magnitudes. This survey is the *SDSS* (Fukugita et al., 1996; Smith et al., 2002), based on an optical photometric system composed of five bands (*ugriz*) in the range from 3000 Å to 11 000 Å. The GALANTE and *SDSS* photometric systems share the same optical wavelength range, thus we will use the NGSL and MAW catalogues to derive transformation equations between both systems.

It is worth noting that both photometric systems are different in several aspects: number of bands and filter bandwidth, as we show in Figure 4.1. While *SDSS* uses five wide-band filters, GALANTE applies a mix of seven narrow and intermediate-band filter set.

We obtain synthetic photometric GALANTE and *SDSS* AB magnitudes for NGSL and MAW libraries using the response curves shown in Figure 4.2.

Figure 4.5 shows a colour-colour diagram for both catalogues. NGSL stars are represented by red dots while MAW stars are shown in blue dots. We also draw a 1 Myr theoretical PARSEC curve with solar metallicity without extinction from <http://stev.oapd.inaf.it/cmd>, isochrones PARSEC release v1.2S + COLIBRI release PR16 (Marigo et al., 2017). Black triangles represent main locus in *SDSS* photometry from Covey et al. (2007). Looking at both

catalogues in this figure one can see that the MAW library covers a good number of reddened high-temperature stars, showing a sparse distribution for dwarf late-type and giant stars, whereas the NGSL library covers a wider range of temperature and gravity but is limited in reddening. Lastly, in order to derive GALANTE transformation equations that are as general as possible, we use both catalogues as a single one to better probe the diagram of Figure 4.5.

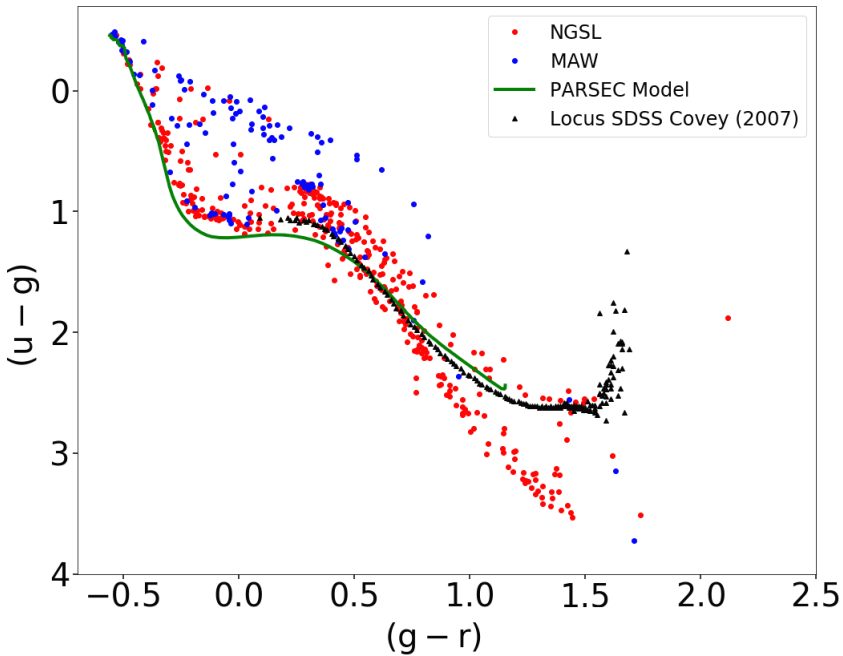


Fig. 4.5 Colour-colour diagram using *SDSS* synthetic photometry for both catalogues. NGSL stars are red dots while MAW stars are shown as blue dots. We draw a 1 Myr theoretical PARSEC curve with solar metallicity and no extinction. Black triangles represent main stellar locus in *SDSS* photometry from Covey et al. (2007).

We have considered the possibility of modeling these transformations through multilinear fitting with the 4 independent *SDSS* colours ($u-g$, $g-r$, $r-i$, and $i-z$). However, a multilinear analysis where the independent variables are not really stochastically independent can introduce significant biases. For

this reason, we first analysed the covariance matrix of both catalogues, which are shown below (Equation 4.8 and 4.9), where we see a high correlation between these 4 colours. Therefore, we have decided to use only a linear fitting to a colour. Equation 4.10 shows the general case, where i indicates the GALANTE bands, k the *SDSS* band, and j specifies the *SDSS* colour used. To select the best fit, we have considered all the possible combinations of *SDSS* colours, choosing the one that shows a lower BIC parameter.

$$NGSL_{corr} = \begin{pmatrix} 1.000 & 0.918 & 0.772 & 0.797 \\ 0.918 & 1.000 & 0.893 & 0.908 \\ 0.772 & 0.893 & 1.000 & 0.991 \\ 0.797 & 0.908 & 0.991 & 1.000 \end{pmatrix} \quad (4.8)$$

$$MAW_{corr} = \begin{pmatrix} 1.000 & 0.842 & 0.810 & 0.826 \\ 0.842 & 1.000 & 0.887 & 0.931 \\ 0.810 & 0.887 & 1.000 & 0.983 \\ 0.826 & 0.931 & 0.983 & 1.000 \end{pmatrix} \quad (4.9)$$

$$Gal_i - SDSS_k = c_{ijk}(SDSS_j - SDSS_{j+1}) + d_{ijk} \quad (4.10)$$

We obtain the transformation equations between the *SDSS* and the GALANTE photometric systems (and vice versa) using the following procedure. To do this, we use AB GALANTE synthetic magnitudes as dependent and the *SDSS* synthetic magnitudes as independent variables. We obtain magnitudes in the GALANTE photometric system from *SDSS* using the statistical package *Statsmodels* in **Python** for this linear fitting. This algorithm provides a goodness of fit parameter called Bayesian Information Criterion (BIC), defined as

$$BIC = -2 \ln L + f \ln(n) \quad (4.11)$$

where n is the sample size of the catalogue, f is the number of free parameters, and L is the likelihood. This parameter has been chosen to select the best solution, choosing that fitting with a lower BIC for each *SDSS* colour. Equation 4.12 summarizes the transformation equations from *SDSS* DR12 to GALANTE photometry.

$$\begin{aligned}
 F348M - u &= 0.149; \text{ rms} = 0.067 \\
 F420N - g &= 0.317 (u-r) - 0.182; \text{ rms} = 0.068 \\
 F450N - g &= 0.125 (g-i); \text{ rms} = 0.027 \\
 F515N - g &= -0.300 (g-r) - 0.032; \text{ rms} = 0.028 \\
 F660N - r &= -0.134 (g-z) + 0.040; \text{ rms} = 0.019 \\
 F665N - r &= -0.138 (g-i) + 0.010; \text{ rms} = 0.009 \\
 F861M - z &= 0.047 (r-z) + 0.005; \text{ rms} = 0.008
 \end{aligned} \tag{4.12}$$

After this fitting we plot the residuals versus $(g-r)$ in Figure 4.6. The residuals have been split for each library. For $(g-r) < 0.3$, the high-reddened hot stars (blue points) are well differentiated from the distribution of red points representing less-reddened intermediate-type stars, especially for the F348M, F420N, F450N, and F660N filters.

If we take a look at these figures, F348M- u , and F420N- g residuals are more scattered than for the other filters, which was expected due to the bands being closer to the Balmer jump. The rms of these residuals is always lower than 6% for both libraries.

The relationship of NGSL residuals with temperature and reddening is shown more clearly in Figure 4.7. Here we have represented fitting residuals versus tabulated NGSL temperature together with its absorption in the visible range (A_v) marked by different colours (<https://archive.stsci.edu/prepds/stisngsl/>,

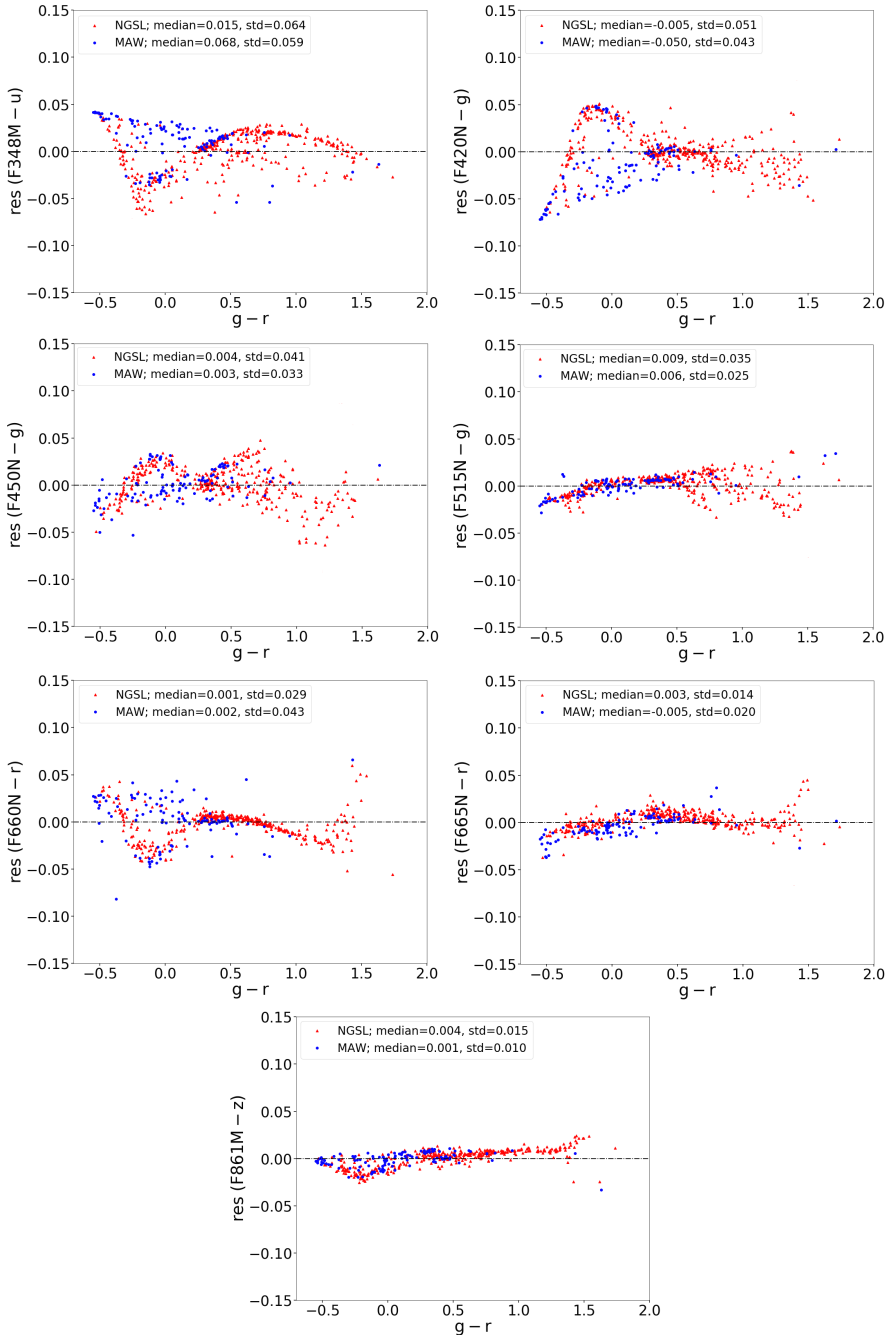


Fig. 4.6 Residual fitting errors for both catalogues from Equation 4.12. NGSL stars are plotted in red dots and MAW stars are shown in blue dots.

Heap & Lindler (2016)). As can be seen, differences due to reddening are not very marked, since in all cases we are limited to values lower than 0.7. However, fitting these transformations by a single colour generates substructures in the residuals, such as those observed in filters F348M, F420N, F450N and F660N. Nonetheless, these transformation equations allow us to establish a first ZP of the GALANTE photometry, which will be very dependent on the SDSS data quality in the regions to be calibrated.

We also estimated the inverse transformation equations from GALANTE to SDSS following the same procedure. The results are shown in Equation 4.13.

$$\begin{aligned}
 u - F348M &= -0.149; \text{ rms} = 0.067 \\
 g - F515N &= 0.591 (F450N - F515N) + 0.025; \text{ rms} = 0.018 \\
 r - F665N &= 0.151 (F450N - F660N) - 0.013; \text{ rms} = 0.013 \\
 i - F861M &= -0.068 (F660N - F861M) - 0.005; \text{ rms} = 0.013 \\
 z - F861M &= 0.205 (F515N - F861M) - 0.055; \text{ rms} = 0.022
 \end{aligned} \tag{4.13}$$

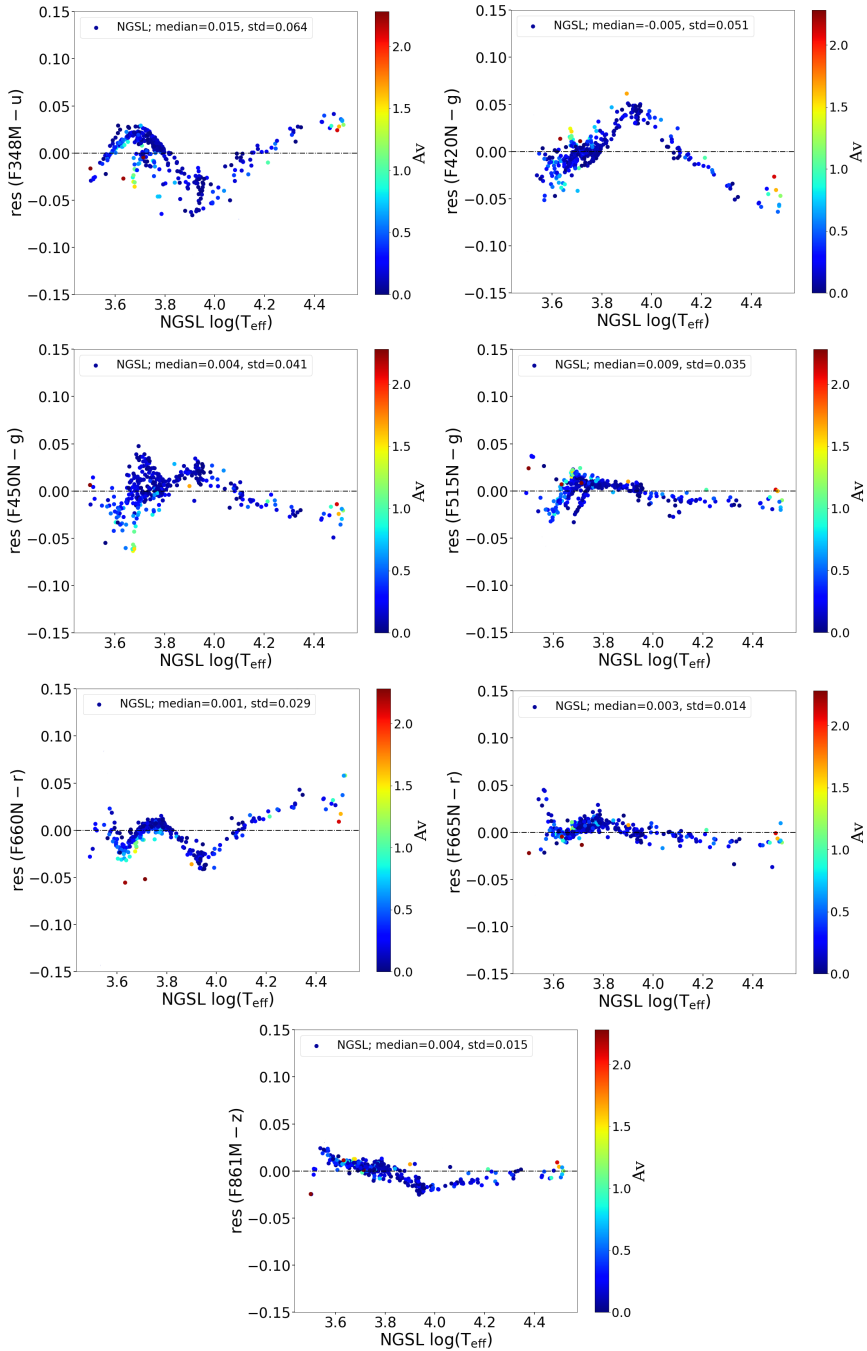


Fig. 4.7 These plots show the residual errors from the fitting depending on the effective temperature and colour excess. The colour map scale represents A_v . Both stellar parameters are extracted from the NGSL library.

4.4 Calibration of the GALANTE photometry

4.4.1 Calibration using SDSS

In this section, we will calibrate the GALANTE photometry for a small region of Cyg OB2, applying transformation equations from Equation 4.12. These data have been obtained over the past 3 years through requests for open observation times from the Javalambre observatory. Data has been previously reduced by the CEFCA team, and aperture photometry has been obtained at the IAA.

We select DR8 and DR12 as possible sources for obtaining GALANTE ZPs through the transformation equations. DR8 has been selected because a previous Cyg OB2 study by [Guarcello et al. \(2012\)](#) was based on this release, while our transformation is based on DR12. Thus we now want to compare both releases in order to see the ZP differences we can obtain using both catalogues.

Firstly, we directly compare *SDSS* photometry in both data releases taking common stars observed with the Javalambre Auxiliary Survey Telescope (hereinafter T-80 telescope). This crossmatch gives a total of 130 stars in Cyg OB2. Figure 4.8 represents the differences between both releases.

Figure 4.8 shows a significant difference in *u* and *g* bands for both releases, showing a light magnitude equation (green dots line) for these two bands. This effect was already known by the *SDSS* team and appeared to be due to the ubercalibration procedure described by [Padmanabhan et al. \(2008\)](#). DR12 was already corrected of this effect. Differences in *r*, *i*, and *z* bands are shown to be lower than a few thousandths of magnitudes and without any evidence of systematic effect. Nonetheless, even though we are observing an equation magnitude between both releases, differences between magnitudes show median values below one hundred, as seen in the histograms of Figure 4.8.

After this analysis, we decided to obtain GALANTE photometry ZPs based on both releases and comparing them afterward. Using both releases, we

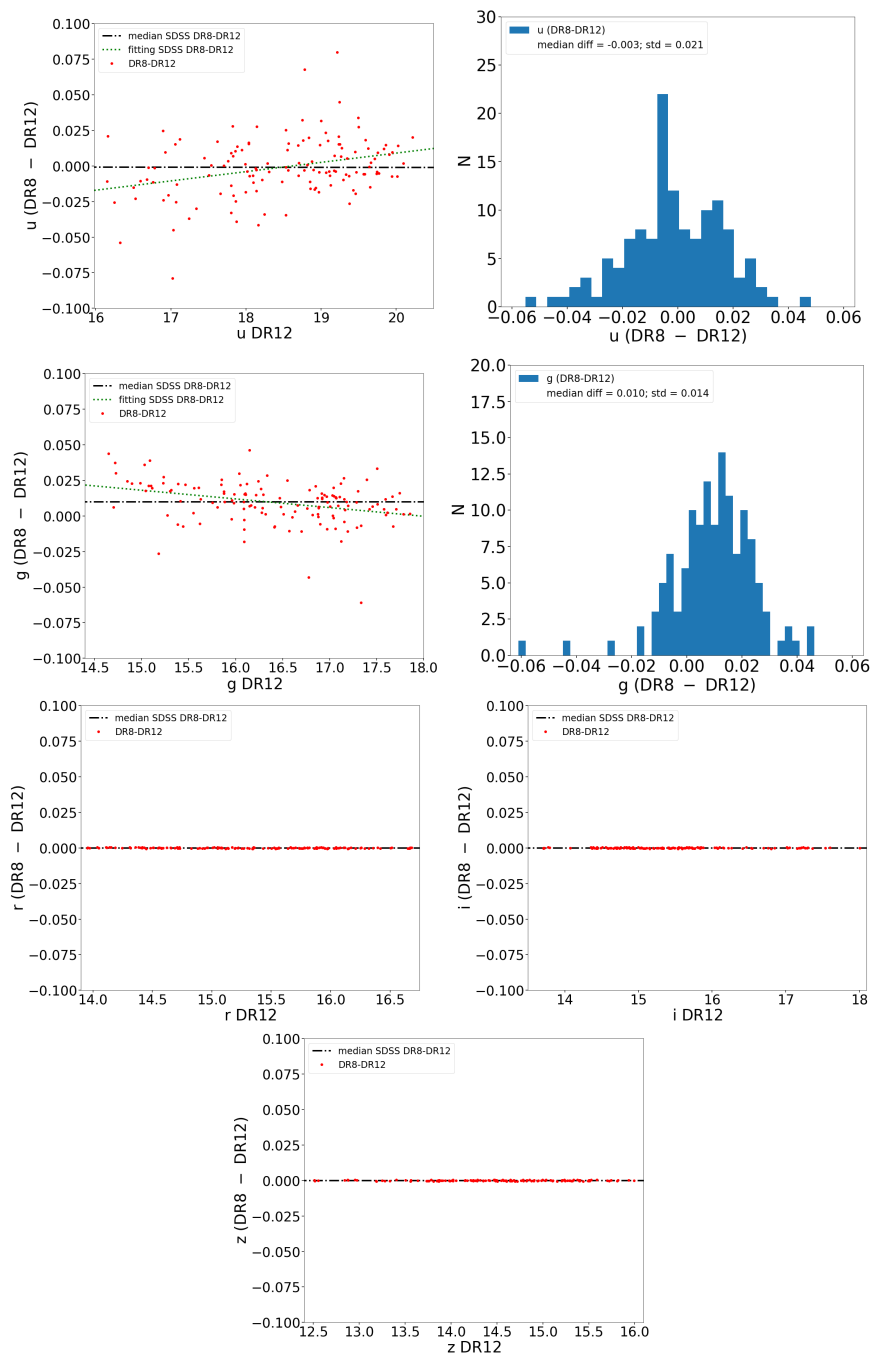


Fig. 4.8 These figures represent differences for stars observed with the Javalambre observatory T-80 telescope in Cyg OB2 and their *SDSS* photometry taken directly from DR8 and DR12.

Table 4.6 GALANTE photometric ZPs from *SDSS* DR8 and DR12.

Band	ZP DR8	error DR8	ZP DR12	error DR12
F348M	26.046	0.004	26.058	0.004
F420N	24.365	0.006	24.349	0.005
F450N	24.496	0.005	24.482	0.005
F515N	26.443	0.004	26.433	0.004
F660N	25.905	0.004	25.907	0.004
F665N	24.057	0.006	24.058	0.006
F861M	26.427	0.003	26.427	0.003

obtain the difference between GALANTE photometries shown in Figure 4.9, where we can see that the median and rms of these distributions are below 0.02 magnitudes for all bands. The final ZPs for each GALANTE band are shown in Table 4.6. Thus, we choose to calibrate GALANTE photometry with *SDSS* data release 12 before to analyze the calibration procedure with the new *RefCat2* catalogue.

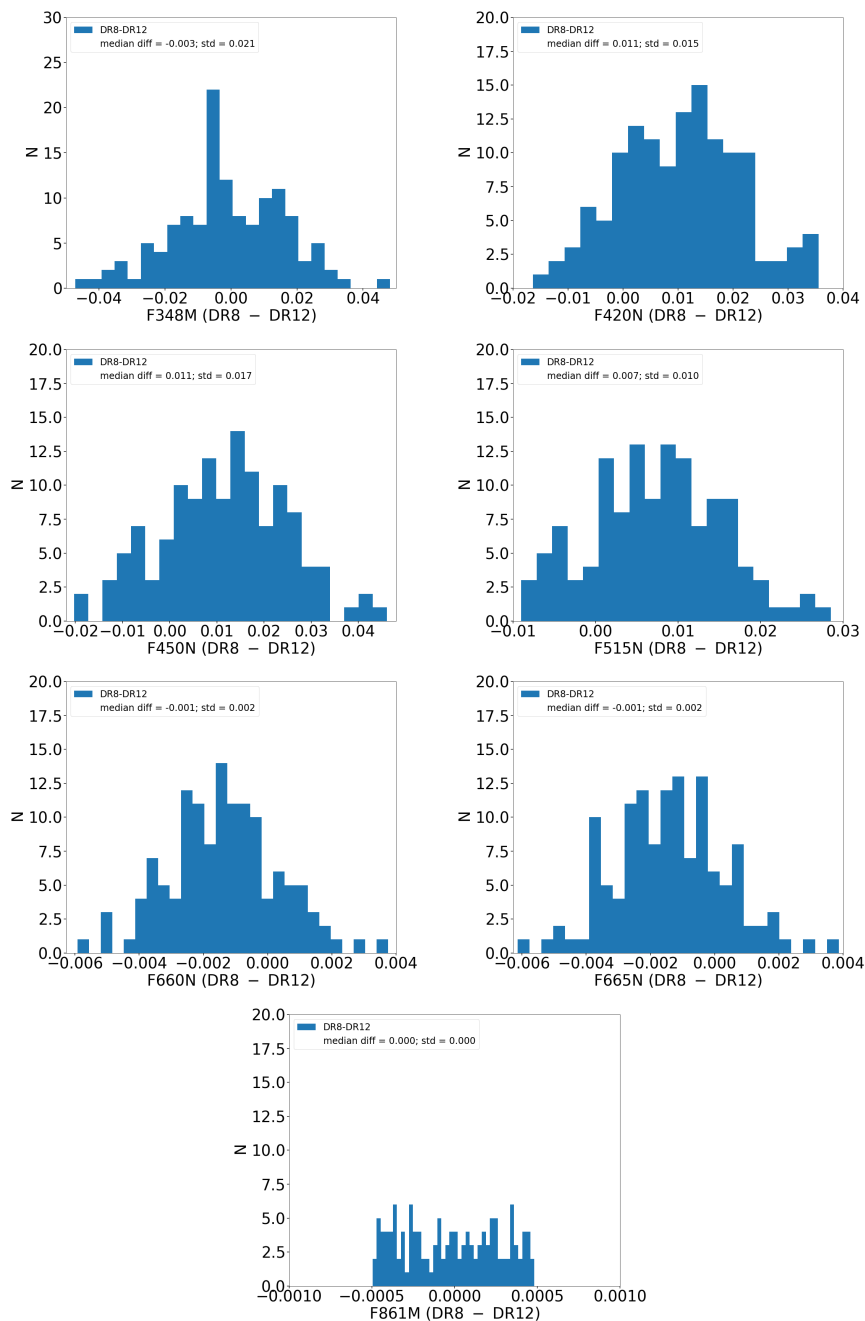


Fig. 4.9 GALANTE photometry histograms for differences between *SDSS* DR8 and DR12 using a small region of Cyg OB2 observed by the T-80 telescope.

4.4.2 Calibration using RefCat2

While we were writing this work, [Tonry et al. \(2018\)](#) published a new catalogue (*RefCat2*) with *griz* photometry of 993 million stars to $m < 19$. According to the authors, *RefCat2* has an internal precision of 0.02 mag for stars in the Galactic disk and is free of systematic effects. In accordance with these premises and at referee's suggestion, we decided to obtain the GALANTE ZPs using this library, however, due to the lack of a *u* band in this catalogue, we have to continue using *u* from *SDSS* DR12. Attending to both libraries, we compare differences between these ZPs in [Figure 4.10](#).

A clear fact to validate this catalogue is that, if these stars present lower systematic errors than those of *SDSS* DR12, this should be translated into the ZP distribution (instrumental - catalogue) for each filter. [Figure 4.11](#) represents GALANTE photometry histograms for these ZP differences comparing with *RefCat2* (in blue) and *SDSS* DR12 (in red). Two facts are clearly observed: *RefCat2* ZPs are more peaked than *SDSS* based ones, and they are also more symmetrical, without the large skews present in the *SDSS* distribution.

Tails that we observe in the ZPs from *SDSS* DR12, suggest the presence of systematic errors for the brightest stars in *SDSS* DR12, as seen in [Figure 4.10](#). After this analysis, and considering that *RefCat2* is an all-sky survey, we consider *RefCat2* our base catalogue to obtain the preliminary calibration of the GALANTE photometric system.

As an example of the obtained results using *RefCat2*, we have drawn the bracket diagram of [Figure 4.4](#) for our Cyg OB2 field. The results are shown in [Figure 4.12](#), where the main and giant sequences by Kurucz as listed by [Castelli et al. \(1997\)](#) are also overplotted. We selected *Kurucz ODFNEW/NOVER* theoretical spectra to obtain the GALANTE synthetic photometry. Kurucz's library provides a coverage of $3500 \text{ K} \leq T_{\text{eff}} \leq 50\,000 \text{ K}$ (in steps of 200 K below $T_{\text{eff}} = 13\,000 \text{ K}$, and 1000 K otherwise), $0.0 \leq \log(g) \leq 5.0$ (in steps of 0.5 dex) and $-2.5 \leq [\text{Fe}/\text{H}] \leq 0.5$ (in steps of 0.2 and

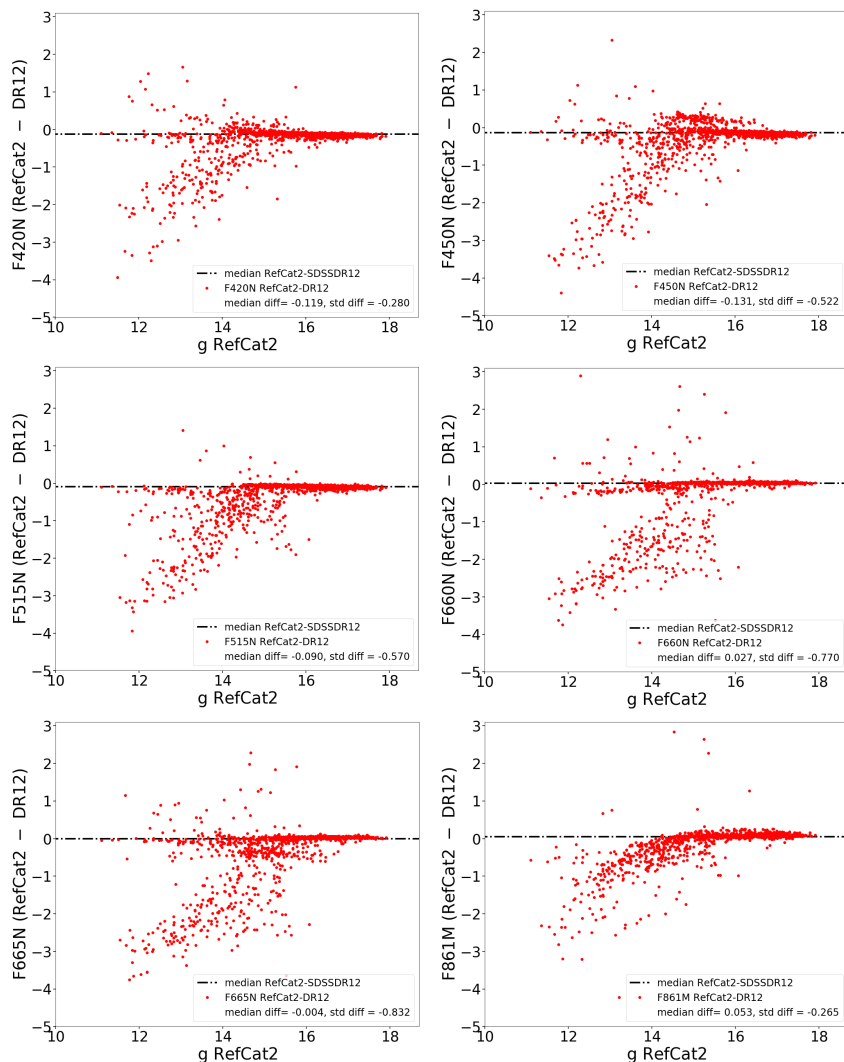


Fig. 4.10 These figures represent differences for stars observed with the Javalambre observatory T-80 telescope in Cyg OB2 and their *RefCat2* and *SDSS DR12* photometry taken directly from both libraries.

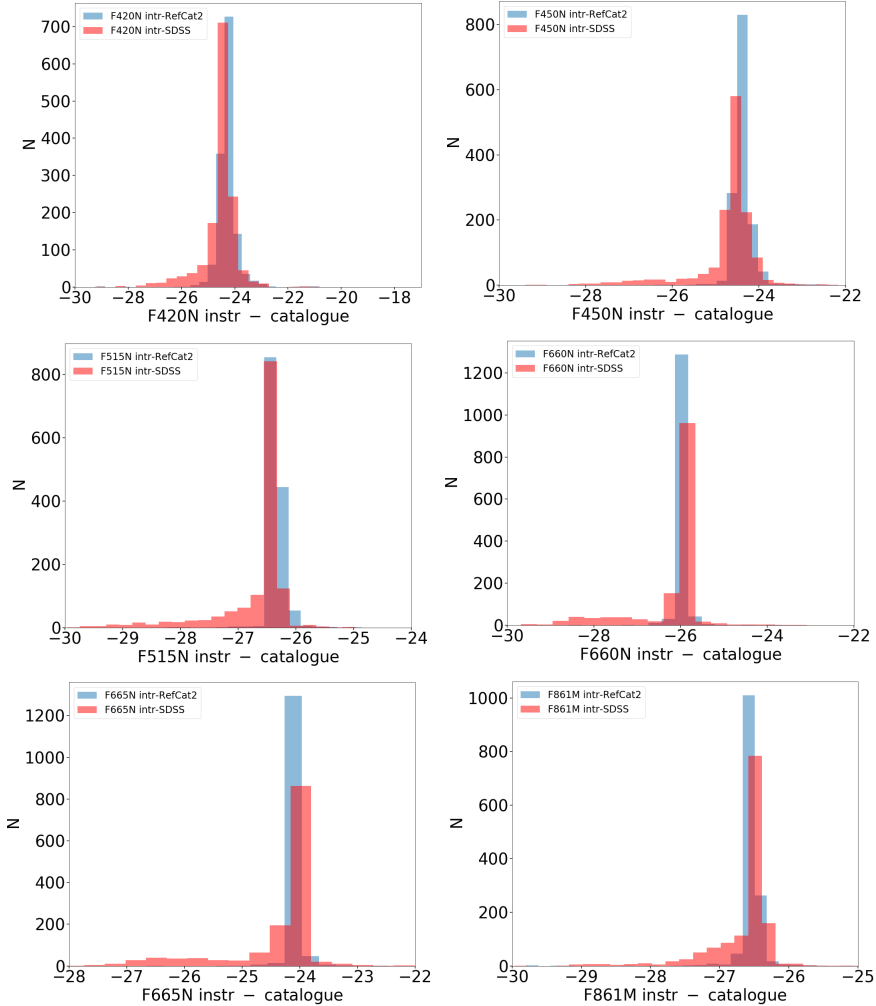


Fig. 4.11 GALANTE photometry histograms for differences between instrumental AB magnitudes minus *RefCat2* (in blue) and *SDSS DR12* (in red) using a small region of Cyg OB2 observed by the T-80 telescope.

0.5). These low-resolution spectra are sampled from 90.9 \AA to 160 \mu m , which includes the GALANTE wavelength range. Solar metallicity, reddening free lines (main sequence: black, and giant: red) are shown.

We observe that most stars are arranged between the two main lines (main sequence and giant stars) and that the most scattered ones could be dispersed due to the high variable reddening and/or ZP error propagation. However, the observed stellar distribution in this plot produces confidence in our ZP choice as a preliminary calibration of the GALANTE photometry. We will compare this calibration with a more sophisticated one in a following paper where we will present the GALANTE photometry of Cyg OB2.

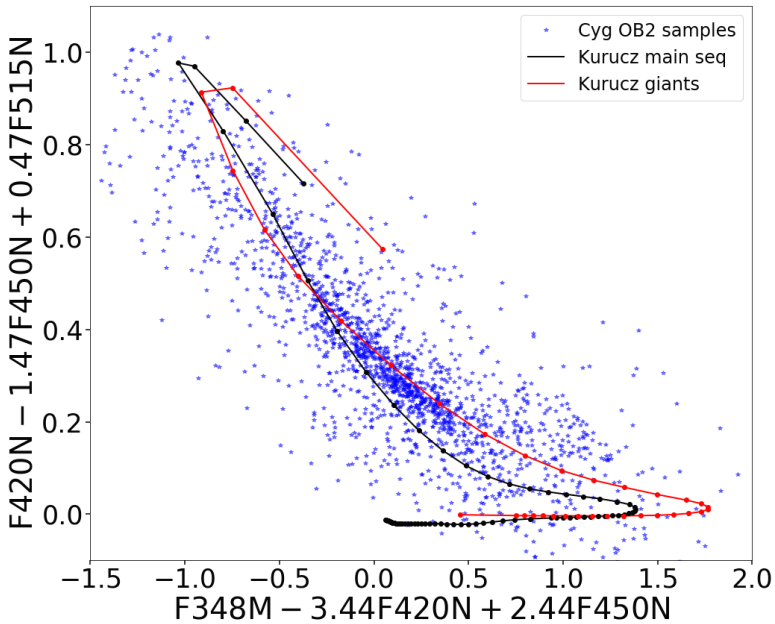


Fig. 4.12 Bracket diagram using GALANTE filter set similar to Figure 4.4. It shows only tracks with solar metallicity models with $\log(g)=4.5$ (black line) and $\log(g)=2.5$ (red line). We represent Cyg OB2 calibrated samples for this work by blue star-shapes.

4.4.3 Conclusions

We present the characterization of the GALANTE photometric system as defined by the convolution of four different response functions: atmosphere, filter, detector, and mirror. The set of primary standard stars to define the GALANTE photometric system is composed of the 378 stars from NGSL library, which cover a wide range of spectral types, luminosity classes and metallicities. We enhance it with the MAW library, which provides a sample of 122 stars. Both libraries provide 500 GALANTE spectrophotometric standard stars. Using this compilation to obtain the GALANTE and *SDSS* synthetic photometries in the AB system, we derive transformation equations from *SDSS* photometry to the GALANTE photometric system (and vice versa) using the BIC parameter as a figure of merit for selecting the best model.

Figure 4.6 shows that a simple *SDSS* model (band+colour; Equation 4.12) is able to shape the GALANTE system up to an rms level of 0.06 magnitudes in the worst case. It is worth noting that our compiled final library covers a wide range of effective temperature, $\log(g)$, metallicity, and, most importantly, reddening. This means that our transformations, despite the noise, can be considered as unbiased. This point is better observed in Figure 4.7, where only NGSL stars are plotted and their dependence on temperature and reddening show a rippled way but limited to an amplitude lower than 0.05 magnitude.

We use Equation 4.12 to obtain the GALANTE photometric ZPs in a field of Cyg OB2 observed using the Javalambre observatory. The ZPs have been obtained from *SDSS* DR8 and DR12 releases. Despite the *u* and *g* magnitude equations between both data releases, the ZP difference is always below 0.01 with an rms of the order of 0.02. During our work, a new *griz* catalogue called *RefCat2* from Tonry et al. (2018) was published. However, the observed stellar distribution of this new catalogue, covering the whole sky, represents an excellent choice for the preliminary calibration of the GALANTE photometry, if, as its authors proclaim, the average internal precision is 0.02 magnitudes

for the stars of the Galactic disk and is free of systematic effects. We have made a comparison between the ZPs obtained from *SDSS* DR12 and *RefCat2*, finding that the distribution of the ZPs derived from *RefCat2* shows a better behavior, with more centralized values and shorter tails (see Figures 4.10 and 4.11). For this reason we adopted *RefCat2* as the base catalogue for GALANTE calibration. The application of the *RefCat2* ZPs to our photometry is shown in Figure 4.12, where the Kurucz's fiducial lines corresponding to main sequence and giant stars of solar metallicity are also overplotted. The agreement between the observed photometry and the theoretical tracks means that we are confident in this ZP calibration.

"What is the point of all of this? To destroy a man who seeks the truth, or to destroy the truth so no man can seek it? Either way, you lose."

X-Files

5

MASTER: Monte-Carlo Astrophysics Studio for galanTE colouRs

Contents

5.1	Data and methods	74
5.1.1	Libraries	74
5.1.2	Magnitudes and colour calculation	76
5.2	Fitting SEDs with MASTER	84
5.2.1	Reduced χ^2 statistic	91
5.3	Theoretical libraries test	92
5.3.1	Reddening free	93

5.3.2	With reddening	95
5.4	Observational tests: NGSL	99
5.4.1	NGSL test with K+T theoretical libraries	100
5.4.2	NGSL test with C+T theoretical libraries	102
5.4.3	NGSL test adding Ko theoretical libraries	106
5.4.4	Results with NGSL without noise	114
5.5	Summary and conclusions	119

Getting intrinsic stellar physical parameters such as effective temperature, gravity and metallicity, as well as extrinsic reddening, is a primary aim for any photometric system. The GALANTE system is no exception. In this paper we analyse how to get the physical stellar properties from the GALANTE photometry by making use of different theoretical and observational stellar libraries. GALANTE provides a new system of 7 intermediate+wide band filters in the optical range of the spectrum (Lorenzo-Gutiérrez et al., 2019; Maíz Apellániz et al., 2019a). The selection of this filter set allows us to get reliable, valuable information on the atmospheric parameters of the stars (Maíz Apellániz, 2017). The GALANTE project presents some peculiarities that distinguish it from other surveys based on different coverage and sampling in the optical range. Some of these differences are mainly based on the observed region of the sky and the limit of magnitude, obtaining photometry that reaches up to 19-20 mag covering the Galactic plane. On the other hand, the definition of the 7 GALANTE filters has been chosen to extract the maximum information about the physical properties of the giant stars in the solar neighbourhood and of the OB stars within the observed magnitude limit. GALANTE has an optimized filter set to measure the Balmer jump to determine T_{eff} for hot stars, using the F348M and F420N filters, including two narrow filters (F660N and F665N) for measuring H_{α} flux.

In this chapter we present an algorithm based on the GALANTE normalized colour fitting to different star libraries covering an extensive range of

physical parameters. The likelihood criterium is the well-know χ_{red}^2 (Barlow, 1989), which has been used for the same purpose in a wide variety of studies (Allende Prieto & del Burgo, 2016; Bohlin et al., 2017; Rodrigo et al., 2019).

One of the fundamental points when determining the physical parameters of a set of stars with a certain photometry is the appropriate choice of the stellar libraries with which they are to be compared. Obviously, the observed stars must be within the set of values that define the parametric space of the models. However, in most cases we do not know beforehand if this condition is satisfied. Another fundamental point, particularly when we work with stars that may be highly reddened, is the choice of the best extinction law that describes the properties of the interstellar medium in the studied region. It is well known that there are regions of the Galactic disk with peculiar dust properties, which would imply a change in the R_{5495} parameter that would define the best model of the interstellar extinction curve (Maíz Apellániz, 2013b; Maíz Apellániz & Barbá, 2018a; Maíz Apellániz & Sota, 2008; Maíz Apellániz et al., 2014).

In this chapter we analyse the capabilities of the algorithm developed to determine the physical stellar properties from the GALANTE photometry. To do this, we use the NGSL observational spectral library (Gregg et al., 2006) as a sample test to estimate the precision and uncertainties of the derived parameters, comparing with 4 different sets of stellar models that cover a wide range of spectral types, luminosity classes, and chemical composition. This analysis provides us information about the best selection of models for the obtaining of physical stellar parameters free from bias and with better internal precision. We want to answer, for example, whether it is better to compare the observations with the whole set of available stellar models or if, on the contrary, a previous selection is needed to ensure a better result. Thus, we focus this study on the development and description of an algorithm for obtaining the physical stellar properties and the analysis of how different

libraries of stellar models can give different results, introducing, in some cases, a considerable bias.

5.1 Data and methods

5.1.1 Libraries

Theoretical stellar libraries

Since the GALANTE project is mainly designed for the study of the Galactic disk (Lorenzo-Gutiérrez et al., 2019; Maíz Apellániz, 2017; Maíz Apellániz et al., 2019a), the set of theoretical models that will be used to determine the physical parameters of the sample objects should be focused mainly on the most characteristic stars of this Galactic subsystem. To this end, we select the C, K, and TLUSTY *OSTAR2002* (Lanz & Hubeny (2003); hereinafter T) theoretical libraries. C's library covers T_{eff} from 3000 K to 25 000 K (in steps of 200 K below $T_{\text{eff}}=4000$ K, 1000 K above $T_{\text{eff}}=12\,000$ K and 250 K otherwise), with $\log g$ between 0.5 and 5.5 (in steps of 0.5 dex) and $[\text{Fe}/\text{H}]$ from -1.3 to 0.2, modelling these parameters for two α -enhanced values (0.0 and 0.4), and for wavelengths between 1300 and 10 000 Å. K's catalogue provides a coverage of $3500 \text{ K} \leq T_{\text{eff}} \leq 50\,000 \text{ K}$ (in steps of 200 K below $T_{\text{eff}} = 13\,000 \text{ K}$, and 1000 K otherwise), $0.0 \leq \log g \leq 5.0$ dex (in steps of 0.5 dex) and $-2.5 \leq [\text{Fe}/\text{H}] \leq 0.5$ (in steps of 0.2 and 0.5 dex). The range of wavelengths in K is from 1000 Å to 10 μm for low resolution spectra. T is another library that especially covers O stars¹, and that therefore enables a better redefinition of the space of parameters for the higher temperatures. The temperature range goes from $27\,500 \text{ K} \leq T_{\text{eff}} \leq 55\,000 \text{ K}$ (in steps of 2500 K), $3.0 \leq \log g \leq 4.75$ (in steps of 0.25 dex) and $[\text{Fe}/\text{H}]$ from 0.0 to 2.0 dex where the accurate calibrated spectra is limited to the 3000-7500 Å wavelength range. In order to extend our grid of models to another type of stars, we select the

¹http://svo2.cab.inta-csic.es/theory/newov/index.php?model=tlusty_mergedbin

KOESTER (hereinafter Ko) white dwarf (WD) theoretical catalogue (Koester, 2010). This theoretical library contains WD spectra whose atmospherical parameters cover T_{eff} from 5000 to 80 000 K in 250 K steps until 20 000 K, in 1000 K steps from 20 000 K to 30 000 K, in 2000 K steps until 40 000 K, in 5000 and 10 000 K steps until 80 000 K. $\log g$ ranges from 6.5 to 9.5 in 0.25 dex steps from 0.9 to 3000 nm.

Figure 5.1 is a graphical representation of the range of physical stellar parameters for each theoretical library.

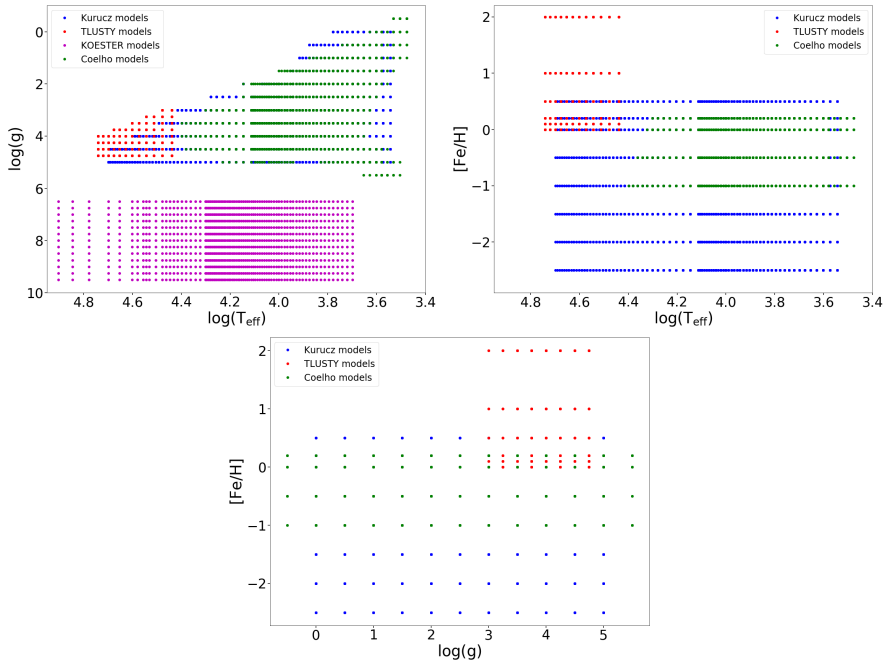


Fig. 5.1 Range of physical stellar parameters for the theoretical libraries. Each library is coded by colours.

Observational stellar library: NGSL

We have chosen the NGSL library (Gregg et al., 2006), which comprises spectra for 378 stars, covering the spectral range from 0.2 to 1.0 μm well calibrated in flux. This catalogue covers a range of $3100 \leq T_{\text{eff}} \leq 32\,900$ K, $0.4 \leq \log g \leq 5.4$ dex and $-2.0 \leq [\text{Fe}/\text{H}] \leq 0.5$ and $E(\text{B}-\text{V})$ from 0 to 0.75. One can see how the physical stellar parameters of this observational library are representative of the three major subsystems of the Galaxy. Therefore, we choose this observational catalogue as input to compare with model libraries. NGSL data have been used for similar purposes in some previous studies (Aparicio Villegas et al., 2010; Heap & Lindler, 2016; Mann & von Braun, 2015; Weiler, 2018). As an example of SEDs that we use in this comparison with models, in Figure 5.2 we show two NGSL spectra in normalized magnitudes. They are representative of the tips in the NGSL effective temperature distribution.

In our study, we excluded those stars catalogued as *suspect* by Heap & Lindler (2016) from the NGSL library. These spectra show a poor fit with the models used by these authors to estimate their physical parameters. Those stars classified as *binary* by Koleva & Vazdekis (2012) have also been removed from our analysis. Thus, our final sample consists of 251 objects that, classified by range of spectral types, are as follows: OBA ($T_{\text{eff}} > 8000$ K, 67 stars), FGK ($4000 < T_{\text{eff}} \leq 8000$ K, 164 stars) and M ($T_{\text{eff}} \leq 4000$ K, 20 stars). In this paper we will use the physical variables listed by Koleva & Vazdekis (2012) in their Table 1, having removed the aforementioned stars.

5.1.2 Magnitudes and colour calculation

We determine the synthetic AB GALANTE magnitudes of both the theoretical and the observational libraries following the procedure described in Lorenzo-Gutiérrez et al. (2019). With these magnitudes, we build the SEDs, normalizing them to the central wavelength band 515.5 nm. This definition of

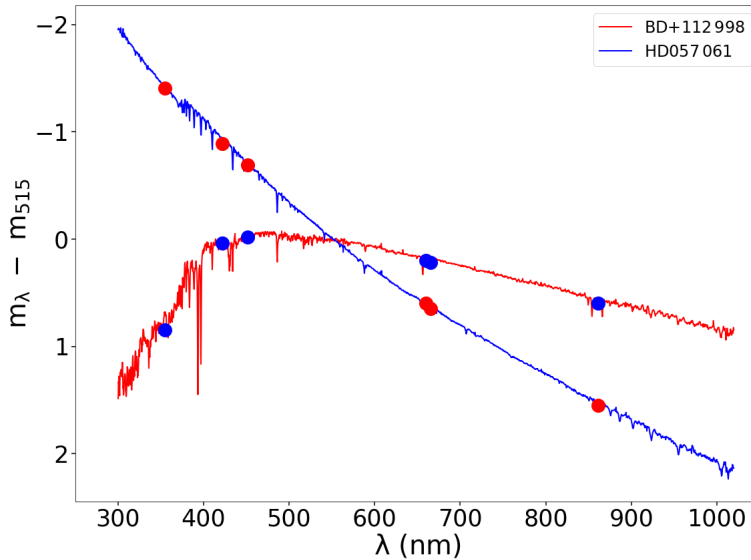


Fig. 5.2 Two NGSL spectra in normalized magnitudes. They are representative of the tips in the NGSL effective temperature distribution.

normalized SED allows us to work with different stellar models whose energy emission is given in different ways, such as brightness between the Coelho low-resolution models (hereinafter C) (Coelho, 2014) and those of Kurucz (hereinafter K) (Castelli et al., 1997). The use of colours defined as $m_\lambda - m_{515}$ remove this problem, as well as the dependence on distance when comparing the observational SEDs with theoretical models. That is, we adopted the same approach as that chosen by Allende Prieto (2016) to solve a similar problem.

In this paper, we will refer interchangeably to these colours as GALANTE normalized colour and GALANTE normalized magnitude.

In order to learn the properties of these theoretical libraries in depth, we carry out an analysis of the flux ratios of the different models for stellar objects with the same physical parameters. In particular, we analyse in more detail the C and K models, which cover the largest range of physical parameters. First,

we choose the intersection of models with the same three physical variables, selecting them a set of 1155 spectra.

In this first exercise, we take those models with solar metallicity $[Fe/H]=0.0$. Figure 5.3 represents the fluxes ratio in normalized magnitudes for different spectral types and luminosity classes. Superimposed on this plot, we draw the transmission curve of the different GALANTE filters.

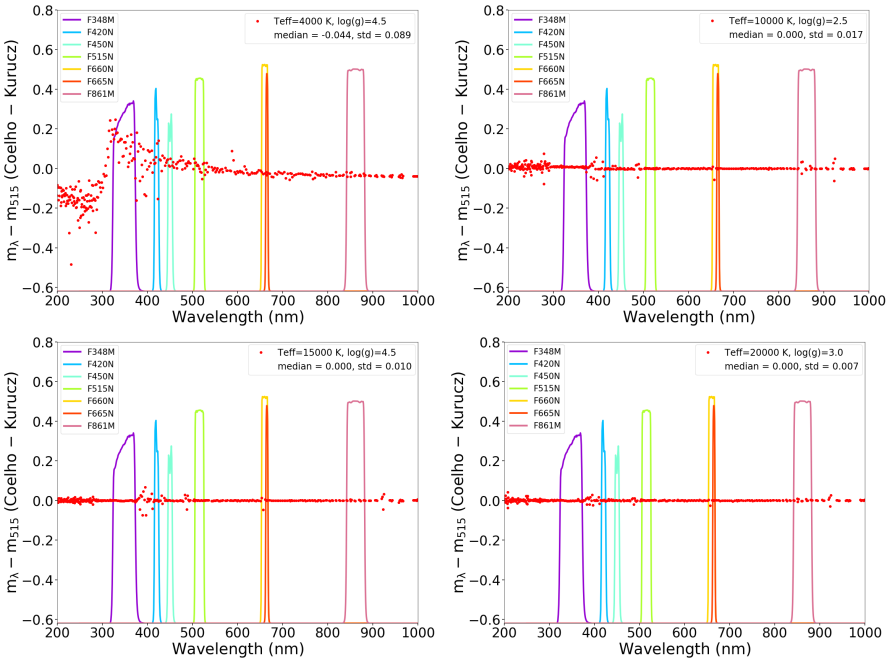


Fig. 5.3 Red dots represent differences between C and K libraries in normalized magnitudes. Colour lines are transmission curves for GALANTE filters, which have been properly scaled to fit the plot.

Regarding Figure 5.3, the most remarkable features can be summarized as follows: a) the main differences are obtained for the cold stars, decreasing the bias and the error (measured by the standard deviation) as we increase the temperature; b) these differences are mainly found for the wavelength range

corresponding to the near-ultraviolet side and other closer bands located on the other side of the Balmer jump. This plot already suggests that the determination of the observational physical parameters obtained from these different model catalogues could give different results especially for low-temperature stars. In all panels of Figure 5.3 we have included the median and standard deviation of these differences.

As we show in Figure 5.4, the major differences in normalized magnitude are mainly due to the spectral type and not to the luminosity class, since for both a giant and a 6000 K main sequence (MS) star the differences between the two models are almost identical. The comparison of models for the same luminosity class shows that this stellar parameter is not critical against the effective temperature.

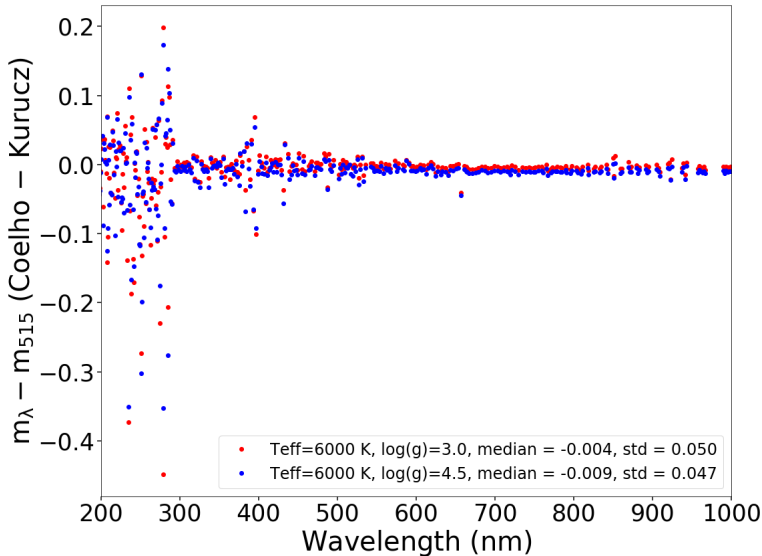


Fig. 5.4 In blue dots the normalized magnitude difference for a MS star with 6000 K; red dots represent differences for a giant star model with the same temperature.

This analysis is now shifts to the SEDs defined by the GALANTE normalized colours for the 1155 models selected above. Here we refer to the residual differences that are obtained as the median of the residuals for each colour.

Figure 5.5 presents the differences of GALANTE normalized colours for each pair of models (C and K). In the top panel we observe that, for objects with $\log(T_{\text{eff}}) < 3.65$ the standard deviation of the values exceeds 0.05 mag, a situation that only occurs again for models with a T_{eff} close to 6000 K. The bottom panel shows how these differences are almost invariant versus luminosity class for a wide range of metallicities. Only stars with $\log g=5.0$ show a higher dispersion since they cover the highest range in T_{eff} .

If we perform this same analysis with K and T, we find that the differences in colours are greater for the range of temperatures in common, while the dispersion in the differences of colours decreases for the range of $\log g$ analysed, as we can see in Figure 5.6.

Regarding the differences in the GALANTE colours versus $\log g$, we see a similar effect to the previous one, but with standard deviations smaller than in the C - K comparison. Metallicities here are not segregated in this group of models, mainly because metallicities are limited to a lesser range of values. This effect means that models are indistinguishable with this methodology as far as these parameters are concerned.

Figure 5.7 shows the differences of normalized magnitudes for each GALANTE colour between C and K common models. For simplicity, Table 5.1 shows the correspondence between GALANTE colour and a numerical code.

It is a remarkable result that, despite the fact that all colour differences are obtained close to 0.0, there is a systematic deviation towards negative values, which indicates that the C library shows values of colours somewhat higher than those obtained with the K catalogue. Another remarkable fact is the error of 2% that occurs in the first colour (F348M-F515N), corresponding to the bluest GALANTE band F348M, which is responsible for the measurement

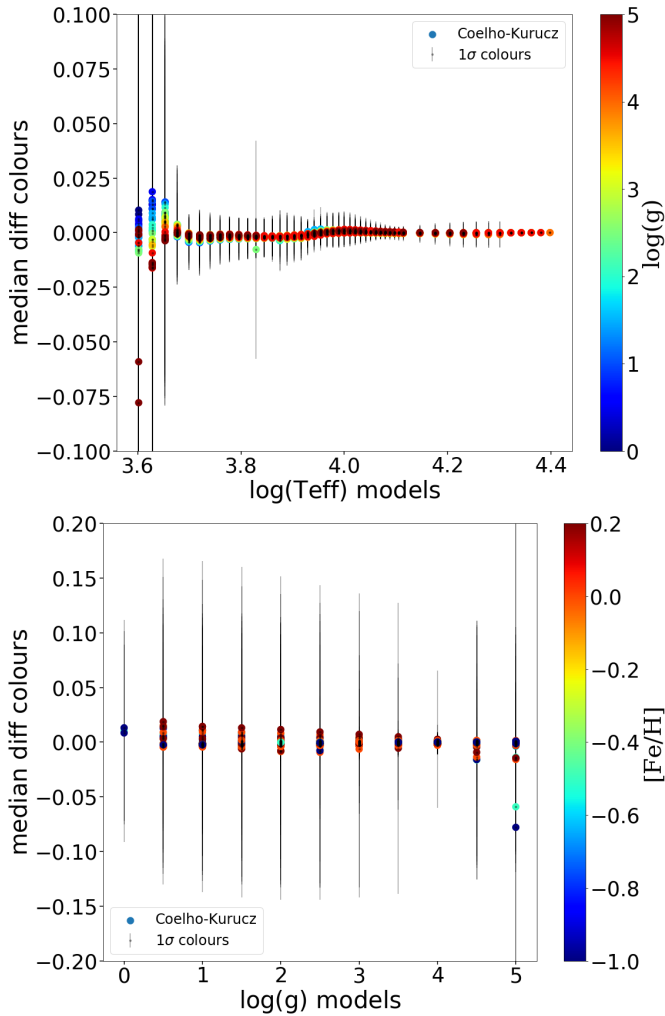


Fig. 5.5 Differences between GALANTE normalized magnitudes for each pair of models (C and K). The top panel shows how for temperatures lower than 4500 K the differences are larger. In the bottom panel, we can see how metallicity is not an important factor affecting the main difference, excepting for $\log g=5.0$, where low $[\text{Fe}/\text{H}]$ values seem to show a negative bias with a larger dispersion.

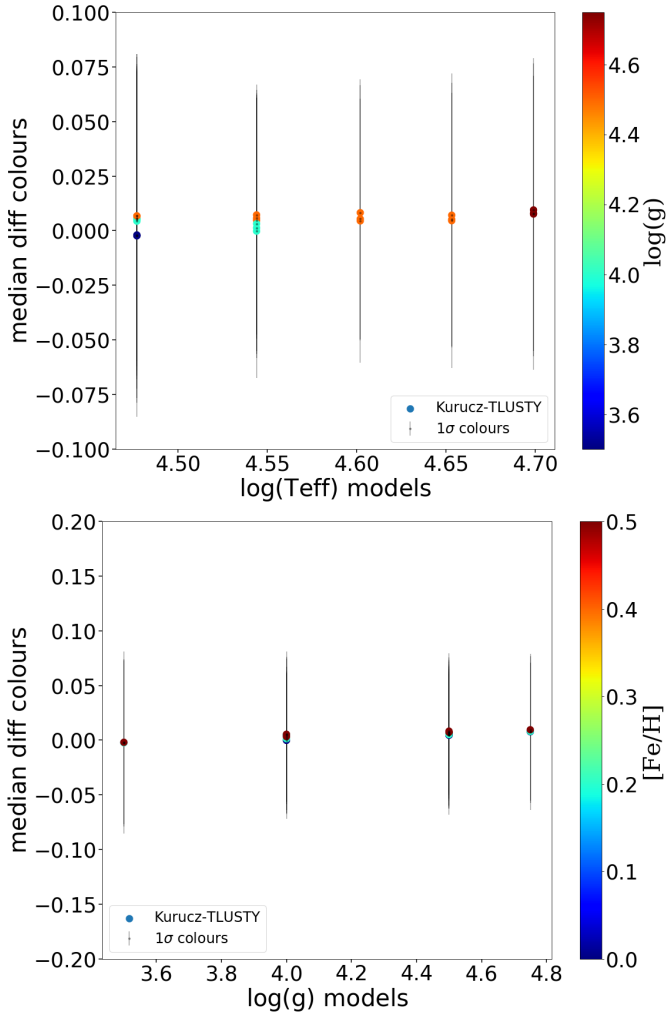


Fig. 5.6 Same as Figure 5.5 but for models K and T. In the top panel, we can see how the dispersion is similar for all temperatures but much larger than that reported for C and K, for temperatures larger than 4500 K. In the bottom panel, we observe that the differences do not show a clear bias.

of the T_{eff} , while the 2 following colours (F420N-F515N and F450N-F515N), also involved in this estimation, are closer in the model comparison.

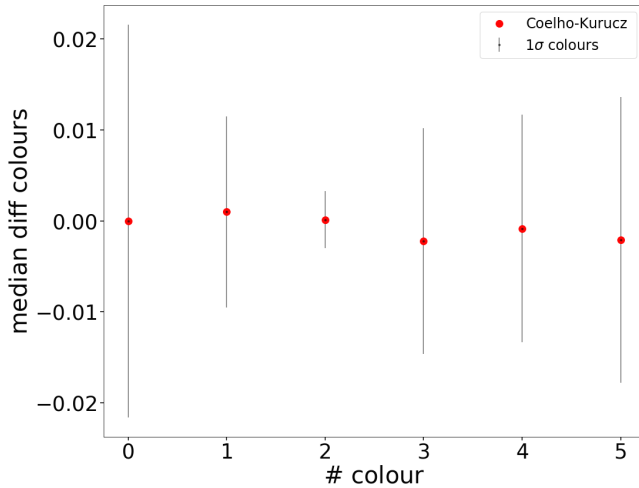


Fig. 5.7 Differences of normalized magnitudes for each GALANTE colour between C and K common models.

Attending to the K - T model comparison, we see a systematic deviation in the more blue and red optical bands of GALANTE. As we see in Figure 5.8, for the bluest colour differences of 3% are prevailing, dominating T, while in colour 5 (F861M-F515N) it is the colours of K that generate these discrepancies. However, we do not see deviations that differ from the observed Figure 5.7, between the C and K models. The differences seen in Figure 5.8 are within 0.01 mag for all colours except for 0 and 5. In the case of F348M-F515N, the analysis of [Maíz Apellániz et al. \(2014\)](#) showed that the T values for the colours associated with the Balmer jump agree with the spectroscopic values for T_{eff} , so the differences around -0.03 mag are likely caused by the K values being incorrect. On the other hand, for F515N-F861M the T models do not include a detailed atmospheric treatment at the wavelength range to the right of the Paschen jump, so that is the likely culprit for the difference.

We do not compare the models from C and T because there is no coincidence in effective temperatures between them.

Table 5.1 Colour code.

# colour	GALANTE colour
0	F348M - F515N
1	F420N - F515N
2	F450N - F515N
3	F660N - F515N
4	F665N - F515N
5	F861M - F515N

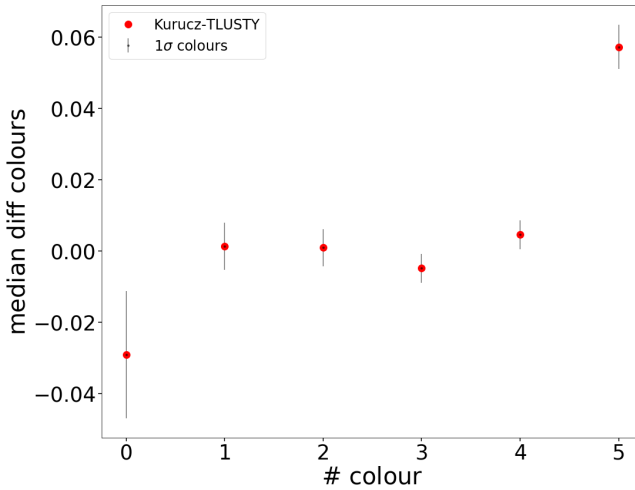


Fig. 5.8 Differences of normalized magnitudes for each GALANTE colour between K and T common models. We can see how the colours 0 and 5 show a clear bias mainly affecting the reddest and bluest colours.

5.2 Fitting SEDs with MASTER

The main idea underlying this work is to extract as much information as possible from the GALANTE photometry using theoretical and observational

libraries. For this purpose, we use the GALANTE normalized colours and we obtain synthetic photometry using theoretical and empirical libraries, applying χ_{red}^2 (hereinafter χ^2) methodology to compare.

The four physical variables we want to determine are: effective temperature, gravity, metallicity, and colour excess using the observational GALANTE photometry. We present the MASTER procedure (Monte-Carlo Astrophysics Studio for galanTE colouRs), using the previous theoretical catalogues as models libraries and the NGSL observational catalogue as input of observed stars to test them. Observational gaussian noise is introduced in the procedure through a Monte-Carlo simulation affecting model spectra; in other words, we translate the observational noise to a Monte-Carlo random deviation of the models. We generate a set of reddened models, which in the first approximation is comprised between $E(4405-5495)=0.0$ and 3.0 divided into 80 steps. The first temperature determination is made using this model grid. Once this temperature is obtained (T_{eff}^1), we again choose a set of models with temperatures between that T_{eff}^1 and $\pm 15\% \cdot T_{eff}^1$ with $E(4405-5495)$ between 0.0 and 3.0 , this time with a 200-step grid. The precision of the photometry is introduced in the same way as in the first step. In this way, we obtain the final solution. The generation by means of the Monte-Carlo method of 50 samplings for each model allows us to obtain a measure of the internal precision of our estimation following a method similar to the bootstrap. The colours are reddened with the extinction law defined by [Maíz Apellániz et al. \(2014\)](#) which is especially valid for regions of massive star formation. In the [Table 5.2](#), we show the number of cells of each model mesh used in this work, for both the first run and the second run. We chose four combination of models: K+T, K+T+Ko, C+T, and C+T+Ko. In the second run the number of cells is variable depending on the T_{eff} derived in the first estimate. In the column corresponding to the second run, we list the maximum and minimum number of cells that we can find in each case. The number of cells is estimated as $N_{T_{eff}} \times N_{\log g} \times N_{[Fe/H]} \times N_{E(4405-5495)} \times N_{Monte-Carlo}$.

Table 5.2 Number of cells of each model mesh used in this work, for both the first run and the second run.

	K + T	K + T + Ko	C + T	C + T + Ko
1 st run, cells	83x15x11x80x50	123x28x11x80x50	65x17x8x80x50	96x30x8x80x50
2 nd run, min. cells	9x6x11x200x50	8x19x11x200x50	5x5x6x200x50	5x18x6x200x50
2 nd run, max. cells	7x11x8x200x50	9x23x8x200x50	9x9x4x200x50	9x22x4x200x50

In this way, for each physical variable we obtain 3 representative core values: a) the value corresponding to the best fitting; b) and c), the mean and median of each of the 50 Monte-Carlo realizations for each model and each step of E(4405-5495), as well as the standard deviation of each of the physical variables. It is evident that since we do not perform any interpolation between the models, the precision in the determination of the physical variables is mainly determined by the size of the four-dimensional cells of the models.

A flux diagram of this methodology is shown in Figure 5.9, where each of the steps followed in the determination of these physical variables is detailed.

The steps that we follow are:

- 1- doing synthetic GALANTE photometry with theoretical and empirical libraries
- 2- obtaining GALANTE colours from the libraries
- 3- applying a grid of colour excess to the theoretical synthetic colours, creating a grid of reddening theoretical colours using [Maíz Apellániz et al. \(2014\)](#) extinction law, using a grid of E(4405-5495) from 0.0 to 3.0, with 80 equidistant values
- 4- generating a gaussian error from the instrumental and calibration magnitude for each GALANTE colour
- 5- using the statistical χ^2 as criterion figure to discriminate which model of the theoretical star colours fits better with each empirical star colours, for each value of E(4405-5495)

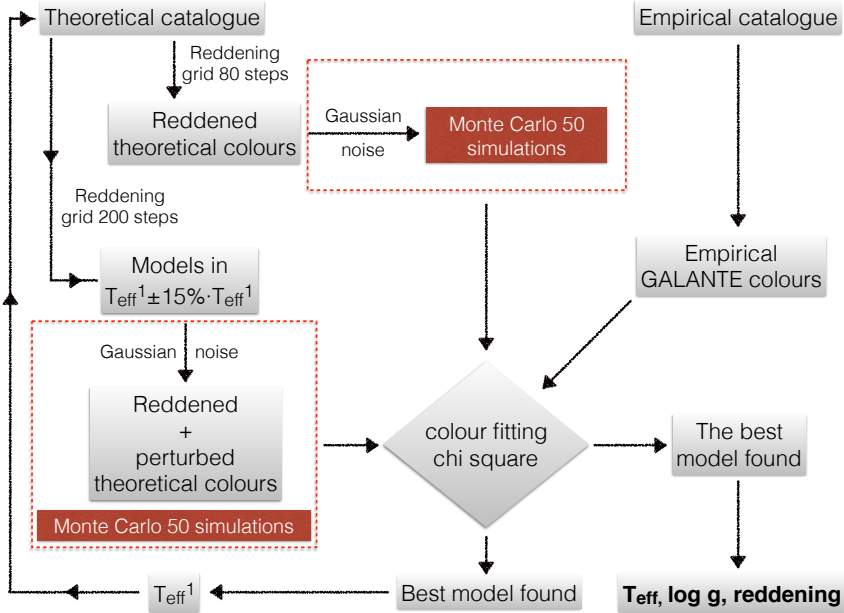


Fig. 5.9 Flux diagram for MASTER algorithm.

6- once T_{eff} is found (T_{eff}^1), redo this χ^2 criteria, entering in the models of stars with $T_{\text{eff}}=T_{\text{eff}}^1 \pm 15\% \cdot T_{\text{eff}}^1$, reddening with 200 steps from 0 to 3.0 of E(4405-5495)

7- put in this method from the step 3, in a Monte-Carlo route (50 simulations).

Let's now explain the method in detail. We start having the colours of theoretical libraries and empirical colours from NGSL catalogue. These models are computed without interstellar absorption (reddening), we want to create a grid as much realistic as possible. To be able to compare with the empirical colours, previously we need to apply a reddening to the theoretical colours. Thus, we first introduce the path of applying a reddening to an unreddened colour. Using the notation of empirical (*emp*) and model (*mod*) referring to a reddered and not reddered flux respectively, we can write

$$F_{emp}(\lambda) = F_{mod}(\lambda) \cdot 10^{-0.4 \cdot E(4405-5495) \cdot k(\lambda)} \quad (5.1)$$

We define an AB magnitude from flux as:

$$m_{AB} = -2.5 \cdot \log_{10}(F(\lambda)) - 48.6 \quad (5.2)$$

Therefore, applying this to the reddered and unreddered fluxes in Equation 5.1 we can obtain the AB magnitude from a filter and its following. The first one will be:

$$-2.5 \cdot F_{emp}(\lambda^G) = -2.5 \cdot F_{mod}(\lambda^G) \cdot 10^{-0.4 \cdot E(4405-5495) \cdot k(\lambda^G)} \quad (5.3)$$

and for the normalization filter:

$$-2.5 \cdot F_{emp}(\lambda^{G_p}) = -2.5 \cdot F_{mod}(\lambda^{G_p}) \cdot 10^{-0.4 \cdot E(4405-5495) \cdot k(\lambda^{G_p})} \quad (5.4)$$

where λ^G refers to each GALANTE filter of the colour generated excluding F515N filter, and λ^{G_p} refers to the pivot GALANTE filter F515N.

Using the notation of m_{AB} , and renaming the AB magnitude of an empirical star as m_{emp} and m_{mod} being the AB magnitude for a model star, equations 5.3 and 5.4 take respectively the form:

$$m_{emp}^G = m_{mod}^G + 2.5 \cdot 0.4 \cdot E(4405 - 5495) \cdot k(\lambda^G) \quad (5.5)$$

$$m_{emp}^{G_p} = m_{mod}^{G_p} + 2.5 \cdot 0.4 \cdot E(4405 - 5495) \cdot k(\lambda^{G_p}) \quad (5.6)$$

Subtracting equation 5.5 - 5.6:

Table 5.3 Effective wavelength of the GALANTE photometric system filter set.

Filter	F348M	F420N	F450N	F515N	F660N	F665N	F861M
$\lambda_{eff}(\mu\text{m})$	0.3548	0.4215	0.4510	0.5154	0.6601	0.6652	0.8612

$$m_{emp}^G - m_{emp}^{G_p} = m_{mod}^G - m_{mod}^{G_p} + E(4405 - 5495) \cdot [k(\lambda^G) - k(\lambda^{G_p})] \quad (5.7)$$

and identifying this difference to an empirical or theoretical colour, final equation has the next expression:

$$c_{emp} = c_{mod} + E(4405 - 5495) \cdot [k(\lambda^G) - k(\lambda^{G_p})] \quad (5.8)$$

Equation 5.8 allows obtaining a reddened colour from an unreddened one of a model star for any value of $E(4405-5495)$. $k(\lambda)$ refers to the extinction law used. We use the J. Maíz Apellániz extinction law (Maíz Apellániz et al., 2014) because we think it is the most appropriate for the study of objects in the Milky Way. Due to GALANTE is an optical photometric survey, we take advantage of that part in Maíz's expression. In this case, we remember that GALANTE project uses 7 filters (4 from JPLUS and 3 new filters developed for our purpose (Lorenzo-Gutiérrez et al., 2019)), which effective wavelengths are in Table 5.3.

Once we have selected the extinction law, we create a $E(4405-5495)$ array from 0.0 to 3.0 with 80 steps on it. With this values of reddening, we create a grid of reddened models, applying the first value of reddening to the complete theoretical library and it generating 6 normalized GALANTE colours from every theoretical star. After this step, it uses the statistical χ^2 to discriminate which model of the theoretical star colours fits better with each empirical

star colours. This star is saved in an array with all its physical parameters and its χ^2 associated value. This process is repeated for each value of the E(B-V) array. Next, we select the best χ^2 value in the array of best fitting for that colour excess. The final step is identify the physical parameters of that theoretical star to the observational star problem, in this case, a NGSL star.

With the aim of making it more robust obtaining each physical parameter, we introduce a gaussian noise of 5% in flux for each normalized GALANTE colour to the models library colours. We estimate this value in colour error to be fair with photometric errors, explaining how we translate an error of 5% in flux to a 0.05 magnitude error. We start with the magnitude equation, using a flux F :

$$m = -2.5 \log_{10}(F) + cte \quad (5.9)$$

To calculate this magnitude error, we derive m :

$$|d(m)| = \left| -2.5 \log_{10}(e) \left(\frac{dF}{F} \right) \right| \simeq \left(\frac{\sqrt{F}}{F} \right) = \left(\frac{1}{\sqrt{F}} \right) \quad (5.10)$$

If we calculate a colour error deriving a colour c from 2 magnitude errors $d(m)$, fixing this error to 5%:

$$d(c) = \sqrt{2} d(m) = 0.05 \quad (5.11)$$

which implies that a flux error of 5% is 0.05 mag, what is the top value that we consider in our proceeding.

Now we introduce all steps of the script in a Monte-Carlo route of 50 simulations. For a fixed E(4405-5495) and for each iteration of Monte-Carlo, we save the best χ^2 , selecting the best one for each E(4405-5495) in the grid of 80 values. Thus, χ^2 discriminates which pertubated and reddened model represents better each observational NGSL star.

Afterwards, we pick out the T_{eff} selected from the models (T_{eff}^1) applying this physical parameter to research again the best fitting, but this time, it has to use the colours of the theoretical library that are between $T_{\text{eff}}^1 \pm 15\% \cdot T_{\text{eff}}^1$. With this criterion, we increase the accuracy finding the best model for the rest of the physical properties. Then, E(4405-5495) array creates a new grid of colours from the models, due to we introduce a higher number of steps between those range of reddening, using now 200 steps between 0.0 and 3.0. We have adopted that rule due to the fact that T_{eff} is the best physical parameter that we can solve using this technique, so the grid of models to work with are highly confined, giving a better obtention of $\log g$, metallicity, and colour excess.

5.2.1 Reduced χ^2 statistic

To do this comparison between models and observations, we choose the statistical χ^2 , which is a very popular model comparison in astronomy. It is a model-based method, thus it depends on the models that we select to compare with, so we have to be very carefull choosing theoretical model libraries in order to cover each physical parameter in the observational region. Furthermore, this statistical parameter is based on gaussian data errors, which fits with our assumption of perturbing models with a gaussian error to create a extense and more realistic grid of models.

This test, introduced by [Pearson \(1900\)](#), grounded the modern statistical analysis fitting model/hypothesis procedure to describe the goodness of our data comparing with models. χ^2 is defined as the minimization between the squared difference between N observed values O with gaussian errors σ_n and their theoretical predictions using models M .

$$\chi^2 = \sum_{n=1}^N \left(\frac{O_n - M_n}{\sigma_n} \right)^2 \quad (5.12)$$

If a theoretical model agrees with an observable then χ^2 will be small, but this is not the only result that we can obtain with this statistical function. On one hand, having a large value of χ^2 means that models are not similar to observed phenomena. On the other hand, a very small χ^2 is unlikely, meaning that errors have been overestimated, deviating measurements from their ideal values (Barlow, 1989; Kenney & Keeping, 1947).

Now, if we have K known degrees of freedom, we can define a reduced χ^2 as:

$$\chi_{red}^2 = \frac{\chi^2}{K} \quad (5.13)$$

Equation 5.13 is a likelihood function that we use in astronomy to do a model comparison, selecting the best model as that one with a χ_{red}^2 closest to one. This is the perfect scenario, which means that the model we are using is the correct one, representing our data properly. Another two scenarios could happen: to obtain a χ_{red}^2 higher than 1 or lower than 1. What means each one? On one hand, if we obtain a χ_{red}^2 , we have a bad fitting, which means that our models don't fit with our observation. This is the most common scenario when we don't obtain a $\chi_{red}^2 \approx 1$. On the other hand, we can have a $\chi_{red}^2 < 1$, meaning that we have an overfit, indicating that experimental errors are smaller than we estimated (Andrae, 2010; Andrae et al., 2010).

In order to facilitate the reading of this work, we adopt χ_{red}^2 as χ^2 .

5.3 Theoretical libraries test

In this section we will use the C and K stellar model catalogues to test MASTER with different scenarios.

5.3.1 Reddening free

The first test that we carry out is to consider one of the theoretical libraries as observational, using the other as a model. First, we consider no reddening, but that there may be different noise values corresponding to 2%, 5%, and 10% relative errors in the fluxes. The next test follows the same structure, introducing different amounts of reddening in the catalogue used as observational. We start by using the K library as observational and C as a catalogue of models to compare with, considering the observations and the models free of reddening, thus obtaining bias and precision in the determination of the physical parameters for different input photometric precisions. We then carry out the same experiment, swapping the role of the libraries. The results are presented in Table 5.4, where we can see how almost identical results are recovered regardless of the catalogue used as the comparison model.

From Figure 5.10 we can see that as we increase the noise, we generate a bias in the determination of the effective temperature, but that never exceeds 100 K (measured as the median of the differences), while decreasing the precision in determining the effective temperature. Although barely perceptible, it seems that the bias is greater when we consider the K models as the theoretical models and C as our observational sample. The same happens for $\log g$, although in this case we see how the precision decreases more quickly with the relative error than for the effective temperature. In $\log g$ there seems to be no difference between one library and the other as the comparison model, as in the case for metallicities. The top panel shows a systematic deviation to hotter temperatures when we increase photometric errors in the models, with none of these errors being an important effect. As we expected, errors increase when we increase observational photometric errors. In the central panel, we observe how the $\log g$ does not show an appreciable bias but instead shows an internal precision that decreases rapidly with the observational error. Finally, in the bottom panel it is also observed how the metallicity does not

Table 5.4 Summary of the results obtained using C and K libraries as observational input data with different photometric errors in flux. Column labelled *Coelho observational* means for C stellar library as input data and K stellar library as comparison model. Respectively, the same for the column labelled as *Kurucz observational*. The analysis has been performed for four different photometric errors, corresponding to 0%, 2%, 5%, and 10% in fluxes.

Photometric error (%)	Parameter	Coelho observational	Kurucz observational
0	diff T_{eff} (K)	1	1
	std T_{eff} (K)	55	55
	diff log(g) (dex)	0.00	0.00
	std log(g) (dex)	0.04	0.04
	diff [Fe/H] (dex)	-0.02	0.02
	std [Fe/H] (dex)	0.17	0.17
2	diff T_{eff} (K)	-7	-1
	std T_{eff} (K)	111	111
	diff log(g) (dex)	0.00	0.00
	std log(g) (dex)	0.05	0.05
	diff [Fe/H] (dex)	-0.01	-0.01
	std [Fe/H] (dex)	0.27	0.27
5	diff T_{eff} (K)	-25	-12
	std T_{eff} (K)	178	184
	diff log(g) (dex)	0.00	0.00
	std log(g) (dex)	0.22	0.20
	diff [Fe/H] (dex)	-0.01	-0.03
	std [Fe/H] (dex)	0.35	0.35
10	diff T_{eff} (K)	-51	-37
	std T_{eff} (K)	243	208
	diff log(g) (dex)	-0.02	-0.02
	std log(g) (dex)	0.33	0.33
	diff [Fe/H] (dex)	-0.02	-0.04
	std [Fe/H] (dex)	0.39	0.39

seem to be affected by a bias when increasing the photometric errors but instead the precision in the determination of this parameter increases with the observational error and is very high (> 0.15) in all the cases we analyse.

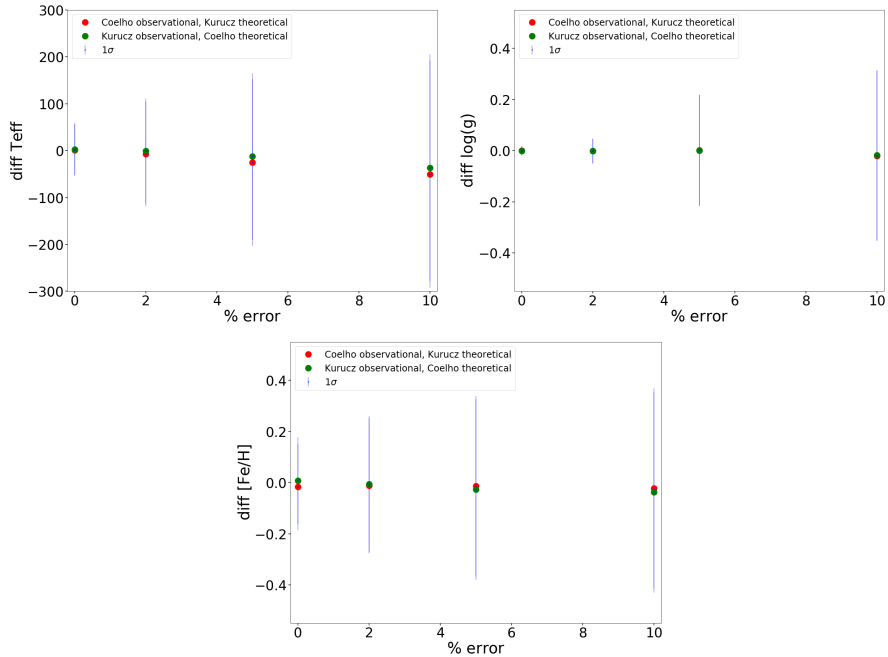


Fig. 5.10 Differences between input and output physical parameters derived by MASTER, for different photometric errors. Red dots are using C library as observational input and K as models to compare with. Green dots refer to the opposite combination (K observational and C as spectral models). Blue lines represent standar deviation as a measurement of the internal precision.

5.3.2 With reddening

This time we perform the same test but considering different degrees of reddening: in particular, for input we utilize reddening values of $E(4405-5495)$ equal to 0, 1, 2, and 3 applied to the library model used as observational data. At the same time, we introduce a grid of extinctions ranging from -1.0 to 4.0

in the models, as explained in Section 5.2. Expanding the reddening range in the set of models avoids edge effect that can appear when the tip values in the models are equal to the tip values of the observational sample. A first realization of this experiment, considering a range of $E(4405-5495)$ between 1.0 and 3.0 on the theoretical side, led to incongruous results that appear to have been overpassed with the new choice of the reddening interval. In this way, we test how our method works by expanding the space of parameters, including extinction. Results of these tests are collected in Table 5.5.

In this case, the main result is that the introduction of this extrinsic variable increases considerably the bias and the internal error in the determination of the stellar physical parameters, mainly affecting temperatures, where the standard deviation can exceed 1000 K for reddening of 1-2-3 magnitudes. Table 5.5 indicates two other important points: a) the collection of reddened stellar models must have reddening that far surpasses the actual reddening of the stars whose parameters we want to determine. This is clearly seen in the table when the standard deviations for cases of reddening of 1-2-3 magnitudes increase considerably with respect to 0.0 reddening.

Figure 5.11 shows a graphic summary of the results. Again, red the dots represent differences using C library as observational data and K as models to compare without gaussian noise. The blue dots show the differences with the libraries' roles swapped. The star markers are those differences applying a noise of 5% for models in MASTER. The blue lines are errors in these differences from models without noise, and the red lines for a 5% noise.

Figure 5.11 shows how the introduction of noise increases the bias in temperature, not reaching more than 200 K, decreasing the accuracy for both catalogues. This bias in the cases in which we introduce the noise is very similar in each test. The same happens in the estimation of surface gravity, where the bias shows the same behavior, but with significant errors in the case in which we apply a noise of 5%. In the determination of the metallicity we do not see a bias, regardless of the library or noise we use, showing in Figure 5.10

Table 5.5 The same as in the tests for Table 5.4. This time we add a new parameter E(4405-5495) in the observational catalogue, applying a grid of reddening in theoretical models of MASTER. The analysis has been performed for four different photometric errors, corresponding to 0%, 2%, 5%, and 10% in fluxes.

E(4405-5495)	Photometric error (%)	Coelho observational				Kurucz observational			
		0	2	5	10	0	2	5	10
0	diff T_{eff}	10	199	-2140	392	9	208	-312	-2180
	std T_{eff}	578	1128	1686	3566	573	1075	1902	3560
	diff $\log g$	-0.02	0.04	-0.06	-0.24	-0.02	0.04	-0.07	-0.26
	std $\log g$	0.31	0.43	0.67	0.89	0.32	0.44	0.68	0.91
	diff [Fe/H]	-0.01	0.02	-0.01	-0.10	0.02	0.01	-0.01	-0.10
	std [Fe/H]	0.31	0.35	0.41	0.44	0.36	0.35	0.41	0.45
	diff E(4405-5495)	0.00	0.02	-0.01	-0.15	0.00	0.02	-0.02	-0.15
	std E(4405-5495)	0.06	0.07	0.08	0.22	0.07	0.07	0.11	0.22
1	diff T_{eff}	59	159	-325	-2203	62	160	-385	-2187
	std T_{eff}	1024	1148	1735	3635	1015	1011	1679	3662
	diff $\log g$	0.05	0.06	-0.07	-0.24	-0.03	0.07	-0.08	-0.27
	std $\log g$	0.51	0.51	0.68	0.89	0.55	0.53	0.68	0.90
	diff [Fe/H]	0.00	0.03	0.00	-0.10	-0.02	0.02	-0.02	-0.10
	std [Fe/H]	0.42	0.39	0.42	0.44	0.42	0.39	0.41	0.44
	diff E(4405-5495)	0.01	0.02	-0.02	-0.15	0.00	0.01	-0.02	-0.16
	std E(4405-5495)	0.07	0.07	0.08	0.22	0.07	0.07	0.11	0.22
2	diff T_{eff}	97	191	-275	-2156	8	218	-335	-2070
	std T_{eff}	908	1070	1511	3520	1135	1111	1798	3563
	diff $\log g$	0.03	0.09	-0.08	-0.25	0.02	0.09	-0.10	-0.24
	std $\log g$	0.54	0.53	0.70	0.89	0.54	0.54	0.70	0.88
	diff [Fe/H]	0.00	0.02	0.00	-0.10	0.00	0.03	-0.01	-0.10
	std [Fe/H]	0.43	0.38	0.41	0.44	0.43	0.38	0.41	0.45
	diff E(4405-5495)	0.01	0.02	-0.02	-0.15	0.00	0.01	-0.02	-0.15
	std E(4405-5495)	0.06	0.07	0.08	0.22	0.06	0.07	0.11	0.22
3	diff T_{eff}	6	281	-349	-2109	30	236	-241	-2185
	std T_{eff}	1114	1139	1872	3598	1126	1096	1573	3687
	diff $\log g$	-0.03	0.09	-0.07	-0.26	-0.01	0.09	-0.07	-0.27
	std $\log g$	0.56	0.44	0.67	0.89	0.56	0.40	0.67	0.91
	diff [Fe/H]	-0.03	0.03	0.01	-0.10	0.00	0.02	0.00	-0.10
	std [Fe/H]	0.48	0.36	0.41	0.44	0.47	0.35	0.40	0.44
	diff E(4405-5495)	0.00	0.02	-0.02	-0.15	0.00	0.01	-0.01	-0.16
	std E(4405-5495)	0.09	0.08	0.11	0.22	0.08	0.07	0.10	0.22

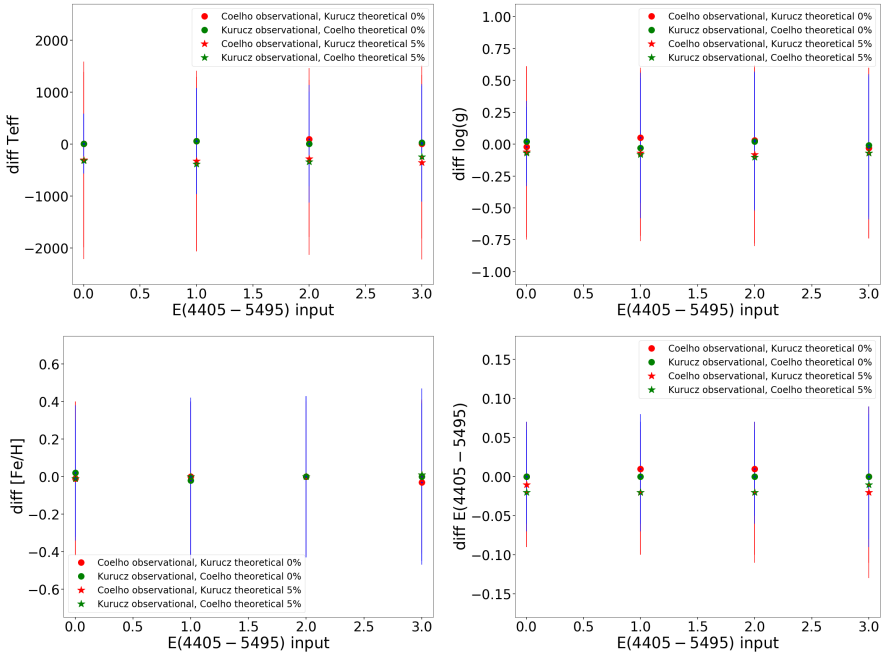


Fig. 5.11 Graphic summary of the results listed in Table 5.5. Colour dots represent models without noise while colour stars show results using a 5% photometric error in flux, introducing different values of reddening in the input catalogue. Blue lines refer to standard deviation in the absence of photometric error while red lines correspond to a 5% photometric error in flux.

how indeterminations in the medians of the differences are close to 0.4 dex. In the case of $E(4405-5495)$, we see how we recover these values without any bias by not introducing noise, while in the tests with noise there is a slight bias, which is not very pronounced. As far as errors in the determination are concerned, we observe that these are greater in the tests with noise.

5.4 Observational tests: NGSL

We carry out a comparative test of the different stellar models, now using the observational data of the NGSL catalogue. In particular, we analyse the theoretical stellar libraries of C, K, T, and Ko combining them in the following way: C+T, C+T+Ko, K+T, K+T+Ko. The T library has been introduced in all cases because it extends the range of effective temperatures catalogued in both C and K. We have also introduced the Ko library to take into account the WDs that could be found in certain regions of the Galactic disk, and how its use combined with the other stellar libraries could even introduce artefacts in the determination of stellar physical parameters. This can be checked using the NGSL library that does not contain any catalogued WD.

The maximum colour excess catalogued in the NGSL library does not exceed 0.80 magnitudes. Here we introduce reddening in the theoretical stellar models that reach up to 3 magnitudes to avoid as far as possible the effect of the edges discussed in Section 5.3. We will assume that the NGSL has a typical error of 0.05 magnitudes for all colours.

As an initial idea when using GALANTE colours, we generated a total of 21 colours, always using one more blue-band less the rest. On the other hand, we thought of using the pivot band F515N filter as a normalization magnitude, using each of the other bands to generate the normalized 6 GALANTE colours that we finally use. However, we did a test introducing in MASTER the 21 colours of both the models and NGSL, doing the same with the 6 normalized colours already described. Figure 5.12 represents χ^2 distribution after both tests, being this our figure of discrimination between both options. As we can see, using 6 colours we get a χ^2 distribution with more centralized values in 1 than using 21 colours. For this example, we use K+T theoretical libraries.

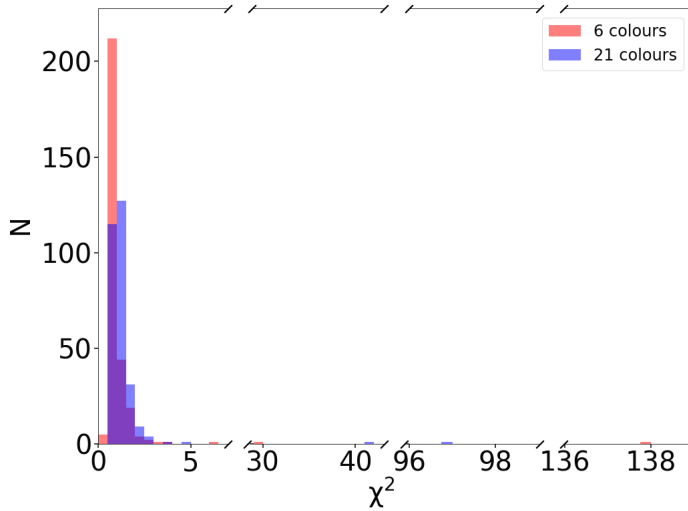


Fig. 5.12 χ^2 histogram comparing results with NGSL using 21 GALANTE non-normalized and 6 normalized colours.

5.4.1 NGSL test with K+T theoretical libraries

We begin by using the K and T theoretical stellar libraries. Figure 5.13 represents the models of K+T in the plane of the physical variables T_{eff} and $\log g$ including also the observational NGSL catalogue. There we observe that there are 5 NGSL stars whose labelled temperatures are not covered by the model grid.

These are the stars: LHS10, HD 123 657, HD 126 327, HD 175 865, and VGKCOM, all of them with $T_{\text{eff}} < 3500$ K. Three of these five are labelled as *binary* or *suspect*, and the other two have an extremely high χ^2 but with a $T_{\text{eff}} = 3500$ K which is the lowest temperature value in the models. For HD 123 657, with a much smaller χ^2 (7.4) we obtain a similar T_{eff} to the one catalogued. The differences lie in the estimation of the $\log g$; in the case of LHS10 it is 5.34 dex in the library, while we obtain 2.5 dex. In the case of

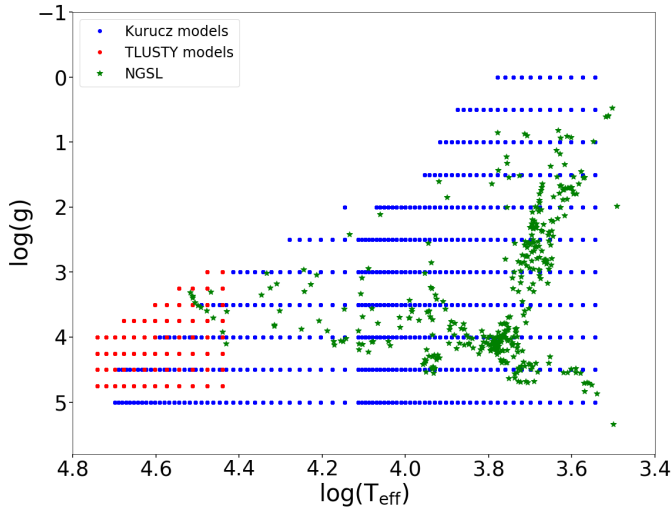


Fig. 5.13 Dots represent K+T theoretical stellar models in the plane of the physical variables T_{eff} and $\log g$. The observational NGSL catalogue is drawn in green stars.

HD 123 657, it is tabulated with a value of 0.59 dex and we obtain it with 0.5 dex.

In Figure 5.14 (a), we represent the results obtained for the effective temperatures, colouring them according to their $\log g$. The green line serves as a 1:1 visual reference between both values. In this case we see a high degree of conformity between the values catalogued and those estimated from these models for the effective temperature, slightly increasing the dispersion for the OB stars. The dots density map seems to fit very well to the 1:1 line and the median of the difference of the fitted stars is of the order of 3% in effective temperature with its standard deviation not exceeding 11%. Another remarkable fact is the deviation towards hot temperatures of 3 stars not considered as *binary* or *suspect* (in ascending order of T_{eff} they are BD 174 708 (*binary* according to Simbad), HD 142 703 (variable star according to Simbad, gamma-Bootis star), and HD 111 786 (variable star according to Simbad of delta Sct type)). Star HD 126 327, with a catalogued temperature of 3100

K and with a surface gravity of 1.98 dex, which is not covered by this grid of models, leads to an adjustment with a χ^2 above the hundred and very erroneous values in all physical parameters except T_{eff} , for which we obtain a value of 3500 K.

The results in Figure 5.14 (b) are not so good for the determination of the superficial gravity where there is a bias defined by the median of the differences, which reaches the value of -0.32 dex and mainly affects the giant and supergiant stars, while the MS stars do not present such a remarkable bias and also show a lower dispersion for the whole metallicity range.

The determination of metallicities in Figure 5.14 (c) shows worse results and is very dependent on temperature. Although the density map shows that the highest concentration of objects fits the 1:1 line, we see how stars with high temperatures (red dots) show chaotic results, tending mainly to determine metallicities much lower than those catalogued. For metallicities catalogued < -1.0 dex, there is a clear bias towards more metallic determinations, even for stars of late spectral type. However, the median of the differences is of the order of -0.04 dex, which shields the biases mentioned above.

Finally, in Figure 5.14 (d), where we represent the obtained reddening values, we see how there is a clear tendency (observable in the density map) to overestimate the colour excess determined, although the median of the differences shows a value close to 0.0.

5.4.2 NGSL test with C+T theoretical libraries

Figure 5.15 shows the range of coverage of these C+T theoretical stellar models with the observational NGSL library. Blue and red dots represent theoretical catalogues while green stars are the NGSL catalogue stars. Here we observe how at least one cold star is outside the coverage, while for OB stars, the grid of models has more remarkable discontinuities than with K+T.

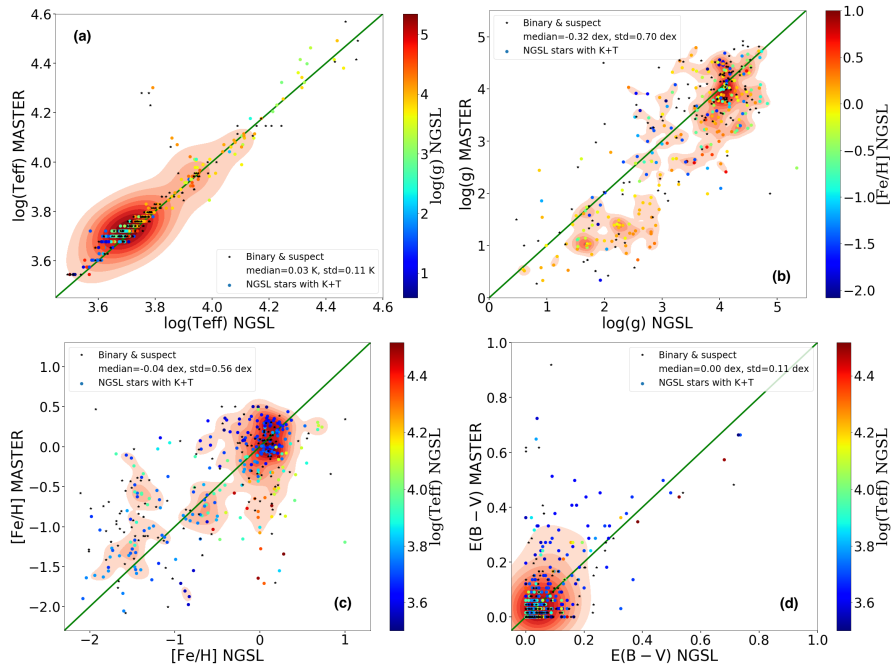


Fig. 5.14 Results of deriving physical variables for NGSL stars based on theoretical libraries K+T.

In Figure 5.16 we plot this grid of models in a $\log g$ -[Fe/H] context. As can be seen, we cannot reproduce the NGSL library in metallicities.

Using C+T we find very similar results to those of K+T, although with small differences for the $\log(T_{\text{eff}})$ and the gravity and colour excess, as we can see in Figure 5.17 (a) and (d). However there is a clear bias in the determination of the metallicities with tabulated values for $[\text{Fe}/\text{H}] < -1.0$ dex, since this grid of models does not cover such low metallicities for temperatures below 25 000 K, as we expect from Figure 5.16. This fact leads us to obtain erroneous metallicities, so these fittings end up being worse than those obtained with K+T.

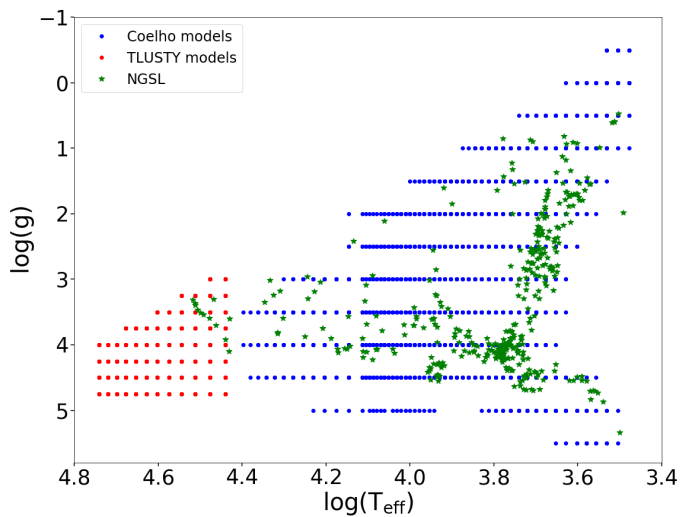


Fig. 5.15 Dots represent C+T theoretical stellar models in the plane of the physical variables T_{eff} and $\log g$. The observational NGSL catalogue is drawn in green stars.

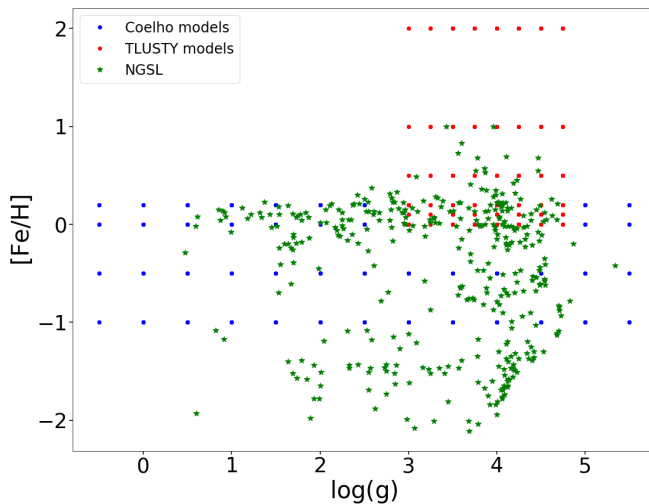


Fig. 5.16 Dots represent C+T theoretical stellar models in the plane of the physical variables $\log g$ and $[\text{Fe}/\text{H}]$. The observational NGSL catalogue is drawn in green stars.

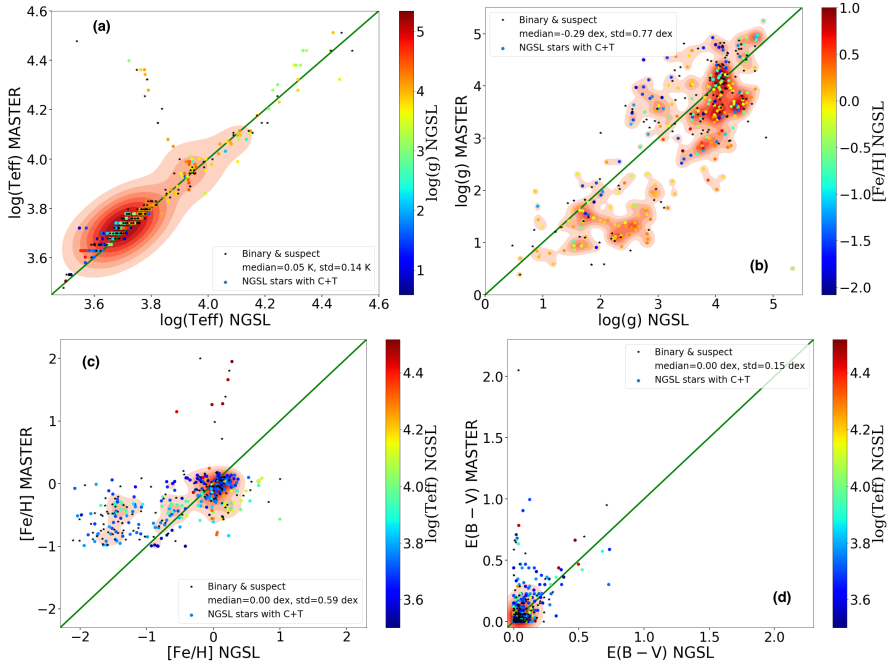


Fig. 5.17 Results of deriving physical variables for NGSL stars based on theoretical libraries C+T.

Next, we show the results that we obtain for $\log g$ in Figure 5.17 (b). Here we again extract results very similar to those of Figure 5.14 (b) for MS stars. However, for giant and supergiant stars with solar metallicity or higher, lower $\log g$ values are obtained systematically. In comparison with what was obtained using K+T, differences are obtained in similar values but with a higher deviation.

We continue with Figure 5.17 (c), which represents the results of $[\text{Fe}/\text{H}]$. In this case, the results that we obtain are concentrated between -1.0 and 0.0 dex for non-OB stars. This happens due to C models' coverage for this type of stars, while for very hot stars, the best fitting occurs from the T models. This fact indicates that the coverage of the C models with $[\alpha/\text{Fe}]=0.0$ for the

metallicity is not complete, so the results are systematically diverted towards incorrect $[\text{Fe}/\text{H}]$ values.

Finally we see the results of colour excess for this study with this pair of models represented in Figure 5.17 (d). Here we again observe the fact of the coupling between temperature and colour excess. A bad determination of one of them entails not correctly deriving the other. In this case, since in Figure 5.17 the number of NGSL stars with a poorly obtained temperature is greater than in Figure 5.14 using other models, here are more objects with a wrong $E(4405-5495)$. We can therefore conclude that, for the same objects of the NGSL library, the theoretical stellar models that work best in deriving their physical properties with MASTER are K+T.

5.4.3 NGSL test adding Ko theoretical libraries

Figure 5.18 shows the GALANTE normalized colours of different models with T_{eff} from 20 000 K to 50 000 K for different surface gravity values. In the case of the MS models, the GALANTE colours are almost indistinguishable from the WD model from $T_{\text{eff}}=30\,000$ K. This indistinguishability between MS and WD models increases as the temperature increases. For this, we must be careful in the choice of models for the estimation of physical parameters, since they could at some point determine more WDs than those that really exist in the population we are observing.

Once we have carried out the study of NGSL with these pairs of theoretical libraries, we wonder whether introducing a third theoretical catalogue would introduce some kind of degeneration when selecting the best model after applying reddening in the GALANTE normalized colours. In order to carry out this study, we select the catalogue of Ko WD models.

Following the same order, in Figure 5.19 (a) we represent the T_{eff} derived with MASTER using the K+T+Ko models. If we compare these results with those from Figure 5.14, we see that the temperatures are very similar except

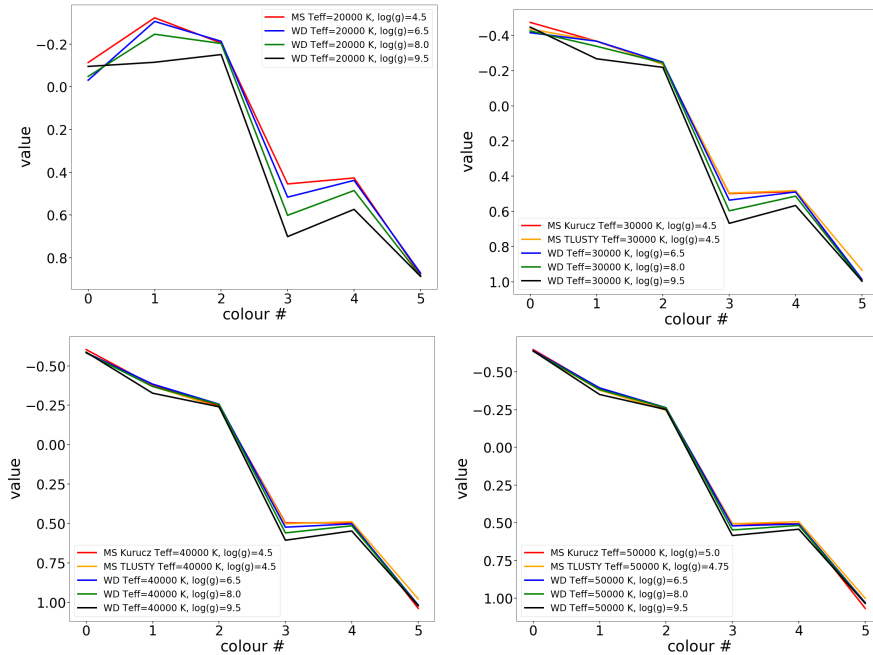


Fig. 5.18 GALANTE normalized colours of different models with T_{eff} from 20 000 K to 50 000 K for different surface gravity values.

for those stars that deviated from the correct ones between 3.8 and 4.0 $\log(T_{\text{eff}})$. On this occasion, the models to which they fit best are somewhat colder. On the other hand, OB stars are derived with values similar to those in Figure 5.14, with a pair of stars with some $\log g$ from supergiants and not from giants. From this comparison we can conclude that those cold stars with difficulties have improved slightly when determining their T_{eff} . It should be noted that this has not happened when introducing WD models since no object shows a $\log g$ of these kind of stars, showing the robustness of the method with the appropriate catalogues.

Figure 5.19 (b) shows the results in $\log g$. When comparing with Figure 5.14 (b) we observe a very similar distribution to that obtained with the

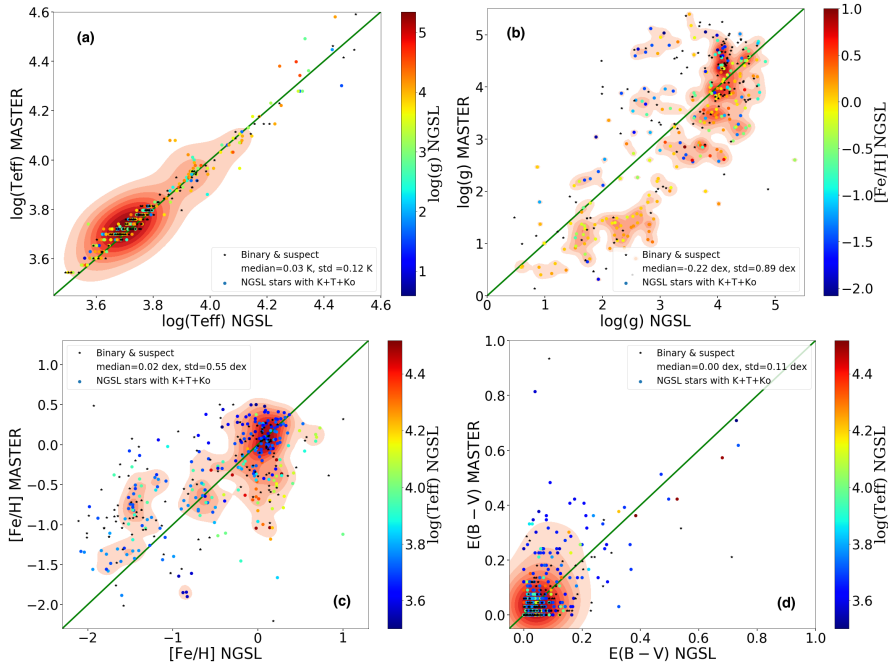


Fig. 5.19 Results of deriving physical variables for NGSL stars based on theoretical libraries K+T+Ko.

K+T models. As expected, here we can see that the derived values of $\log g$ come only from the models of K+T, without using those from WD models.

In terms of metallicities, Figure 5.19 (c) presents the results we obtain using the 3 catalogues in MASTER. Although the results in the distribution of densities are very similar, the values that are not correctly recovered are distributed further away from those tabulated by the authors, which explains the deviation we derive in this case.

Finally, since the T_{eff} have not been derived from the Ko models, we do not expect any change in the values of $E(4405-5495)$. Figure 5.19 (d) represents the colour excess values for this set of 3 models. In this parameter, the values

that we obtain are exactly those expected when launching MASTER using only the K+T models, confirming the certainty of our results.

We will now present the MASTER results for the NGSL stars, inputting models of C+T into MASTER with the addition of the Ko WD models. In this case, due to the fact that T_{eff} with C+T were not derived as well as with K+T, the inclusion of the Ko models can cause some of these results to improve their fitting from the WD models. Figure 5.20 presents all the results for each physical parameter using these models in MASTER.

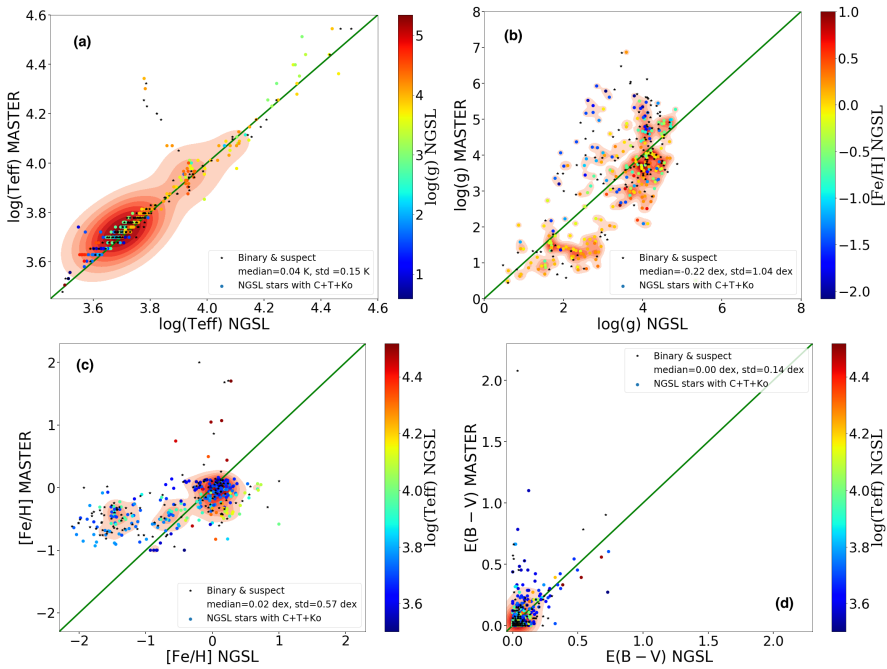


Fig. 5.20 Results of deriving physical variables for NGSL stars based on theoretical libraries C+T+Ko.

In this case we see an improvement, without being entirely correct, in the T_{eff} for cold stars, which as we can see in the results of the $\log g$ in the plot (b), come from a better fit using WD models. It should be remembered

that among the NGSL stars there is not any catalogued star of this type, so it is attaining a better mathematical solution of χ^2 , but without being a better physical solution.

Regarding metallicity, this physical variable is still not recovered correctly since C models do not cover this parameter for the range of values that the NGSL library has. Again, erroneous values are derived for those stars that best adjust using K when forced to obtain a better χ^2 mathematical result.

Finally, we observe a somewhat higher value in those stars that have better fitting to some WD models, although as we see in Figure 5.20 (d), this only happens for those stars for which this theoretical catalogue was used to get a better solution in their fitting. This fact reflects the correlation between the estimation of the effective temperature of a star and its reddening. Therefore, if the best fitting is obtained from a WD model, its colours are reddened with a higher E(4405-5495) value to get its modified GALANTE colours for the model until it matches the GALANTE colours for NGSL.

Table 5.6 summarizes the results we obtain for each block of models using the NGSL as an observational catalogue. We also introduce the percentages of the NGSL stars that we obtain with χ^2 below 5% and 2%. In view of these results, we can conclude that the set of catalogues of K+T obtains more accurate results in reference to those catalogued for these stars of the NGSL library.

As a complementary table (Table 5.7), we include the results of the derivation of the physical stellar parameters of the NGSL stars from the K+T models. At this point, we take stars BD 442 051 and HD 126 327 to clarify our results in 2 extreme scenarios watching Figure 5.21 and Figure 5.22 respectively.

Table 5.6 This table summarizes the results we obtain for each block of models using the NGSL as input catalogue. The term diff E(B-V) means for the difference between the E(B-V) listed in [Koleva & Vazdekis \(2012\)](#) and the E(4405-5495) estimated by MASTER. This difference has an intrinsic component depending on actual temperature and reddening ([Maíz Apellániz, 2013a](#)).

	K + T	K + T + Ko	C + T	C + T + Ko
diff $\log(T_{\text{eff}})$	0.03	0.03	0.05	0.04
std diff $\log(T_{\text{eff}})$	0.11	0.12	0.14	0.15
diff $\log g$	-0.32	-0.22	-0.29	-0.22
std diff $\log g$	0.70	0.89	0.77	1.04
diff [Fe/H]	-0.04	0.02	0.00	0.02
std diff [Fe/H]	0.56	0.55	0.59	0.57
diff E(B-V)	0.00	0.00	0.00	0.00
std diff E(B-V)	0.11	0.11	0.15	0.14
χ^2 (%) < 5	93	93	92	92
χ^2 (%) < 2	80	80	77	77

Table 5.7 Comparison of example stars covering the range of each stellar physical parameters of the NGSL empirical library. We tabulate nine NGSL stars by way of example.

NGSL star	Input $T_{\text{eff}}(\text{K})$	Output $T_{\text{eff}}(\text{K})$	Input $\log g$	Output $\log g$	Input $[\text{Fe}/\text{H}]$	Output $[\text{Fe}/\text{H}]$	Input $E(\text{B}-\text{V})$	Output $E(4405-5495)$	χ^2
HD 126 327	3100	3500	1.98	4.50	-0.45	0.50	0.09	0.87	137.80
BD 442 051	3664	3750	4.70	4.50	-0.83	-1.82	0.06	0.05	1.03
BD 511 696	5746	6000	4.39	4.50	-1.25	-1.21	0.03	0.04	0.97
HD 111 786	7549	10000	4.17	3.50	-1.06	-0.39	0.03	0.15	0.94
HD 143 459	10 298	9250	3.85	3.00	-0.47	-0.90	0.13	0.08	0.86
HD 212 593	13 642	14000	2.42	3.00	0.30	-0.27	0.16	0.20	0.69
HD 175 156	16 361	17000	3.04	3.00	0.17	-0.37	0.33	0.37	1.10
HD 096 446	20 086	24000	3.59	4.00	0.06	-0.74	0.07	0.10	0.87
HD 057 061	32 514	27000	3.37	4.00	0.18	-2.42	0.20	0.16	1.94

We represent the best model found with our method applied to both NGSL stars using the full 6 GALANTE colours. In red line is the best theoretical star model found, in blue it shows the observational colours.

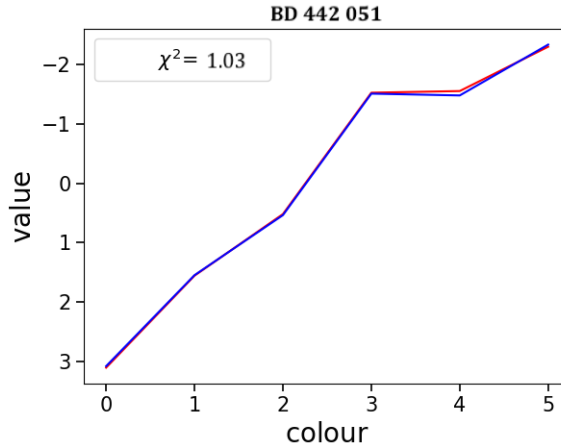


Fig. 5.21 Diagram of the best fitting model for BD 442 051. We show the best fits for this star in red versus the NGSL GALANTE colours.

We takes BD 442 051 as an example, focusing on the full 6 colours plot in Figure 5.21. We observe that differences between the best model and observational are very small, giving as a result a $\chi^2=1.03$. We can see in Table 5.7 physical stellar parameters recovered. T_{eff} is properly returned as we expect attending to the plot. $\log g$ and $E(4405-5495)$ are also very coincident with those tabulated in NGSL, but $[\text{Fe}/\text{H}]$ is clearly different in this comparison, even though this is completely close-fitting. We translate this fact as a discrepancy between atmospherical models and NGSL spectral fitting.

We can also see the other example star, HD 126 327, in Figure 5.22. This example is very representative, allowing us to see what is happening when we try to recover physical parameters of a star which is not covered by Kurucz theoretical models. Because of we cannot find a better model for this case, the result is that we do not recover the same parameters tabulated by NGSL.

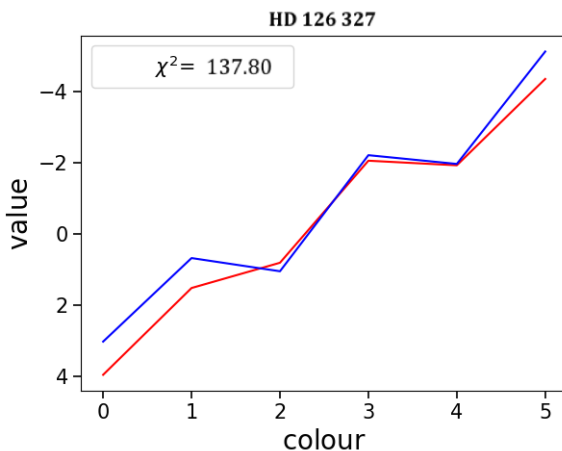


Fig. 5.22 Diagram of the best fitting model for HD 126 327. We show the best fits for this star in red versus the NGSL GALANTE colours.

HD 126 327 represents a good example of the limits of the models, requiring a colder model spectrum in that range to obtain accurate parameters of this star. As we observe with this example, MASTER reddens as much as necessary to distort the models in their search for the best fitting. In case there is not any model that covers the physical parameters of the stars to be adjusted, what MASTER obtains are very high reddening parameters compared to the real one, thus giving the rest of the properties in an erroneous way. This is reflected in a χ^2 value that is far away from the desired one, serving as a discrimination criterion.

5.4.4 Results with NGSL without noise

In this subsection we will repeat the above procedure using the NGSL catalogue again and the same way to group the models, without applying noise. With this test we want to obtain results that can give us an idea of the internal errors made with this methodology for each set of theoretical libraries. Below we represent, for the 4 set of previous models, the values of the physical

parameters retrieved with MASTER for the NGSL. Figure 5.23 shows the results obtained from the effective temperature, both for the K+T and C+T model sets, and for their extensions with the Ko models. As we can see, there are no noticeable differences in plot results with K+T and K+T+Ko ((a) and (c)), without significant variations in the derivation of the T_{eff} for any range of spectral type. Taking into account the results with C+T compared to those obtained and adding the Ko models ((b) and (d)), we see how some of the mathematical solutions obtained with these 3 models are better than with the 2 models catalogue. If we compare the results by model blocks, we appreciate that the results involving those obtained with Kurucz have a lower deviation than those obtained from Coelho's models for cold stars, obtaining similar results for OB stars.

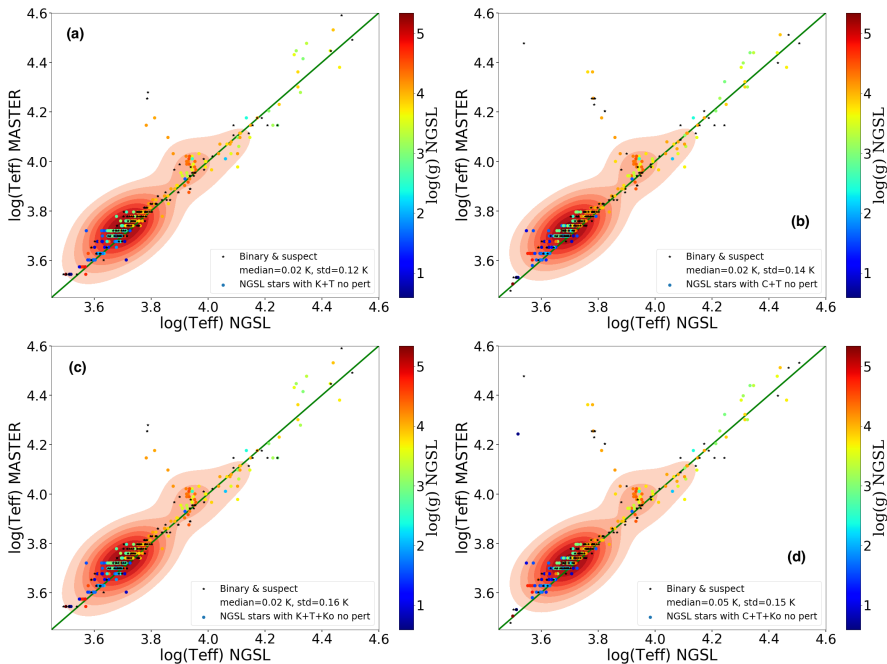


Fig. 5.23 Results of deriving effective temperature for NGSL stars based on theoretical libraries C+T+Ko without noise.

Figure 5.24 shows the recovered results for the $\log g$ physical parameter. In the same way, the results obtained with K+T and expanding with those of Ko models, we do not appreciate changes for this variable. In contrast, for results using C+T compared to these by adding WD stellar models, different results are retrieved. This fact once again shows that the inclusion of Ko models recovers mathematically improved results that are not physically acceptable. A remarkable fact regarding these results is that, for any set of models used for NGSL, our results are systematically lower than those tabulated by [Koleva & Vazdekis \(2012\)](#). These values are around 0.20 dex below, being this value the step between models for this physical parameter.

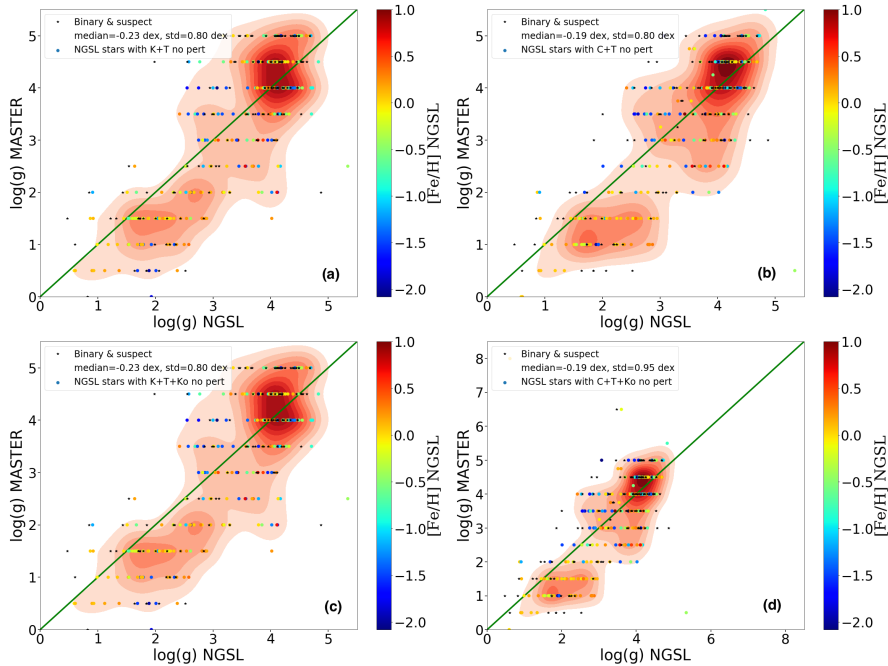


Fig. 5.24 Results of deriving $\log g$ for NGSL stars based on theoretical libraries C+T+Ko without noise.

Figure 5.25 shows the derivation of metallicity for each group of models. As the results used by the Coelho models show, most of them are between -1.3 and 0.2, whereas for OB stars they have values of $[\text{Fe}/\text{H}]=2$, that are derived from the TLUSTY models. In contrast, the results using the Kurucz's models have a wider coverage of this physical variable, so the results obtained, even with a systematic deviation towards less metallicity values of those tabulated by the authors, are almost identical for both sets of models.

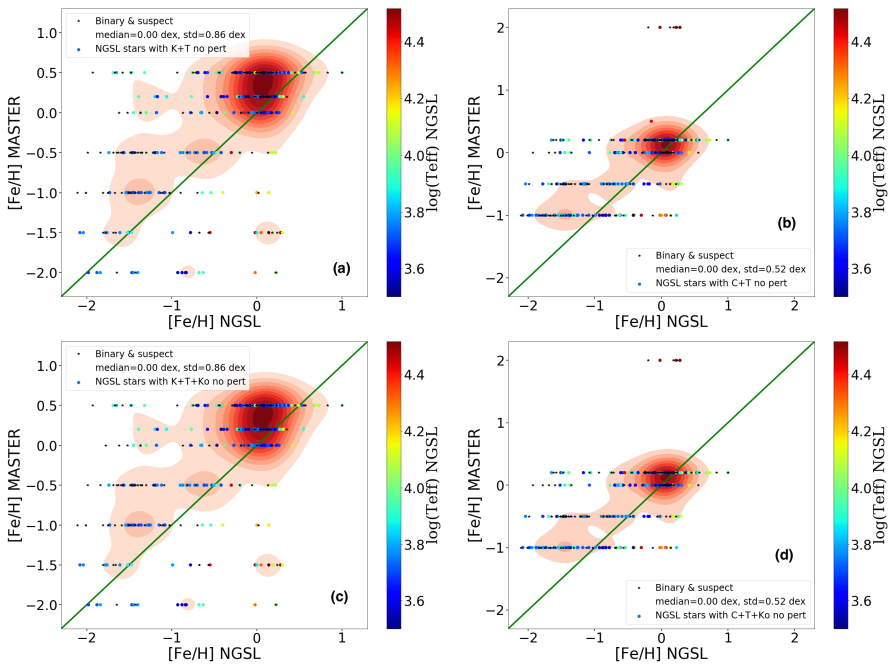


Fig. 5.25 Results of deriving $[\text{Fe}/\text{H}]$ for NGSL stars based on theoretical libraries C+T+Ko without noise.

To conclude, Figure 5.26 shows the colour excess recovered by MASTER in each model test. If we look at the results obtained from the Coelho models, we see how those stars with a bad derivation in their temperatures, we obtain a more discordant of $E(4405-5495)$ than in the results obtained with the Kurucz

models. This fact shows the correlation between T_{eff} and $E(4405-5495)$, with the correct derivation of one being very important for obtaining the other and vice versa. In the case of the C+T libraries, by not finding the T_{eff} for the cold stars cited in Figure 5.23, by adding the Ko models, the mathematical solution ends up getting better by finding a highly reddened WD model that fits better than a Coelho model. Regarding the results obtained using the model sets with Kurucz, the same values are obtained for both sets of catalogues, so it is confirmed that it is not necessary to use the WD models to cover the NGSL, as we expected since there is not a single star of this type in this library.

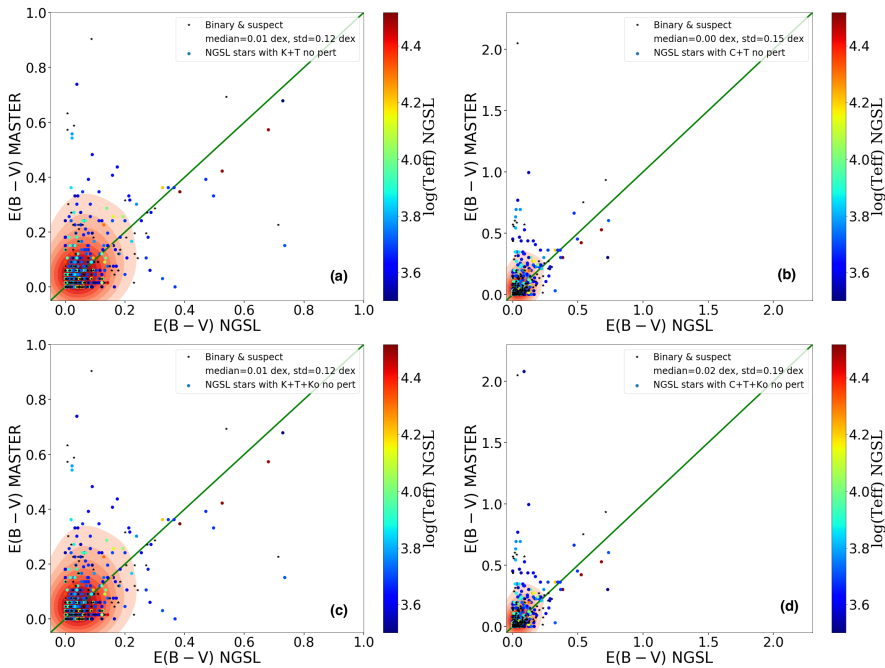


Fig. 5.26 Results of deriving reddening for NGSL stars based on theoretical libraries C+T+Ko without noise.

Table 5.8 summarizes the results we obtain for each block of models using the NGSL as an observational catalogue without introducing any noise in the

Table 5.8 This table summarizes the results we obtain for each block of models (without noise) using the NGSL as input catalogue. The term diff E(B-V) means for the difference between the E(B-V) listed in [Koleva & Vazdekis \(2012\)](#) and the E(4405-5495) estimated by MASTER. This difference has an intrinsic component depending on actual temperature and reddening ([Maíz Apellániz, 2013a](#)).

	K + T	K + T + Ko	C + T	C + T + Ko
diff $\log(T_{eff})$	0.02	0.02	0.02	0.05
std diff $\log(T_{eff})$	0.12	0.16	0.14	0.15
diff $\log g$	-0.23	-0.23	-0.19	-0.19
std diff $\log g$	0.80	0.80	0.80	0.95
diff [Fe/H]	0.00	0.00	0.00	0.00
std diff [Fe/H]	0.86	0.86	0.52	0.52
diff E(B-V)	0.01	0.01	0.00	0.02
std diff E(B-V)	0.12	0.12	0.15	0.19
χ^2 (%) < 5	99	93	92	92
χ^2 (%) < 2	96	80	77	77

models. We also introduce the percentages of the NGSL stars that we obtain with χ^2 below 5% and 2%. In view of these results, we conclude again that the set of catalogues of K+T obtains more accurate results in reference to those catalogued for these stars of the NGSL library.

5.5 Summary and conclusions

In this chapter we analyse the differences between several theoretical stellar libraries, with the result that for $T_{eff} < 10\,000$ K there are discrepancies between them, highlighting a dependence on the catalogue used. We also analysed with MASTER a fitting of models to observational SEDs developed by us and based on χ^2 , studying the behaviour of the different models and how to work better with them to obtain a lower bias and the inclusion of artefacts. To do

this, we use the GALANTE normalized colours and perform different tests between the models, both for the case of extinction and without it. Here we see how the inclusion of this extrinsic parameter has great weight, showing an increase both in the medians of the differences and standard deviations in comparison with the same study carried out without applying extinctions. Once this analysis with models was done, we used the NGSL observational catalogue, using 3 libraries of models with extinction. After analysing the results, we expanded our grid of models with a WD catalogue, checking whether our method is sufficiently robust when introducing spectral models that are not catalogued in the NGSL. For the specific case of C+T, we see that the introduction of this library causes a couple of stars to adjust better with WD SEDs. The bad fitting χ^2 obtained from this group of models improves with the inclusion of the Ko models, due to the impossibility of covering all the physical parameters of the NGSL with the C+T models.

“Once again...welcome to my house. Come freely. Go safely; and leave something of the happiness you bring.”

Dracula

6

GALANTE photometry of Cygnus OB2: observation, reduction and calibration

Contents

6.1	Why Cyg OB2?	122
6.2	Observations	125
	6.2.1 Image reduction and photometry	125
6.3	GALANTE calibration of instrumental photometry .	132

6.1 Why Cyg OB2?

We now have a complete, tested methodology to run in an observational GALANTE region. We selected the Cygnus OB2 region to study, due to its having a huge collection of stars, including hot OB stars, with a wide range of interstellar absorption going from 4 to 20 mag in the visible (Massey & Thompson, 1991; Wright et al., 2015).



Fig. 6.1 Urania’s Mirror card (1825), showing Lacerta, Cygnus, Lyra and Vulpecula constelations and Anser star (α -vulp) illustration card (Commons, 2018).

The observational part of this thesis is based on the study of the Cygnus OB2 association because we consider it to be a perfect laboratory, for studying the star-formation processes of masive stars, because its large population of OB

stars, only comparable to the Carina region. We can define an OB association as a system whose stars are gravitationally unbound, consisting typically of between 10 - 100 massive O and B stars type (Blaauw, 1964; Gratton, 1963), containing several hundred or thousands of stars of intermediate and low mass. These associations are formed within a giant molecular cloud. The age these associations usually have is around 10 Myr with an average size of about 80 pc (Elmegreen, 2009). It is now believed that most of the stars that make up the Milky Way disk were formed within OB associations. de Zeeuw et al. (1999) conducted a study of the stellar content of OB associations with a radio of 1 kpc from the Sun, making use of the Hipparcos data. Associations are representative of a size and age (10 Myr) within a Hierarchical Star Formation process (Elmegreen & Efremov, 1998), where large clouds of gas in galaxies, with typical kpc sizes and masses of a million solar masses, forming stars in a structure assembled where stellar clusters are formed within other higher-order clusters with a self-similar geometry (Sánchez et al., 2010). These associations are often accompanied by stars still in formation (Comerón et al., 2008) and presenting a complicated cinematic (Jeffries et al., 2009; Román-Zúñiga et al., 2019; Wright et al., 2019). Inside these associations some stellar groupings have been recognised as young stellar clusters (Comerón & Torra, 2001; Le Duigou & Knödlseeder, 2002).

Cyg OB2 is one of these associations that has some unique features containing a large number of O stars, along with the Carina nebula, and it also seems to be located in a tangent direction to a spiral arm. Furthermore, when we look at Cygnus we see the local spiral arm tangentially, overlapping the structures at different distances in the line of vision, giving a wrong perception of the actual spatial structure and the content of these associations. Cyg OB2 ($l=79.8^\circ$ and $b=0.8^\circ$) is included within a wider star formation region, forming part of Cygnus-X region, containing several 10^4 solar masses (Comerón et al., 2002; Knödlseeder, 2000). It is located at about 1.7 kpc according to Berlanas et al. (2019) using Gaia DR2 data. A previous work of Berlanas et al. (2018)

obtain a 1.4 kpc distance using spectroscopy from OB stars. This distance is the same for [Comerón & Pasquali \(2012\)](#) using a careful methodology with spectroscopic observations. Other work from [Kiminki et al. \(2015\)](#) establish a distance for 1.33 kpc using in their study eclipsing binaries, while [Zhang et al. \(2012\)](#) obtain an upper distance limit of 1.61 kpc using radiointerferometry in the region of Cyg OB2, discrepancies are attached to other studies relating to its extent, and is not currently clearly delimited ([Berlanas et al., 2019](#); [Kiminki et al., 2007](#); [Wright et al., 2015](#)). We can see an example of this in the study by [Straižys et al. \(2014\)](#), where the authors analysed the stellar population of the M29 cluster in which they have stars ranging from a few hundred pc to more than 2 kpc away. They also showed that three-dimensional geometry of the regions that make up Cygnus very complicated, where it can be difficult to separate different subsystems into projection, being necessary to introduce other physical variables such as kinematics and/or metallicity to unravel this structure.

As far as his age is concerned, it seems to be a young association with ages not exceeding 10 Myr ([Elmegreen, 2009](#); [Kuhn et al., 2019](#); [Leisawitz et al., 1989](#); [Wright et al., 2014](#)). Another studies carried out with clusters within Cyg OB2 in both visible ([Comerón & Pasquali, 2007](#)) and infrared ([Le Duigou & Knödlseeder, 2002](#)) date to this region with that upper age limit, thus confirming that we find an area of ongoing star formation, reaching to find stars as young as 1 Myr. There have already been enough authors who have studied this region as complex as interesting with both spectroscopy and photometry for different wavelength ranges ([Comerón et al., 2002](#); [Drew et al., 2008](#); [Hanson, 2003](#); [Kiminki et al., 2015](#); [Knödlseeder, 2000](#); [Reddish et al., 1966](#); [Wright et al., 2015](#)). It is clear that Cyg OB2 is a region of stellar formation that, because of its previous studies and its connection to the Local Arm, engage it into a observational target of great interest to analyze in greater detail the star population of the region and its spatial structure. The

data from Gaia DR2 is the ideal complement to this objective, as we will see throughout this work.

The Cygnus region is very complex for any range of wavelengths, given its high frequency spacial variation in interstellar absorption. These qualities make Cygnus an ideal region for studying his stellar formation history, its structure and evolution, as well as the distribution of extinction in the area, or the dynamics and kinematics of OB associations and stellar groups.

6.2 Observations

6.2.1 Image reduction and photometry

The OAJ provides astronomers with images taken with the T-80 telescope. Before this, they perform a pre-processing of Raw images, whose pipeline mainly performs 2 tasks: generation of the calibration frames and daily processing. First, you get the Master Calibration Frames that will be used to correct the cosmetic of scientific images and get the first zero-point calibration. This process uses the images of:

- Bias frames: Used to correct any reset additive pattern.
- Flat-field: Used to correct the pixel to pixel variations and instrumental throughput.
- Fringing pattern: Used to remove the additive interference patterns.
- Photo-superflat: Used to correct the residual multiplicative factor not totally covered by the flat-fields. These can be produced by a non-homogeneous illumination on the master flat, astrometric distortion sampled by the pixels, and ghosts in the master flat.
- Spect std: science image containing a spectrophotometric standard star for internal checking purposes.

All images involved in this process are shown in Figure 6.2. In this caption, the central blue figure is an example of a raw science image in F515N for a 50 s exposure of Cygnus OB2. The grey images are Bias, Flat+Sky, Spectral std, and Master Frame, respectively, which are applied to the raw image, obtaining a final science image to work with.

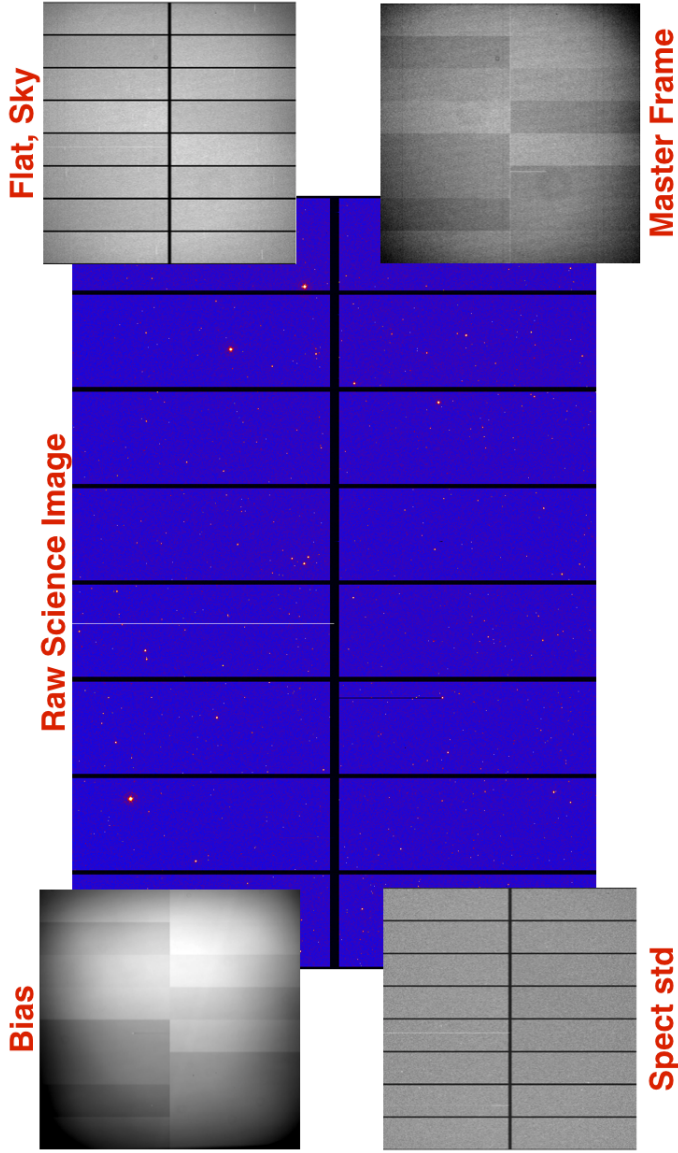


Fig. 6.2 In this caption, the central blue figure is an example of a raw science image in F515N for a 50 s exposure of Cygnus OB2. Grey images are Bias, Flat+Sky, Spectral std, and Master Frame, respectively, which are applied to the raw image, obtaining a final science image to work with.

The next process, daily processing, is to remove the cosmic rays, bad pixels and possible satellite traces with different masks to subsequently apply the Master Frames previously generated. Finally, an astrometric calibration is performed whose coefficients are saved in the header, and these are the working images with which we will finally get the GALANTE photometry.

In order to clearly understand the way to proceed in explaining this section, we must keep in mind the goal of GALANTE. This project seeks to perform a mapping for the entire range of temperatures as its first objective. This is the reason why GALANTE has such varied observation times, making sure that both very bright stars and the weakest ones are obtained without saturation and with the expected signal-to-noise ratio. In this way we could create a list of objects observed in the common filters with SDSS, thinking of F348M like a *uSDSS* filter, and look for those objects in the rest of the GALANTE filters to obtain a complete 11-band photometry.

Once we obtain the pre-processed scientific images by CEFCA, we obtain the catalogues of the fields observed with the extraction of the flux using aperture photometry. To do this, we designed an algorithm in Python that uses several packages from Image Reduction and Analysis Facility (IRAF; Tody (1986)): *photutils*, *astropy* and *DAOSStarFinder*. Before applying aperture photometry, we have determined the fundamental parameters of this task (background, threshold, FWHM and radius aperture) using a 1000x1000 pixel subimage in all obtained images (different fields and exposure times). To get the background level we apply *photutils*, calculating the median value of the image with the associated sigma. We set a value equal to 3 times the sigma of the sky background (σ_s), removing pixels that are above or below this value, we made 5 iterations for a better estimate of the sky background. To locate the objects in the images, we use *DAOfind* with a minimum values of $\text{threshold}=5\sigma_s$ and $\text{FWHM}=2$, using a radii array to extract the fluxes. Figure 6.3 represent an example of the objects detection with the *rSDSS* filter for 10 s of exposure. Each object found is highlighted in red, with an

arbitrary radius that is equal for all, the centre of which is that detected by the DAOSStarFinder function.

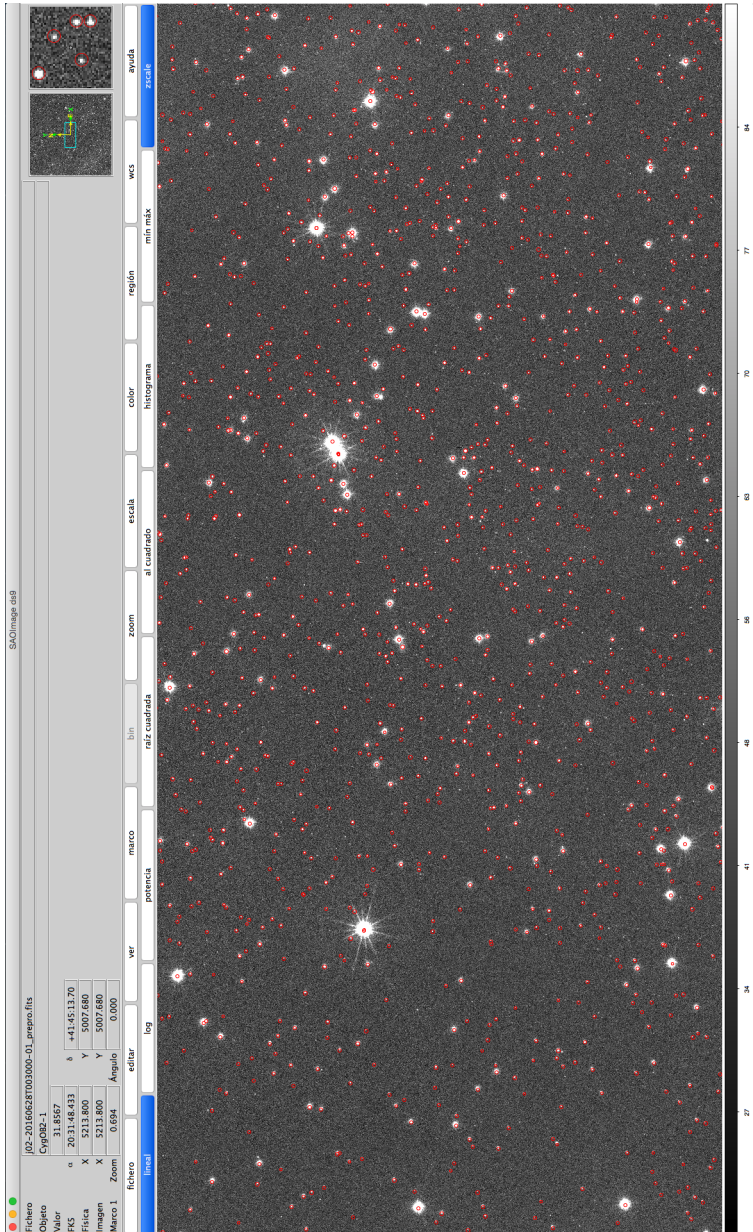


Fig. 6.3 Example of a field observed with the *rSDSS* filter for 10 s of exposure. Each object found is highlighted in red, with an arbitrary radius that is equal for all, the centre of which is that detected by the DAOSStarFinder function.

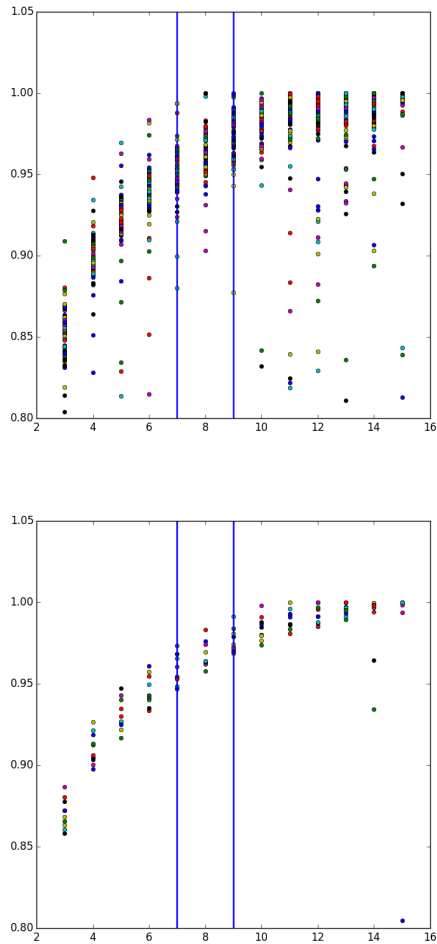


Fig. 6.4 Example for the *rSDSS* filter in the case of 100s (upper) and 1s (bottom). The normalized flux is represented on the Y axis, taking the maximum value of each flux for the different radii represented on the X axis.

Figure 6.4 shows two diagrams example with the maximum flux for each normalized object is generated for each radius for the *rSDSS* filter in the case of 100s (upper) and 1s (bottom). As we see, for 100s of exposure it is enough

to take an aperture radius of 7 pixels to take a flux of more than 95% for most objects, while for an exposition of 1s, we need to use an aperture with a radius of 9 pixels. After reviewing these results with the rest of the bands and exposure times, we adopt the criterion of using an aperture of 9 pixels, using an external ring of 2 pixels wide to subtract the background, for all filters and exposure times.

We obtain the error in this flux calculation as the square root of the quadratic sum of the Poisson noise of each individual source and the background error, given by the equation:

$$\Delta F = \sqrt{\sum_{i \in A} \sigma_{tot,i}^2} \quad (6.1)$$

where ΔF is the quadrature sum of the total errors over the non-masked pixels within the source area, A . $\sigma_{tot,i}^2$ is the input error array given by the Poisson noise added quadratically with the sky background error for each pixel.

Finally we apply this procedure to all images with their corresponding filters and exposure times

6.3 GALANTE calibration of instrumental photometry

Once this reduction is detailed, it is important to trace a path to reduce all the images. To do that efficiently, firstly we obtain each single star from *SDSS* filters images g , r , i , and z , with F348M included as a *uSDSS*-like filter. These stars are in an array, awaiting the reduction of the rest of the images in F420N, F450N, F515N, F660N, F665N, and F861M. So the pipeline searches these positions in those bands in each image to obtain a photometry, completing the instrumental catalogue in this way.

This procedure give us a total amount of 6765 non-saturated stars in each of the 11 bands. Once we identify objects obtaining their instrumental photometry, we use a simple methodology to calibrate them taking advantage of the *SDSS* DR12 and *RefCat2* catalogues.

Equation 6.2 summarizes the transformations from *SDSS* to GALANTE photometry developed using synthetic photometry from the NGSL and MAW libraries for each GALANTE filter. Applying those transformation equations described in Chapter 4 (Lorenzo-Gutiérrez et al., 2019), we obtained preliminary zero points (ZPs) to calibrate Cyg OB2 for a small sample of this region. To achieve this goal, all instrumental AB magnitudes in each frame have been tied to the instrumental magnitude of the longest exposure time. At this point, we could calibrate F348M, *g*, *r*, *i*, and *z* directly from *RefCat2* and *SDSS* DR12 and apply GALANTE transformation equations for the rest of the filters.

$$\begin{aligned}
 F348M - u &= 0.149; \text{ rms} = 0.067 \\
 F420N - g &= 0.317(u-r) - 0.182; \text{ rms} = 0.068 \\
 F450N - g &= 0.125(g-i); \text{ rms} = 0.027 \\
 F515N - g &= -0.300(g-r) - 0.032; \text{ rms} = 0.028 \\
 F660N - r &= -0.134(g-z) + 0.040; \text{ rms} = 0.019 \\
 F665N - r &= -0.138(g-i) + 0.010; \text{ rms} = 0.009 \\
 F861M - z &= 0.047(r-z) + 0.005; \text{ rms} = 0.008
 \end{aligned} \tag{6.2}$$

In this study, we obtain a robust calibration for GALANTE ZPs using a different methodology. Once we have all frames tied to their longest instrumental time, we obtain 4 different fields with overlapping. In order to calibrate these instrumental AB magnitudes properly, we calculate the instrumental ZP between each field using common stars in frames. This procedure gives us a

Table 6.1 Zero Points calibration directly using *griz* from *RefCat2* and *u* band from *SDSS* DR12 for common filters with *SDSS* and GALANTE transformation equations for the rest of the bands.

Filter	Zero Point	std Mean Error
F348M	26.046	0.004
gSDSS	28.463	0.003
rSDSS	28.535	0.002
iSDSS	28.217	0.002
zSDSS	27.621	0.003
F420N	24.289	0.005
F450N	24.431	0.005
F515N	26.359	0.004
F660N	25.969	0.004
F665N	24.074	0.006
F861M	26.517	0.003

reliable ZP obtention, free from errors in the photometry subtraction. Using this method of calibration, we obtain the ZPs for the 11 bands in Cyg OB2 which are tabulated in Table 6.1. These values are derived using *RefCat2* for *griz* bands and *SDSS* DR12 *u* band. We calculate the std Mean Error as the square root of the quadratic sum of errors derived from transformation equations (rms) plus errors obtained from aperture photometry, divided by the number of objects. We want to note that, although the value of these errors are small, we should not forget that they are dominated by errors coming from transformation equations, which become up to 7 tenths of magnitude in the bluer GALANTE bands.

Taking previous studies in Cyg OB2 based on photometry, we highlight [Guarcello et al. \(2012\)](#), where they observed and calibrated 3 *SDSS* bands: *rSDSS*, *iSDSS*, and *zSDSS*. We can approach this to compare our calibration

in common bands selecting those stars in their catalogue with good PSF and with circular profiles, which entails taking only those with $\chi^2 > 5$ or $|sharp| > 8$. It is important to remember that [Guarcello et al. \(2012\)](#) apply ZPs from their calibrated colour equations. This comparison aims to show possible differences between their calibration and this GALANTE one using *RefCat2*. We compare our GALANTE colours $r-i$ and $i-z$ with Guarcello for those common stars. Figure 6.5 shows in red dots the differences between GALANTE and *RefCat2* and in blue dots those differences with [Guarcello et al. \(2012\)](#). A visual reference line is plotted in green with a 0.0 value.

Differences in colour $r-i$ in both GALANTE calibrations indicate a linear ZP for each of those bands in comparison with Guarcello's colour calibration. In this case, our GALANTE calibration obtains ZPs more accurately. In contrast, $i-z$ colour shows a high colour term if we observe its linear calibration in red dots. We can see in the blue dots how our calibration using *RefCat2* solves this problem. Figure 6.6 presents the differences for common objects between our observations with the T-80 telescope and in both Guarcello's, the *SDSS DR12* and the *RefCat2* catalogues. Applying a simple difference in each band, we extract ZP without colour terms, in contrast to [Guarcello et al. \(2012\)](#). In view of these results, we conclude that this obtaining of ZPs is more precise than that made using *SDSS DR8* as could be seen in Chapter 4 ([Lorenzo-Gutiérrez et al., 2019](#)).

These 4 plots represent on the Y axes the differences between our colour calibration and *SDSS DR12 + RefCat2* with respect to colour. Calibration colour catalogues are represented on the X axis. Those figures show our colour calibration, plotting common stars in Guarcello's, *SDSS DR12*, *RefCat2*, and GALANTE catalogues, reflecting a linear zero point in each case except in F348M-g. Here we observe a spread ZP, but we have to note that in this case, F348M is the one calibrated using the *SDSS* library, which implies systematic errors from this catalogue (see [Lorenzo-Gutiérrez et al. \(2019\)](#)). All in all, as a result of this GALANTE photometric calibration, we show in Figure 6.7 a

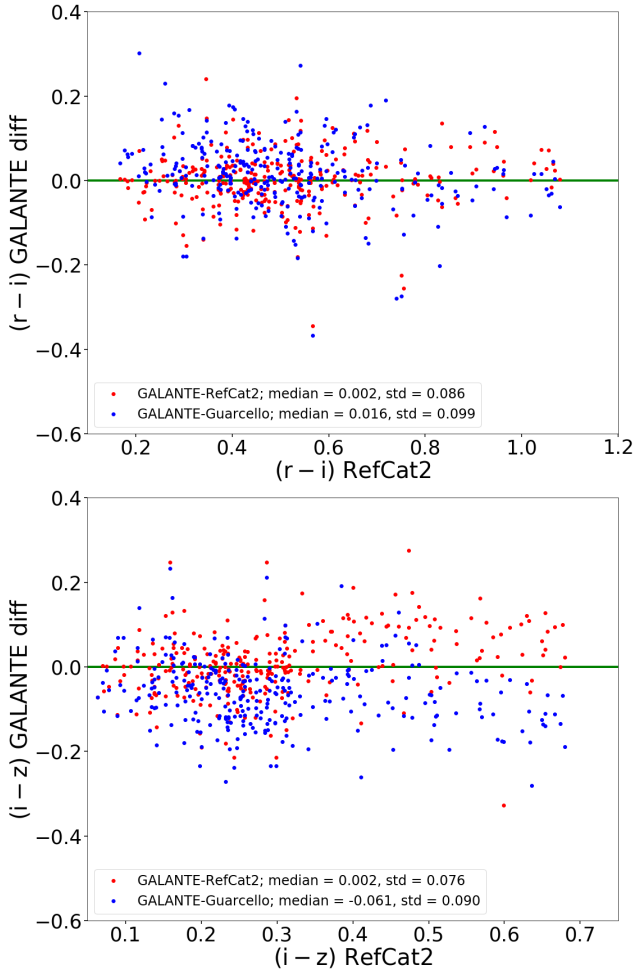


Fig. 6.5 In these figures we show in red dots the differences between GALANTE calibration and *RefCat2*. Blue dots represent differences between GALANTE and Guarcello et al. (2012) calibrations. A visual reference line is plotted in green with a 0.0 value.

bracket diagram with Cyg OB2 in this work represented in blue stars, the same as done in Lorenzo-Gutiérrez et al. (2019). We again make use of Kurucz, plotting main sequence in black and giants models in red. The green cross

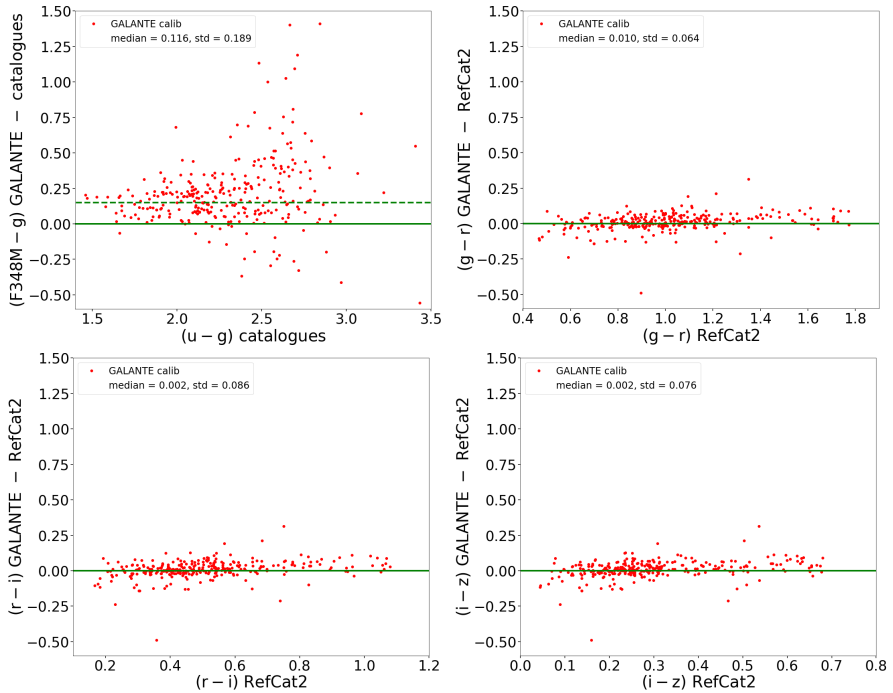


Fig. 6.6 Differences between our GALANTE calibration, u (*SDSS* DR12), and $griz$ (*RefCat2*). We take common stars between our observations, Guarcello, *SDSS* DR12, and *RefCat2* catalogues. Green continuous lines are drawn as a visual reference, while the green discontinuous line in $y=0.149$ marks the ZP between F348M and u .

error bar represents realistic median std errors in both axes, taking into account the ZPs between instrumental fields, photometric and calibration errors.

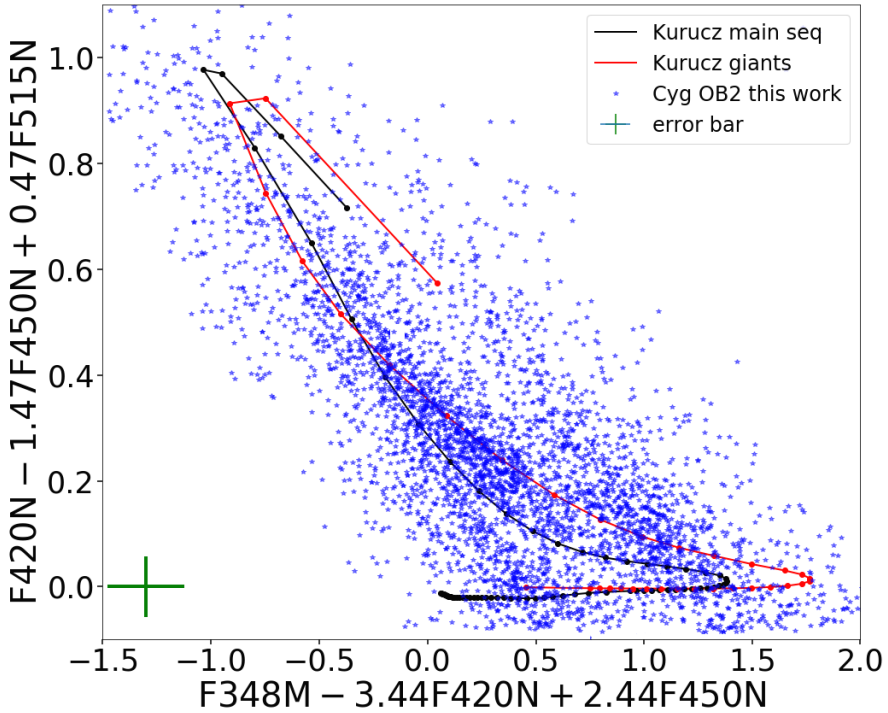


Fig. 6.7 Bracket diagram using the GALANTE filters. We make use of Kurucz, plotting main sequence in black and giants models in red. Green cross error bar represents realistic median std errors in both axes, taking into account the ZPs between instrumental fields, photometric and calibration errors.

"... but now you come to me and you say, 'Don Corleone, give me Justice.' But you don't ask with respect, you don't offer friendship; you don't even think to call me Godfather. Instead, you come into my house on the day my daughter's to be married and you ask me to do murder for money."

Vito Corleone to Bonasera

7

Deriving physical properties of Cygnus OB2 with MASTER

Contents

7.1	Models in MASTER to study Cygnus OB2	142
7.2	Physical stellar derived from K+T theoretical libraries	142
7.2.1	Comparison with previous results	149
7.2.2	Reddening estimation with Gaia DR2	153
7.3	Physical stellar derived from C+T theoretical libraries	160
7.4	Gaia DR2 comparison	167

Once we have a calibrated photometry of our observations for the GALANTE bands and with the MASTER algorithm already studied, we can introduce our catalogue in MASTER to study the results that we derive. In this chapter we show and compare the stellar physical properties derived from MASTER for the K+T and C+T set of models. To perform this study, we make comparisons of the effective temperature and surface gravity with previous studies in the Cygnus region. Using the recent Gaia DR2 catalogue both photometrically and cinematically and spatially, with the results derived from MASTER, we can also characterize the region of the sky observed with the PARSEC and MIST isochrones. In order to compare our results with other studies, we compare with the catalogue of OB stars by [Wright et al. \(2015\)](#) and the Galactic O-Star Spectrometric Survey (GOSSS) included in its respective publications ([Maíz Apellániz et al., 2019b](#); [Sota et al., 2013](#)), which are two spectrometric libraries that already classify OB stars in the Cyg OB2 association.

To make possible a direct comparison of the extinction we obtain with MASTER, a difference of two monochromatic excesses $E(4405-5495)$, and the classic colour excess typically found in the literature, $E(B-V)$, we get an equation that relates both reddening. The data to establish this relationship come from the analysis carried out by [Maíz Apellániz \(2013a\)](#), where the variation of the monochromatic excess is presented depending on the temperature of the star and the value of the reddening. The relationship obtained is shown in Equation 7.1.

From the data used by the author, we obtain empirically through a multi-linear fitting, the relationship between colour excess $E(B-V)$, $E(4405-5495)$ and $\log(T_{\text{eff}})$ for $R_{5495}=3.1$:

$$E(B - V) = 0.8955 \cdot E(4405 - 5495) + 0.1933 \cdot \log(T_{\text{eff}}) - 0.7258 \quad (7.1)$$

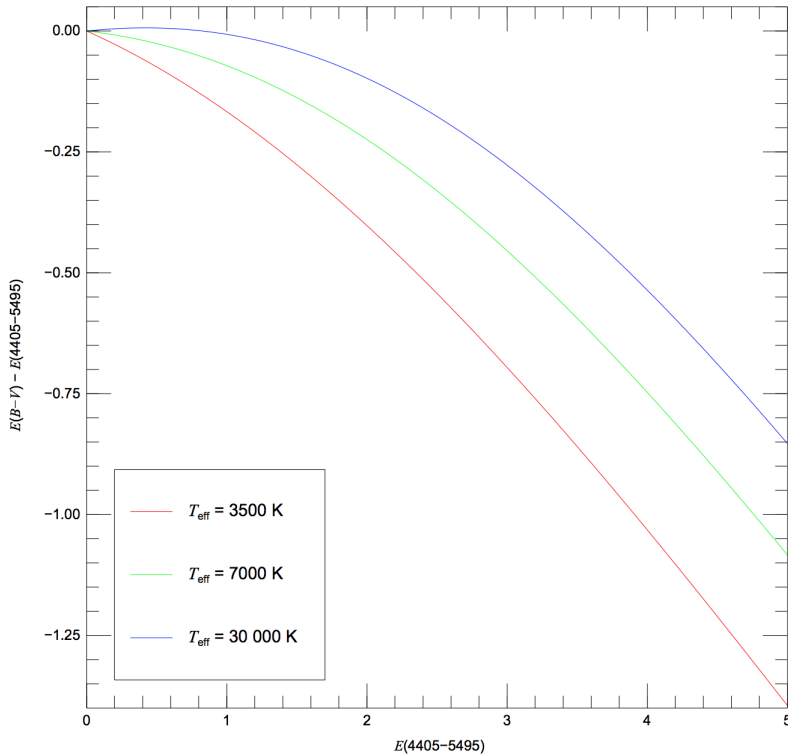


Fig. 7.1 Differences between $E(4405-5495)$ and $E(B-V)$ as a function of $E(4405-5495)$ using $R_{5495}=3.2$ and three MS stars for different T_{eff} . Figure taken from [Maíz Apellániz \(2013a\)](#).

From Equation 7.1, we will transform the values of this stellar physical variable $E(4405-5495)$ derived using MASTER to $E(B-V)$ to fairly compare with previous works in the Cyg OB2 region that we will analyze in this chapter. We note that this equation has a functional validity that allows to eliminate biases, but that can introduce greater inaccuracy in the determination of $E(B-V)$.

7.1 Models in MASTER to study Cygnus OB2

Once we have calibrated our 7 GALANTE bands, it is time to take advantage from MASTER once we tested it with NGSL as probe catalogue. Due to Cyg OB2 is a region where we expect to find hotter and more massive stars than in NGSL (Comerón et al., 2002; Hanson, 2003; Johnson & Morgan, 1954; Massey & Thompson, 1991; Wright et al., 2015), we need to select a grid of models in order to cover OB stars, but also a wide range of physical parameters for colder stars. We use in this case the Kurucz model library (Castelli et al., 1997), adding the TLUSTY library to ensure a better coverage of massive stars. Furthermore, combination of Kurucz and TLUSTY give us a denser grid of models in the temperature range of OB stars. With the idea of covering the maximum temperature range, in addition to other stellar physical parameters, we expanded the Kurucz theoretical library with the TLUSTY OB stellar models (Lanz & Hubeny, 2003). We will then compare these results with those derived from using the Coelho (2014) and the TLUSTY models. We only consider stellar models with solar metallicity in both cases (Grisoni et al., 2019).

In this study we do not use the catalogue of WD stellar models because, as we showed in Chapter 5, it can introduce some biased results by indistinguishability between the SEDs of MS and WD stars for temperatures higher than 30 000 K (see Figure 5.18).

7.2 Physical stellar derived from K+T theoretical libraries

Once we have run MASTER for this Galactic region, we have obtained T_{eff} , $\log g$ and extinction for each single star. In order to compare whether our results from MASTER could be affected by clearly appreciable systematic errors, we have drawn a $\log g$ vs $\log(T_{\text{eff}})$ diagram for our sample,

along with a set of isochrones from the Geneva group (Ekström et al., 2012) (<https://www.astro.unige.ch/syclist/index/>) in Figure 7.2. It is important to remember that with the T-80 we obtain 2 square degrees images in each field, so in our 5.60 square degrees, we expected a huge variety of stars, not only OB stars but a complete sample of stars from the Disk.

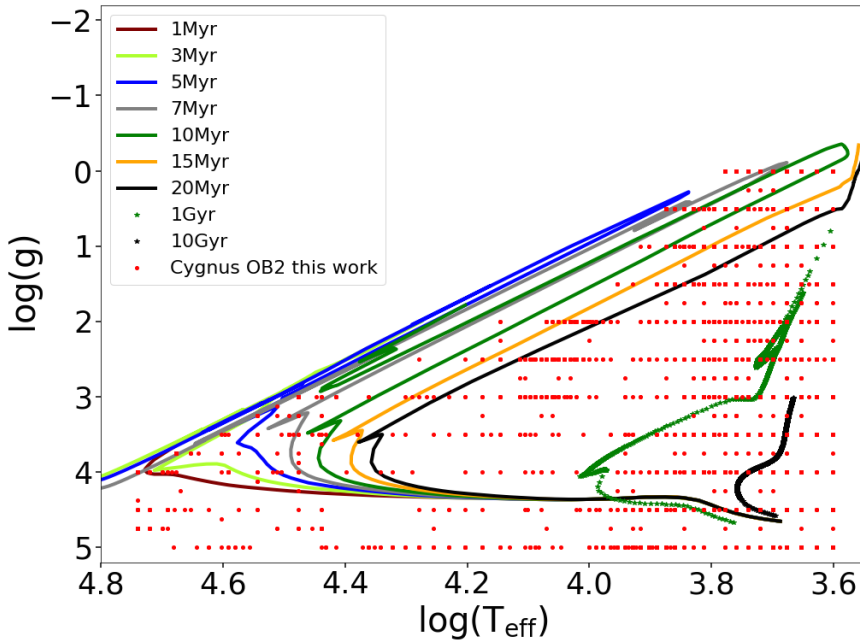


Fig. 7.2 Output physical parameters for Cyg OB2 stars from MASTER using K+T theoretical libraries with Geneva isochrones (Ekström et al., 2012). We plot in this figure observed stars in red dots. Isochrones between 1 and 20 Myr, in continuous colour lines, completing with 1 and 10 Gyr in green and blue dots, respectively.

We have $\log g$ values knowing some properties from stars like initial mass M , T_{eff} , and their bolometric magnitude M_{BOL} , following next equation:

$$\log g = \log(M) + 4 \log(T_{\text{eff}}) + 0.4 \log(M_{\text{BOL}}) - 12.49 \quad (7.2)$$

With equation 7.2, we plot in this figure isochrones between 1 and 20 Myr, in continuous colours, completing with 1 and 10 Gyr in green and blue dots, respectively. We see that the derived values for the objects do not correspond to what one would expect from a stellar cluster or association harbouring a single stellar population. This figure shows young stars from the main sequence mixed with cooler stars, both from the main sequence and giants of different ages. This age range for such association is compatible with the presence of pre-main-sequence stars (PMS). In order to explore in a visual way, we overprint PMS evolutionary tracks from *MIST* (Choi et al., 2016; Dotter, 2016) to our results in Figure 7.3.

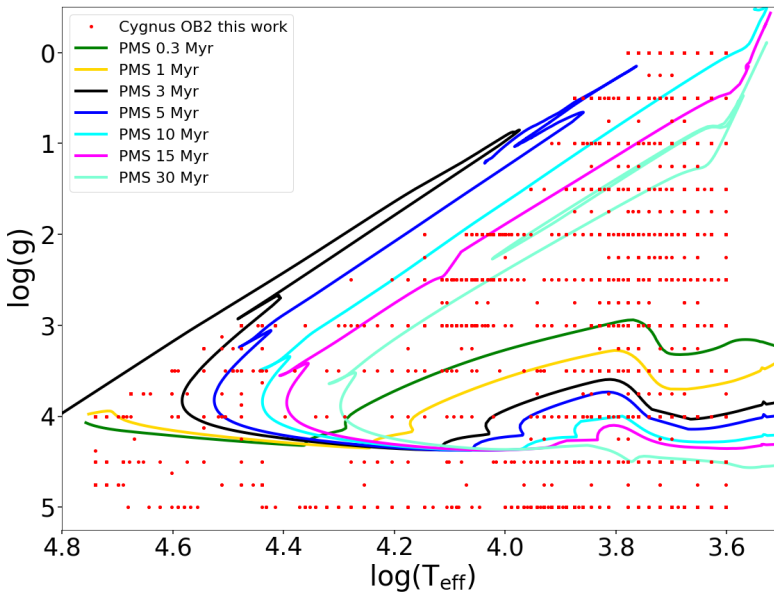


Fig. 7.3 PMS evolutionary tracks from *MIST* (Choi et al., 2016; Dotter, 2016) overprinted on our results using MASTER for the GALANTE observations.

We also represent an A_v extinction map in Figure 7.4 from our results in MASTER with K+T libraries. In the darker blue colour is shown a zero extinction value while in the redder colour is the maximum value of $A_v=10$.

In this type of figures it should be taken into account that it is a representation in 2 dimensions, in which not only is a wide field region being observed, but also collects all the objects observed along the line of vision. The patchy structure is not necessarily representative of the absorption at the very Cyg OB2 association, but we have a stellar sample located at different distances where the largest reddening values for the observed direction is, in some way, driving our final map. In view of our K+T results, we obtain a distribution of extinctions with a maximum value located in $RA \approx 308.25$ and $DE \approx 41.30$, next to another in $RA \approx 308.40$ and $DE \approx 41.20$.

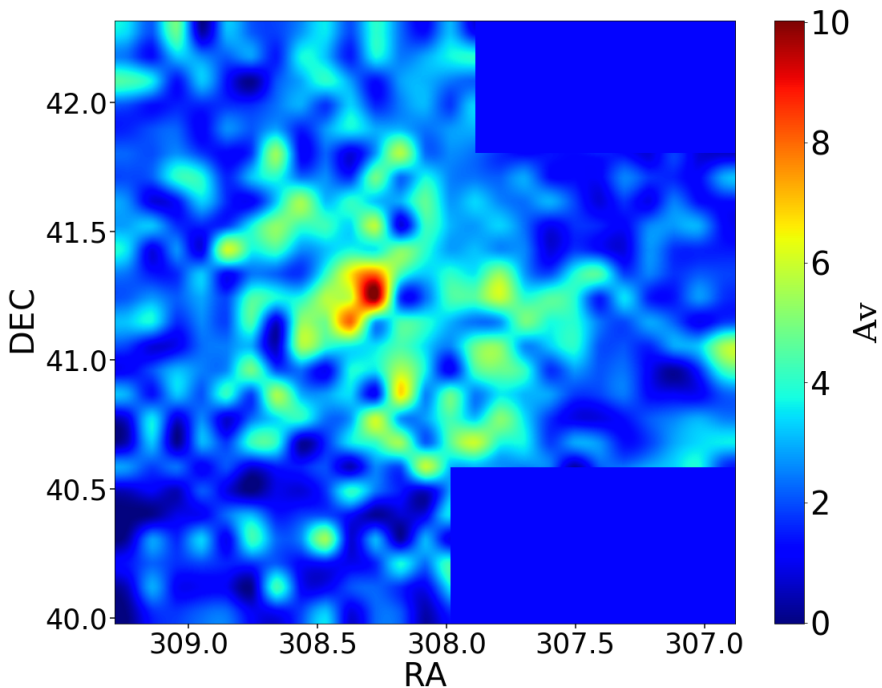


Fig. 7.4 A_v extinction map extracted from MASTER using K+T libraries. In the blue colour is shown a zero extinction value while in the red colour is the maximum value of $A_v=10$ for our region.

This result is very similar to the Voronoi tessellated extinction map in [Wright et al. \(2015\)](#) (see Figure 7.5), where the authors find a region of maximum extinction in $308.22 < \text{RA} < 308.15$ and $41.30 < \text{DE} < 41.15$, showing another small area of high extinction in $\text{RA} \approx 308.35$ and $\text{DE} \approx 41.25$.

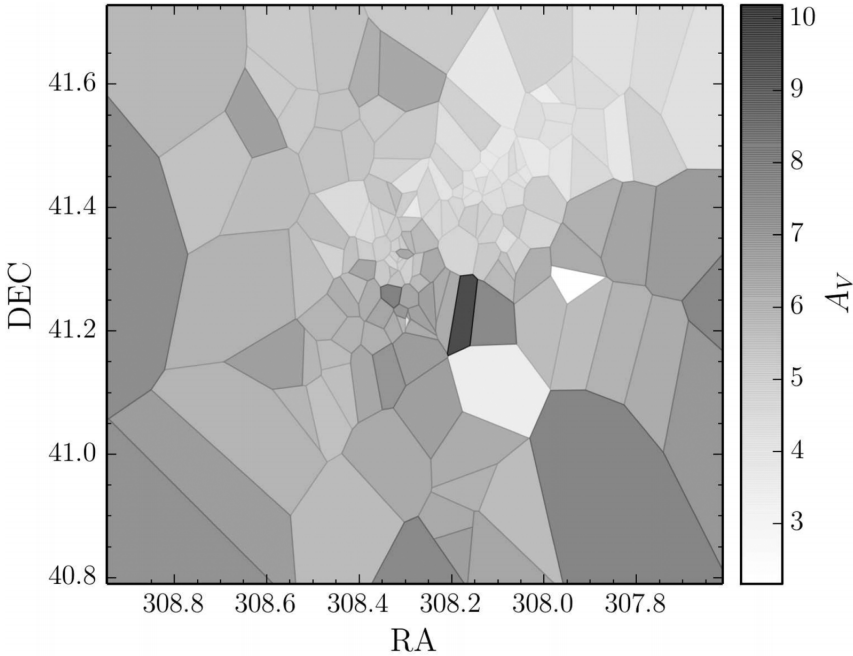


Fig. 7.5 Voronoi extinction map for Cyg OB2. Figure from [Wright et al. \(2015\)](#) to compare with the results of this study.

To see how this extinction map changes with distance, we represent in Figure 7.6 the absorption we get before (left) and after (right) 1 kpc away. Up to 1 kpc of distance, the absorption distribution in the observed area shows low levels of extinction, except in 2 zones. One of them, focused on $\text{RA} \approx 308.25$ and $\text{DE} \approx 41.30$, seems to be part of the high extinction found in Cyg OB2. This leads us to think that Cygnus can extend from just before 1 kpc away, being an association with a high level of structure and high extension.

If we look at the distribution of absorptions beyond 1 kpc (right plot), we see how we have no observations throughout the field, showing a more variable colour map with higher extinctions. This lack of data to generate a complete map is due to the opacity of the areas with a very high extinction and that we cannot observe with our photometry in the optical range. Here are 2 high extinction zones centered on $RA \approx 308.25$, $DE \approx 41.30$ and $RA \approx 308.40$, $DE \approx 41.20$, this second zone coinciding with the one found before 1 kpc, being the continuation of the cloud of gas that extends to the Cygnus region. The other area of high extinction that we find from 1 kpc and that is not seen before this distance is located in the center of Cyg OB2, which fits according to the [Wright et al. \(2015\)](#) extinction map.

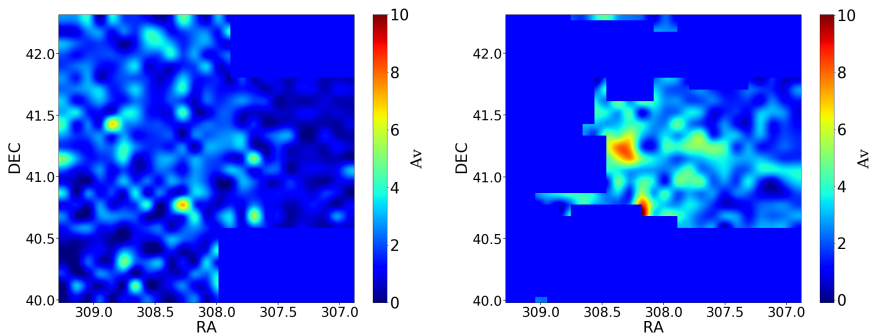


Fig. 7.6 A_v extinction map, using K+T libraries, before (left) and after (right) 1 kpc. In the blue colour is shown a zero extinction value while in the red colour is the maximum value of $A_v=10$ for our region.

The results for all stars observed in this region is shown in an A_v histogram in Figure 7.7 where we can see a large amount of stars with $A_v < 1$, which is also showed in Figure 7.2 which can be late-type stars with a $\log(T_{\text{eff}}) < 3.8$. This histogram again shows the correlation between A_v and T_{eff} , reflecting how complicated can this region be in order to estimate the physical parameters.

We are crossing the Local Spiral Arm with a low angle of inclination (16 degrees) (Figure 7.8), so we find different stars-forming regions with a high

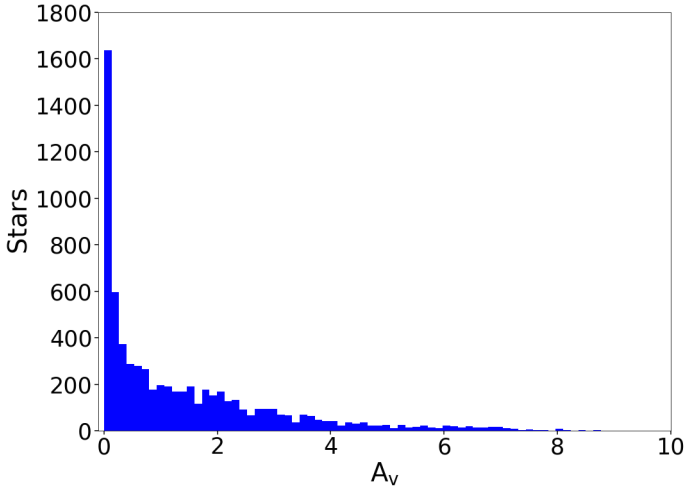


Fig. 7.7 A_v histogram of stars observed in the GALANTE region, whose values has been derived from MASTER.

degree of structure. This also shows a complicated distribution of dust in the region, so that even within the small observation cone, there are directions that have different absorptions for the same distance. Figure 7.8 shows in gray points our observations. In red we have represented those masers of water and methanol identified in the study of Reid et al. (2014) and the positions of methanol masers associated with ultracompact HII regions studied by Hu et al. (2016) are represented in blue squares. We have made a linear fitting to the masers of methanol, which these authors associate with the Local Arm. The estimation of the width of the spiral arms depends, to a large extent, on the spiral arm tracer that we are using, the size of the Galaxy and its location within it. (Lin et al., 2017; Yang et al., 2019). So that we can find widths that range from 300 pcs to 1 kpc. In this particular case, we are considering a half-width of 500 pcs, which includes the Sun at its inner edge (red circle), as it does Reid et al. (2014), considering these lines are merely descriptive.

As these authors refer, the masers of water and methanol are associated to areas of star formation with very massive young stars. Maser distance has been estimates by Very-Long-Baseline Interferometry (VLBI) techniques. If we look closely at the observed area for our study with the results obtained by these works, we see how at a Solar distance of ~ 1520 pc the authors find a high concentration of methanol and water masers, and very close to the fiducial line defining the center of the spiral arm. Our line of sight is crossing this maser concentration and our farther stars appear also to be at the same position that G079.735+0.990 ultracompact HII region located at $Y = 2400$ and $X = 450$.

7.2.1 Comparison with previous results

We compare our results with those tabulated in literature from [Wright et al. \(2015\)](#), which contains a OB spectroscopic library focusing on Cyg OB2. These authors include spectral type, extinction and effective temperature in their catalogue. We also compare with the Galactic O-Star Spectroscopic Survey (GOSSS) ([Maíz Apellániz et al., 2011](#)), which collects stellar information for 590 O, and for 11 later spectral-type stars, using the extinction values R_{5495} from [Maíz Apellániz & Barbá \(2018b\)](#). Table 7.1 shows the values obtained for T_{eff} , $\log g$ and $E(B-V)$ from the C+T and K+T models for common stars with the GOSSS and [Wright et al. \(2015\)](#) catalogues. To estimate the T_{eff} and $\log g$ values from the spectral type in the GOSSS library, we adopt the following relationships from different previous studies: O stars from [Martins et al. \(2005\)](#), B stars from [Trundle et al. \(2007\)](#) and, if they miss any spectral type of the above, we use [Humphreys & McElroy \(1984\)](#). For those stars without $\log g$ estimations we wrote -9999. Here the GOSSS ID is tabulated (GOS_ID), the spectral type and luminosity class of the GOSSS catalogue (GOS_STO) obtained by private communication with Maíz Apellániz, leffective temperature (T_{eff} GOSSS) and superficial gravity for this library ($\log(g)$

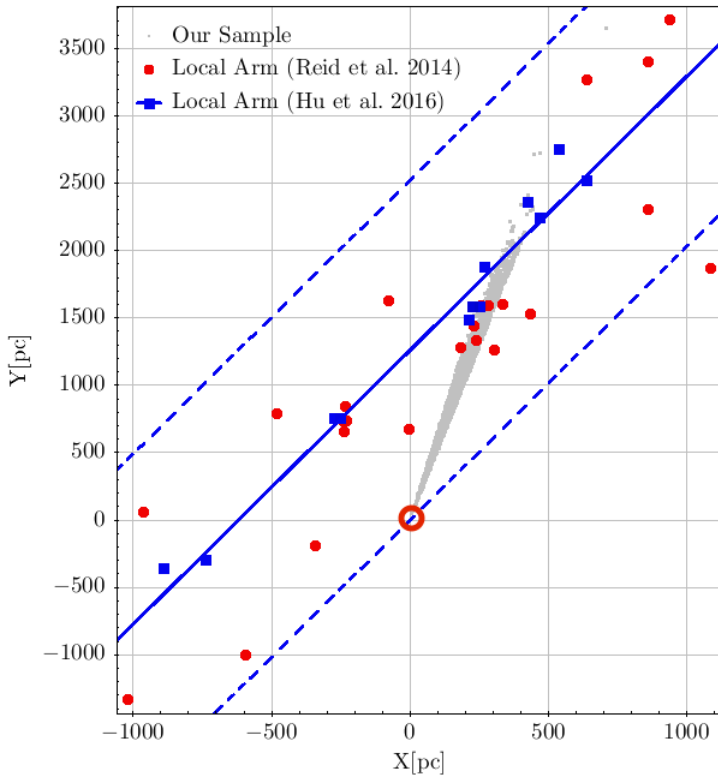


Fig. 7.8 We represent in gray points our observations and in the red circle the Sun, showing our pointing in the Local Arm. Water and methanol masers identified in the study of Reid et al. (2014) in red dots and the positions of methanol masers associated with ultracompact HII regions studied by Hu et al. (2016) in blue squares.

GOSSS) in addition to the value of extinction values R_{5495} , followed by Gaia's DR2 ID (Gaia_ID), spectral types (SpType_Wright), effective temperatures (Teff_Wright) and colour excesses (EBV_Wright) tabulated by Wright et al. (2015), including the values of these stellar physical parameters obtained with the GALANTE photometry using the K+T and C+T model sets.

Table 7.1 Values obtained from T_{eff} , $\log g$ and $E(B-V)$ using the C+T and K+T models in this study for common stars with the GOSSS and Wright et al. (2015) catalogues.

GOS_ID	GOS_STO	Teff_GOSSS	log(g)_GOSSS	R _{avg} _GOSSS	Gama_ID	SpType_Weight	Teff_Weight	EBV_Weight	Teff_K+T	log(g)_K+T	EBV_K+T	Teff_C+T	log(g)_C+T	EBV_C+T
079308+01.08_01	B0.7Ib	2730	-9999	-9999	2067813005390784896	B0.7Ib	26302	2.38	47500	3.75	2.08	47500	3.75	2.08
079314+01.62_01	B0:V	30650	-9999	-9999	2067768195993175936	B0:V	27542	2.32	30000	3.00	2.07	30000	3.00	2.08
079324+01.67_01	B2V	22100	-9999	-9999	20677692925441561586	B2V	21877	1.95	33000	4.00	1.95	32500	3.75	1.95
079354+01.16_01	O7Iaf+O9Iaf	33326; 29569	3.39; 3.23	3.00	2067818353010251776	O7Ia+O9I	34673	2.60	47500	3.75	2.50	47500	3.75	2.48
079355+01.67_01	O8V	36250	-9999	-9999	2067769490049067648	O8V	34673	2.03	55000	4.00	2.09	55000	4.75	2.14
079391+01.69_01	B0Ia	28550	-9999	-9999	2067711533186357888	B0Ia	31802	2.10	55000	4.75	2.10	55000	4.00	2.08
079392+01.01_01	B0:II	27300	-9999	-9999	2067826363267016612	B2V	21877	2.02	40000	3.50	1.87	47500	4.00	1.90
079393+01.48_01	B0Ib	28550	-9999	-9999	206775473121415124	B0Ib	30902	1.90	26000	3.00	1.92	52500	4.50	2.04
079397+01.98_01	O9	31524	3.91	-9999	2067826062091598976	O6V+O9III	38904	1.88	55000	4.75	1.85	55000	4.00	1.83
079398+01.17_01	B0V	30650	-9999	-9999	2067842756659081856	B0V	30902	2.32	55000	4.75	2.35	47500	3.75	2.29
080004+01.69_01	B0 V + B2: V	30650; 22100	-9999; -9999	-9999	2067772048528236240	B0V+B2V	30902	2.25	4000	5.00	0.26	4000	5.00	0.25
080034+01.94_01	O7 V	35531	3.91	2.87	2067827466541470080	O7V	37153	1.89	55000	4.50	2.01	47500	3.75	1.96
080034+01.29_01	B0Ia	28550	-9999	-9999	2067573703093919884	B0Ia	30902	2.44	47500	3.75	2.21	55000	4.75	2.25
080034+01.30_01	O6.5 III(II)	35644	3.62	3.39	2067576989737394688	O6.5III	37153	2.35	52500	4.75	2.25	55000	4.00	2.24
080044+01.11_01	O9 III + B:	31900; -9999	3.52; -9999	-9999	20678401495841051844	O9V+B8V	33113	2.21	52500	4.50	2.15	30000	3.00	2.04
080044+01.93_01	WC5	-9999	-9999	-9999	20678234545946503168	WC4	112201	0.00	4000	5.00	0.64	4000	5.00	0.55
080094+01.95_01	B0: II	30300	-9999	-9999	2067828030916671104	B3V	17782	2.06	47500	3.75	2.10	40000	4.50	2.12
080114+01.72_01	B0V	30650	-9999	-9999	2067783083091598888	B0V	30902	2.30	47500	3.75	2.18	47500	3.75	2.17
080124+01.47_01	O9.5 V	34488	3.91	-9999	2067763080691028756	O9.5V	31622	2.00	55000	4.00	2.12	55000	4.00	2.12
080124+01.91_01	O7 Iamp+sec	35000	3.39	3.16	206783094117418048	O7I+O6I+O9V	34673	1.94	4000	5.00	0.26	4000	5.50	0.18
080134+01.54_01	B0:V	27500	-9999	-9999	2067762761467806808	B0V	30902	1.85	27500	3.00	1.75	30000	3.37	1.77
080134+01.53_01	O9 V	31524	3.91	-9999	2067766579252921152	O9V	33113	1.97	55000	4.00	1.97	55000	4.75	2.02
080144+01.74_01	O9.5 V	34488	3.50	-9999	2067781903538395776	O9V+B8V	33113	2.18	47500	3.75	2.08	55000	4.75	2.12
080144+01.75_01	O3 II*	45000	3.73	2.83	2067781903538395344	O3I+O6V	42657	2.23	55000	4.00	2.16	55000	4.50	2.20
080144+01.60_01	B1 III	21110	-9999	-9999	2067767337001802496	B1III	24547	1.86	5750	4.50	0.97	35000	3.25	1.79
080144+01.68_01	O7.5 V	34419	3.91	3.05	2067780054401020544	O7.5V	35481	2.05	47500	3.75	2.00	52500	4.75	2.04
080144+01.73_01	O8 V	33383	3.91	-9999	206778181717389624	O8V	34673	1.97	30000	3.00	1.81	52500	4.75	1.94
080154+01.79_01	B0V	30650	3.50	2.91	20677829263206240	B0V	30902	2.23	31000	3.50	2.19	47500	3.75	2.21
080174+01.76_01	O5 II*	38520	3.61	3.09	2067783623515353728	O5I+O3.III	38904	2.18	55000	4.50	2.10	52500	4.00	2.09
080184+01.55_01	O9.5 V + B1:2 V	30488; 24500	3.92; -9999	-9999	2067766787246422400	B0.5V+B1.5V	27542	2.24	47500	3.75	2.12	55000	4.75	2.20
080184+01.03_01	B1 V	24300	-9999	-9999	2067835438008006016	B0.5V	27542	1.71	5750	4.00	0.77	27500	3.50	1.59
080184+01.65_01	B0V	30650	-9999	-9999	20677797952905792	B0V	30902	2.01	47500	3.75	1.93	55000	4.75	2.01
080184+01.20_01	B0	27300	-9999	-9999	206784588760744880	B1I	24547	1.28	5250	5.00	0.37	32500	3.25	1.36
080194+01.81_01	O8 V	34419	3.91	-9999	2067784516808530016	O8V	34673	2.13	52500	4.00	2.09	30000	3.00	1.97

GOS_ID	GOS_STO	Teff_GOSSS	log(g)_GOSSS	log(g)_GOSSS	R_stars_GOSSS	Gain_ID	Sptype...Weight	Teff_Weight	EBV_Weight	Teff_K-T	log(g)_K-T	EBV_K-T	Teff_K-T	log(g)_C-T	EBV_C-T
079.69+00.16.01	WN+WC	-9999;-9999	-9999;-9999	-9999;-9999	-9999	206774507687793024	WN7+CE+O7V(0)	50118	0.00	47500	3.75	2.21	47500	4.50	2.26
079.78+00.84.01	O7Ib(0)	33326	3.91	3.91	-9999	2067796787957114048	O7I	34673	2.66	47500	3.75	2.52	47500	4.50	2.55
080.19+01.10.01	O9 III+B	30737	3.52	3.52	-9999	206784750258383744	O9III	31622	1.32	39000	4.00	1.36	39000	3.50	1.32
080.21+01.00.01	O9 V	31524	3.91	3.91	-9999	206783561408871040	O9V	33113	1.46	5500	3.50	0.51	27500	3.25	1.36
080.21+00.76.01	O7.5 V	33383	3.91	2.98	-9999	206778379961328128	O7.5V	35481	1.81	47500	3.75	1.74	47500	3.75	1.74
080.21+00.71.01	O	23750	-9999	-9999	-9999	206778047755025920	B1b	24547	2.08	47500	3.75	2.06	52500	4.75	2.13
080.22+00.76.01	O8.5 V	30488	3.50	3.50	-9999	206778173274049428	O8.5V	33884	1.74	47500	3.75	1.70	30000	3.00	1.57
080.22+00.70.02	O8	39300	3.91	3.21	-9999	206778461998064480	O6.5III	37153	1.65	47500	3.75	1.59	52500	4.00	1.61
080.22+01.02.01	O7 III(0f)	34638	3.60	3.07	-9999	206783568281835376	O7III	36307	1.41	55000	4.00	1.45	47500	3.75	1.42
080.22+01.05.01	B0 Vp	30680	-9999	-9999	-9999	2067835682818353400	B0V	30002	1.38	4500	5.00	0.01	4500	5.50	0.01
080.22+00.79.02	O6 Ibm(0) + s	35747	3.91	3.30	-9999	20677846247057920	O6+O5.5 III	37153	1.56	52500	4.50	1.55	35000	3.25	1.43
080.23+00.78.01	O5 III(0f)	39507	3.68	3.06	-9999	206778246283991776	O5III	40738	1.56	47500	3.75	1.54	52500	4.75	1.60
080.23+00.79.01	O8.5 V	32522	3.91	3.01	-9999	20677802024178688	O8.5V	33884	1.65	55000	4.75	1.71	47500	3.75	1.64
080.24+00.94.01	B0 V	31900	3.91	2.86	-9999	2067781016474500864	B0V	30002	1.88	47500	3.75	1.79	35000	3.25	1.74
080.24+00.98.01	O8 V	32573	3.56	3.56	-9999	206783492694094848	O8V	34673	1.40	5750	3.50	0.46	32500	3.75	1.33
080.24+00.90.01	O8 V	33400	3.91	3.03	-9999	206783324604693632	O8V	34673	1.41	5250	5.00	0.37	58000	4.00	1.41
080.24+00.80.01	O3 I*	41551	4.551	3.73	-9999	20677850170923665104	O3I*	42657	1.70	47500	3.75	1.66	47500	3.75	1.64
080.24+00.95.01	O8.5 V	33383	3.91	2.94	-9999	206783296839974208	O8.5V	33884	1.58	35000	3.25	1.47	52500	5.00	1.36
080.27+00.81.01	O8 V	33383	3.91	3.03	-9999	2067785023661440	O6.5V	31622	1.65	4250	4.50	0.01	4500	5.00	0.01
080.27+00.88.01	O8 V	33383	3.91	2.89	-9999	206783324277076864	O8V	34673	1.46	30000	3.25	1.38	47500	4.75	1.48
080.27+00.75.01	B3 I	15780	-9999	-9999	-9999	206778230838262612	O8V	34673	1.71	55000	4.75	1.77	38000	3.25	1.61
080.27+01.01.01	B0.5 V	27500	-9999	-9999	-9999	2067832624801783040	O8V	34673	1.58	50000	4.00	1.55	35000	3.25	1.47
080.28+00.73.01	O9.5 III	30231	-9999	-9999	-9999	206778414571093252	B3I	17782	1.69	30000	3.00	1.69	35000	3.25	1.71
080.31+00.72.01	B1 III	21100	-9999	-9999	-9999	2067837263366481536	B0.5V	27542	1.22	6000	4.50	0.39	30000	3.50	1.17
080.31+00.84.01	B0:	30650	-9999	-9999	-9999	2067877910951619368	B0Ib	30002	1.84	30000	3.00	1.71	47500	3.75	1.78
080.32+00.60.01	O8 III+ O8 III	33383; 33383	3.91; 3.91	-9999	-9999	2067875127797303040	B1III	24547	1.86	52500	4.00	1.82	30000	3.00	1.69
080.34+00.84.01	O7 Vp	35531	-9999	-9999	-9999	206787935405188992	B0V	30002	1.86	50000	4.75	1.99	47500	4.75	1.98
080.34+00.84.01	O7 Vp	35531	3.91	3.91	2.92	206780241460492544	O8III+O8III	33884	2.02	30000	3.00	1.88	52500	4.00	1.99
080.34+00.82.01	B5 Vp	16300	-9999	-9999	-9999	20678815487153312	B5V	37153	1.78	55000	4.75	1.79	40000	3.50	1.70
080.44+00.91.01	O8.5 V	32522	3.91	2.87	-9999	206788131250301440	B5V	15848	1.84	30000	3.00	1.78	47500	3.75	1.90
080.48+00.92.01	O8 V	33383	3.91	-9999	-9999	206792979440714752	O8V	34673	2.08	55000	3.75	2.06	47500	4.75	2.01
080.53+00.67.01	O...	-9999	-9999	-9999	-9999	2067802755656754532	B1.5III	22908	1.84	39000	4.00	1.83	55000	4.00	1.85
080.53+00.80.01	O9 V	31900	3.01	2.99	-9999	206788702024913216	O9V	33113	1.75	55000	4.00	1.75	58000	4.5	1.77
080.54+00.73.01	O7 V + O9 V	35531; 31524	3.91	2.63	-9999	2067883820810670336	O7V+O9V	37153	2.23	52500	4.75	2.15	52500	4.50	2.13
080.55+00.80.01	O7 V	35531	3.92; 3.91	3.13	-9999	2067887849000094848	O7V	37153	1.72	31000	3.25	1.64	55000	4.75	1.74
080.57+00.83.01	O5 I(0f)	37070	3.56	3.13	-9999	206788821887234304	O5I+O4V	38904	1.74	55000	4.00	1.71	55000	4.00	1.71

We begin by comparing the extinction value, which, as we have already mentioned, can be correlated with the estimate of the effective temperature. If we look carefully at the table, we see that the greatest A_V discrepancies are mainly found for the spectral type stars between O8 and B1, of luminosity class V. The reddening solution shows degeneration for these spectral types, as they have SEDs perfectly compatible with very low extinction G-type stars. That is, small errors in photometry can lead us to choose one or the other solution depending even on the models, as we will discuss later. Other differences are because we are estimating double and triple systems as an isolated star or that the spectral type of it is not included within our models (*e. g.* WR star). Another feature that we observe and whose discussion we will expand later is that we get higher temperatures than those tabulated by these authors, especially when we exceed 30 000 K.

7.2.2 Reddening estimation with Gaia DR2

We make use of the Gaia DR2 release (Evans et al., 2018; Gaia Collaboration et al., 2016), for comparing our reddening estimations with those listed in this release. We have 132 stars in common with Wright et al. (2015), GALANTE and Gaia. To make this comparison, we transform the absorption tabulated by Gaia DR2, A_G , into A_V , for which we make use of the recent study of Wang & Chen (2019) in which they analyze the extinction coefficients between different wavelengths and filters where, among them, they compare A_V and A_G . From this study, we adopt:

$$A_G/A_V = 0.789 \quad (7.3)$$

As we see in Figure 7.9, transformation is not linear, showing a high dependence on the effective temperature and the value of its extinction. In addition, this relationship between both absorptions depends on the author, having an average value of 0.90 if we attend to Andrae et al. (2018). For OB

stars of Cyg OB2, we estimate that A_G/A_V should be between 0.8 and 0.9 depending on the case. However, since the uncertainty of our photometry can reach up to 0.1 mag, the value we adopt is more than enough to compare the results of interstellar absorption with the values of [Wright et al. \(2015\)](#) and Gaia DR2. Especially since the patterns that come out of this comparison are not the product of an A_G/A_V more or less precise but of other causes that are determined by the chosen models and the uncertainties in the photometry.

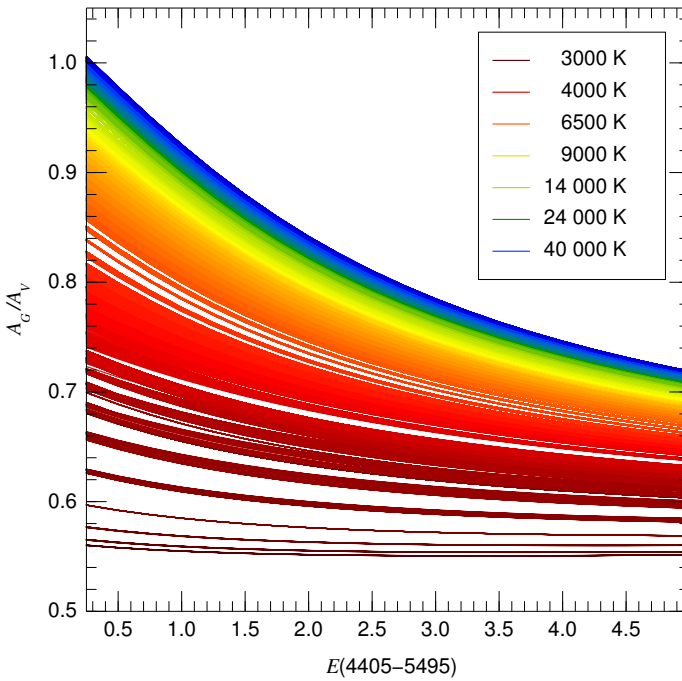


Fig. 7.9 A_G/A_V as a function of the amount of extinction $E(4405 - 5495)$ using the SED models of [Maíz Apellániz \(2013b\)](#) for solar metallicity and luminosity class range from 0.0 (hypergiants) to 5.5 (ZAMS), colour-coded for T_{eff} between 3 000 K and 52 500 K. The extinction law used is the one from [Maíz Apellániz et al. \(2014\)](#) with $R_{5495} = 3.0$ and the filter sensitivity curves are those of [Maíz Apellániz & Weiler \(2018\)](#) for G and [Maíz Apellániz \(2006\)](#) for V .

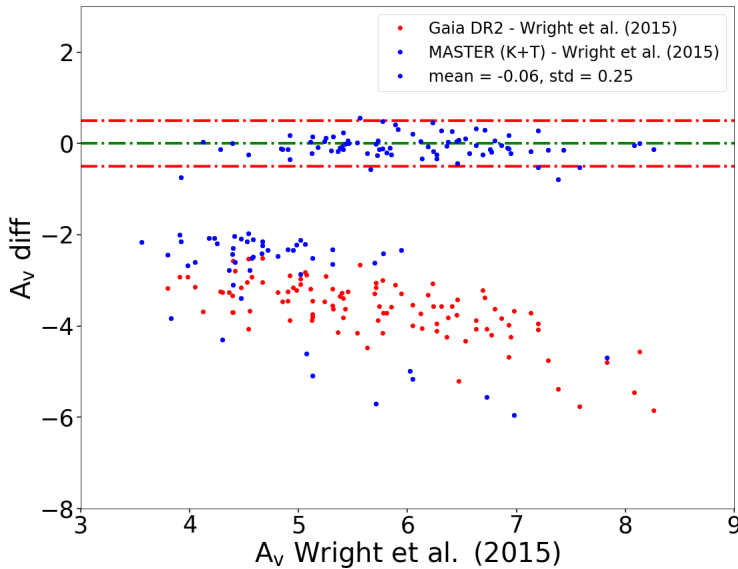


Fig. 7.10 A_v differences between the three catalogues versus A_v values from bibliography [Wright et al. \(2015\)](#). Values in GALANTE are extracted from MASTER using K+T libraries. We represent in red dots differences with Gaia DR2, in blue differences with GALANTE and in green is plotted the zero comparison line, using [Wright et al. \(2015\)](#) as comparison values. Red discontinuous lines are the 2σ from the differences.

Figure 7.10 shows a comparison between GALANTE observations and those of [Wright et al. \(2015\)](#) and Gaia DR2 common stars for the Cyg OB2 region versus A_v values determined by [Wright et al. \(2015\)](#). First we start comparing with the results obtained with MASTER using the K + T libraries. We represent in red dots differences between [Wright et al. \(2015\)](#) and Gaia DR2, in blue differences between spectroscopic values and GALANTE and in green is plotted the zero comparison line, using [Wright et al. \(2015\)](#) as comparison values. As we appreciate in comparing MASTER's results with [Wright et al. \(2015\)](#), there are 81 stars belonging to Cygnus OB2 with very similar A_v values to those obtained with the spectroscopic study of these

authors. In these differences we get an average value of -0.06 , with a standard deviation of 0.25 . For better visualization, we use the value of 2σ encompassing these differences with red dashed lines, marking on a green dashed line the null difference value as a visual reference. Most of the stars that present a great discrepancy with the spectroscopic estimates are distributed around a difference of -2 magnitudes. The constant value of difference for these stars, independent of the extinction defined by [Wright et al. \(2015\)](#), made us think of a bias introduced in the estimation of the physical variables of the stars. The explanation, in a schematic way, comes from the fact that an error of the order of the tenth, as it corresponds to our calibration, can clearly lead to a degeneration between the estimation of the temperature and the extinction, being able to give in some cases, up to three compatible solutions. [Figure 7.11](#) shows a colour-colour diagram as an example where we represent the Kurucz models (red dots) and the Coelho (blue dots) models with $[\text{Fe}/\text{H}]=0.0$ and $\alpha\text{-enh}=0.0$, which is similar to the U-B vs B-V colour diagram. We have represent in a red line the slope of these GALANTE colours when applying the law of extinction of [Maíz Apellániz et al. \(2014\)](#). Here we graphically show how the extinction curve crosses up to three times to the SEDs, being able to get for a star of $30\,000\text{ K}$ values of $7\,000\text{ K}$ or $4\,500\text{ K}$. This result is what we can get, using the six normalized GALANTE colours with our MASTER methodology, which together with the photometric error, we can find a best fitting of a B0V star like an F or G.

We also observe that most of these values correspond to the lowest spectroscopic extinctions. A more detailed analysis of the values that appear in [Table 7.1](#), highlights some points of interest: while supergiant stars show similar reddening (except for the star GOS_ID 080.12+00.91_01 which appears to be a triple system) between the spectroscopic and photometric results, the temperature obtained from the latter is always higher than the derived spectroscopically. If we look at the [Figure 5.1](#) that represent the distribution

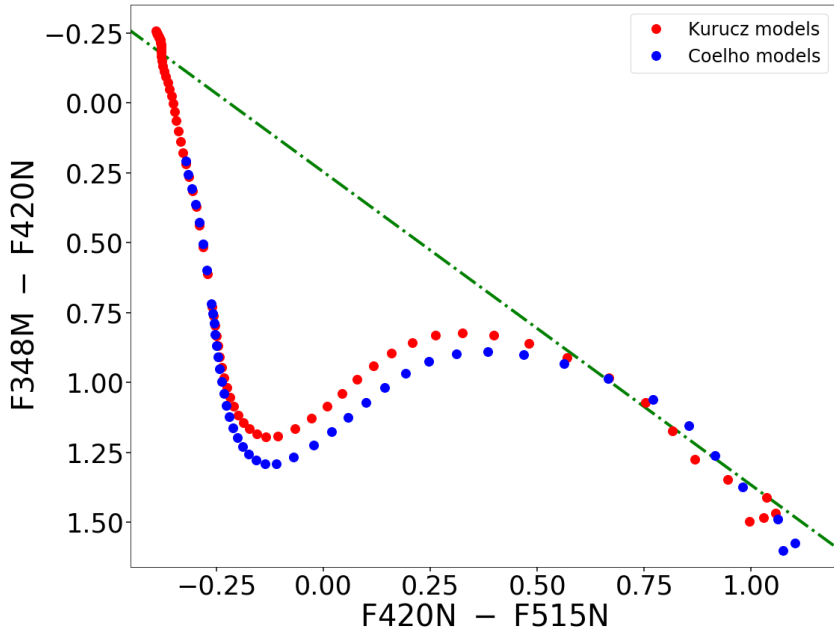


Fig. 7.11 Colour-colour diagram using GALANTE colours, similar to U-B vs B-V. It shows the degeneracy between temperature and extinction using the Kurucz (red dots) and Coelho (blue dots) models. The green line represents the trajectory of these colours when applying the law of extinction of [Maíz Apellániz et al. \(2014\)](#) for these GALANTE colours.

of the physical parameters of the models, we see that these do not cover the values obtained spectroscopically for these stars.

A significant conclusion of the comparison made with Gaia DR2, is the systemic aspect of these differences (red dots), which grow as the value of absorption increases. This is because for this Gaia data release they used models to derive the effective temperature of the stars with a top value of 10 000 K ([Andrae et al., 2018](#)), which means that for a hotter star a lower value will be derived both in temperature and extinction for, as is the case, the stars of Cygnus OB2. This manifests the correlation between temperatures and

extinction (Allende Prieto, 2016; Bailer-Jones, 2011), which is very evident in this comparison for Cygnus OB2 stars, because Gaia DR2 cannot get to use any model with a T_{eff} range of early-type stars.

In the same way, we use the GOSSS catalogue with the absorption values tabulated in Maíz Apellániz & Barbá (2018b), comparing them with the spectroscopic catalogue of Wright et al. (2015) (green dots) and the photometric GALANTE (blue dots) and Gaia DR2 (red dots) catalogues in Figure 7.12, with a total of 28 common stars. Here we see how the values tabulated by Wright et al. (2015) and those obtained in this study by the GALANTE photometry are very similar to those of GOSSS, obtaining absorption values somewhat lower than those obtained by Maíz Apellániz & Barbá (2018b) in both cases. For both comparisons we obtain a very similar median value, having a high standard deviation in the extinction derived with MASTER. As we can see, this is due to the 2 stars that are quite separated from the average value: the star with a difference greater than 5 magnitudes is the triple system O7I + O6I + O9V, while the one with an absolute difference of more than 3 magnitudes is an O8V star, which is in the zone of greatest degeneration between the temperature and extinction shown in Figure 7.11. In both cases, we can see that the value of temperature is not recovered correctly, having values between 4000 and 5000 K (see Table 7.1) for these 2 stars. On the other hand, the differences between Gaia DR2 and GOSSS once again highlight that, since Gaia DR2 is not using models of $T_{\text{eff}} > 10\,000$ K, the temperatures obtained for OB stars are colder and, therefore, with less extinction as temperatures increase as shown in the slope of these differences in red dots.

We plot in Figure 7.13 relative differences between both T_{eff} derived with GALANTE and those from Wright et al. (2015) (blue dots) and the GOSSS (red dots) catalogues. In blue dots we appreciate a high discrepancy in T_{eff} colder than $\log(T_{\text{eff}}) < 4.0$ according to our results with MASTER. These values are related to a different estimation of A_v from Figure 7.10. We see how there is a variation of the relative difference with $\log(T_{\text{eff}})$ determined by Wright

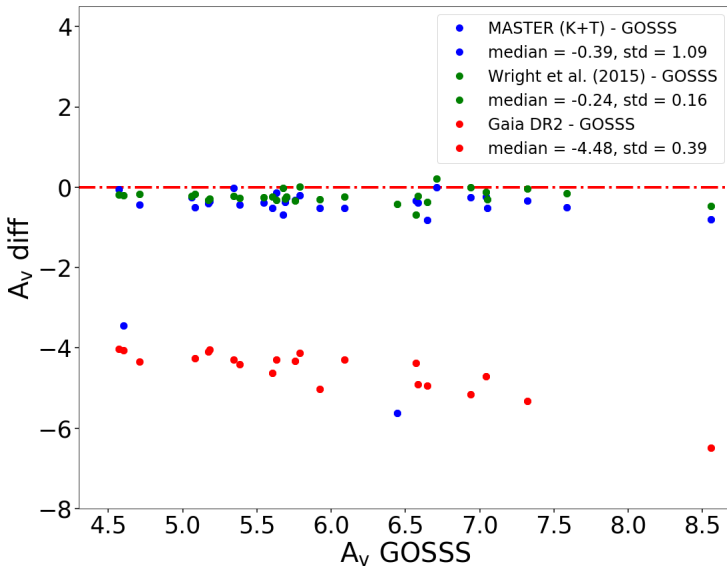


Fig. 7.12 A_V differences between GOSSS and GALANTE (K+T), Gaia DR2, and Wright et al. (2015). Red discontinuous line represents the absence of differences.

et al. (2015). This result connects in some way with the structure also found in the estimation of the extinctions obtained with MASTER using the K+T models from Figure 7.10, getting lower temperatures for the set of stars with $\log(T_{\text{eff}}) < 4.0$, and that are associated with those obtained with an extinction value below that of the authors. In red dots we represent differences between GALANTE and the GOSSS catalogue. Here we can see que the range of values in the relative differences with GOSSS is narrower than with those stars from Wright et al. (2015), obtaining values closer to 0.0. The relative differences obtained below the value -0.5 correspond to stars catalogued by GOSSS as spectral type B and luminosity class III, in addition to the binary stars and the triple system that we saw in Table 7.1. On the other hand, relative differences close to 1.0 are obtained for those stars classified as blue

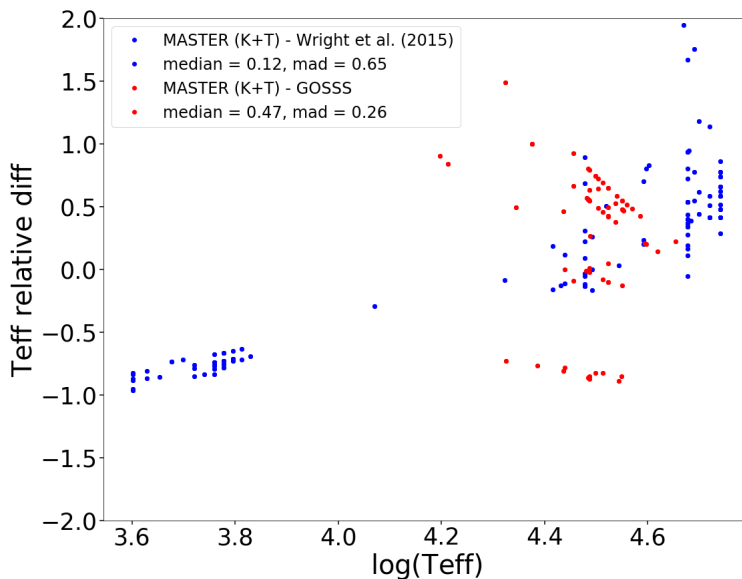


Fig. 7.13 Relative differences between T_{eff} from MASTER (K+T models), [Wright et al. \(2015\)](#) (blue dots) and the GOSSS (red dots) catalogues.

supergiants. Since our models do not cover this type of stars, MASTER finds the best fitting solution with very hot star models by applying a low reddening.

7.3 Physical stellar derived from C+T theoretical libraries

Once we have obtained the results for our observed region, we want to explore if there are changes in the results with MASTER by introducing the C+T models. As we already know, there is a correlation between the determination of effective temperature and extinction, for this reason, we focused our results with this test on the estimation of the extinction and its comparison with [Wright et al. \(2015\)](#) y Gaia DR2. Figure 7.14 shows the extinction map obtained with MASTER using the C+T theoretical libraries for the observed

region. This figure shows, analogously to the Figure 7.4 alternating again areas with very low extinction, generating similar patterns of high extinctions. If we compare these results between one and the other set of models with MASTER, we appreciate that these results show higher reddening values than with the use of K+T models, being in the same positions shown in the Figure 7.4.

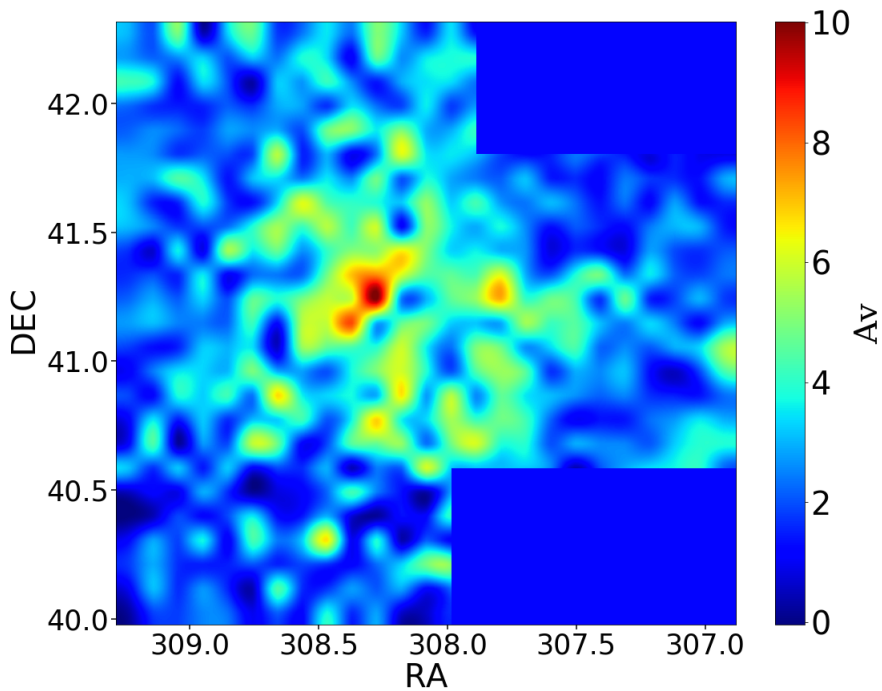


Fig. 7.14 A_v density map extracted from MASTER using C+T libraries. In the blue colour is shown a zero extinction value while in the red colour is the maximum value of $A_v=10$ for our region.

Analogously to what has been done for the K+T models, we divide the absorption we found before (left plot) and after (right plot) of 1 kpc for the C+T models in Figure 7.15. The extinction maps that we see here show similar distributions to those obtained with the K+T models (see Figure 7.6), reaffirm-

ing the idea that the cloud of gas that we see in $RA \approx 308.25$, $DE \approx 41.30$ begins before 1 kpc away and extends to the Cygnus region. This result connects with what we will see later in the study of our results when using the Gaia DR2 catalogue (Figure 7.24) where we see how the gas cloud starts around 900 pcs away.

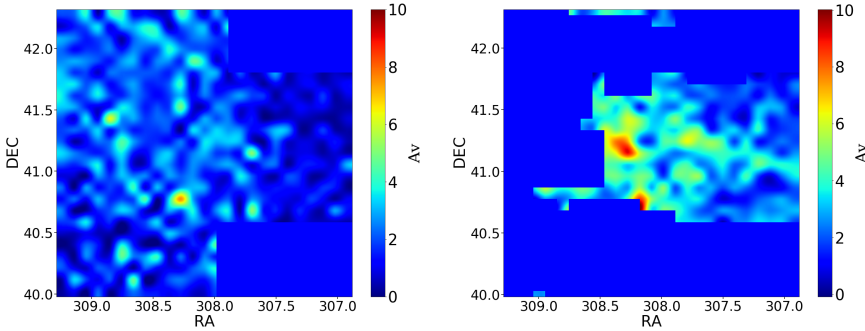


Fig. 7.15 A_V extinction map, using C+T libraries, before (left) and after (right) 1 kpc. In the blue colour is shown a zero extinction value while in the red colour is the maximum value of $A_V=10$ for our region.

A new comparison of the absorptions obtained with our results versus those tabulated by [Wright et al. \(2015\)](#) y Gaia DR2 are shown in Figure 7.16. Analogy to the representation of the Figure 7.10, in red dots we represent the differences between Gaia DR2 and [Wright et al. \(2015\)](#), while in blue dots the differences between our results with MASTER using the C+T models and [Wright et al. \(2015\)](#). Here we see a greater number of common objects with [Wright et al. \(2015\)](#) focused on the green line that visualizes 0.0, with a total of 103 stars contained in the red dashed lines (2σ). In these results we get an average value slightly higher than that obtained with the models K+T (-0.14) with a similar standard deviation. On the other hand, for the stars with a lower extinction, the 2 mag step in this difference is reproduced again, in addition to other objects, which envelope the Gaia DR2-[Wright et al. \(2015\)](#) differences.

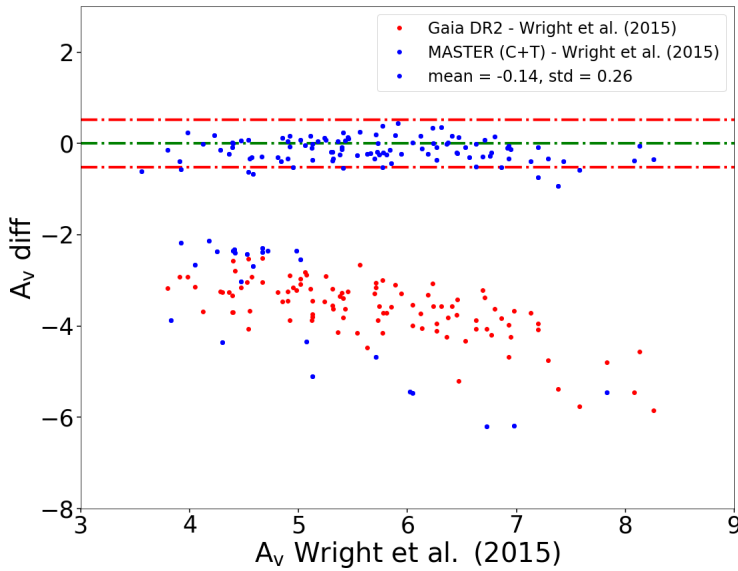


Fig. 7.16 A_v differences of common stars between GALANTE observations, [Wright et al. \(2015\)](#) and Gaia DR2 for the Cyg OB2 region versus A_v values from bibliography [Wright et al. \(2015\)](#). Values in GALANTE are extracted from MASTER using C+T libraries. We represent in red dots the differences with Gaia DR2, in blue dots the differences with GALANTE and in green is plotted the zero comparison line, using [Wright et al. \(2015\)](#) as comparison values. Discontinuous red represent the $\text{mean} \pm 2\sigma$ lines.

Figure 7.17 shows the same comparison of the extinction of the GOSSS ([Maíz Apellániz & Barbá, 2018b](#)) catalogue with the spectroscopic library from [Wright et al. \(2015\)](#) (green dots) in addition to the photometric catalogues of GALANTE (blue dots) and Gaia DR2 (red dots) for the 28 common objects as we did in Figure 7.12. For the set of C+T models we again obtain some differences with the absorption of GOSSS similar to those of [Wright et al. \(2015\)](#), obtaining in both cases values of A_v below those tabulated by [Maíz Apellániz & Barbá \(2018b\)](#) for these stars. This may be due to the fact that we have used a value of $R_v=3.1$ compared to the 2.9 used by the authors of GOSSS.

Again, we see that the differences between [Wright et al. \(2015\)](#)-GOSSS and GALANTE (C+T)-GOSSS have similar median values, obtaining a very high standard deviation in the second case due to the star with a difference of $A_V > 5$ magnitudes in absolute value. This is against the triple system O7I + O6I + O9V, while in this case, this set of models correctly recovers both the extinction and the effective temperature of the O8V star in comparison with the same analysis using the K+T models.

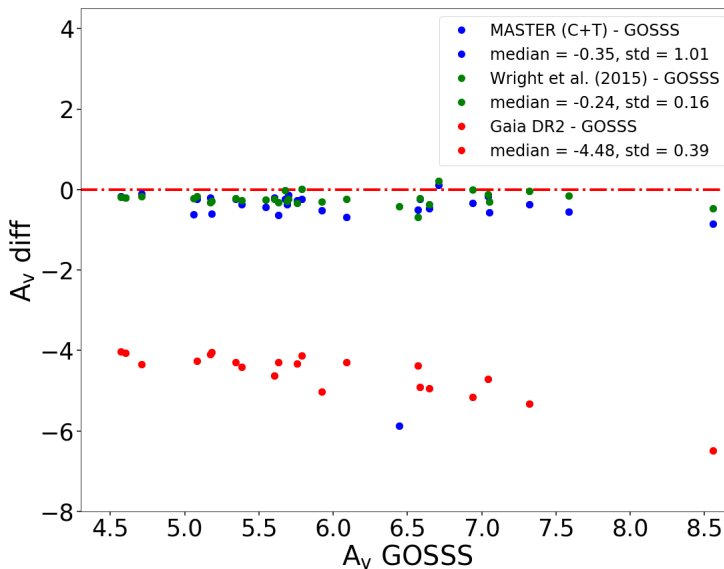


Fig. 7.17 A_V differences between GOSSS and GALANTE (C+T), Gaia DR2, and [Wright et al. \(2015\)](#). Red discontinuous line represents the absence of differences.

These results indicate that, as we saw in the study of the K+T and C+T model sets for the study of the NGSL of the Chapter 5, for a pair of C and K models whose physical parameters are the same, different colours are obtained that lead to a different derivation of stellar parameters. This can make a Cyg OB2 star fits better to a Kurucz model than to a TLUSTY. On the contrary, when using the Coelho models, a better fit with those of TLUSTY can be

obtained for that same star, resulting in a value of T_{eff} higher and with greater extinction. On the other hand we see that, for high extinction values, we derive similar values of A_V to those of [Wright et al. \(2015\)](#), whereas for low extinctions we are not able to recover the values determined by these authors. In addition to compare fitting results using spectrometry versus ours that make use photometry of 6 normalized colours using a seventh band, extinction plays a crucial role in the search for the best photometric fitting, as we have explained before.

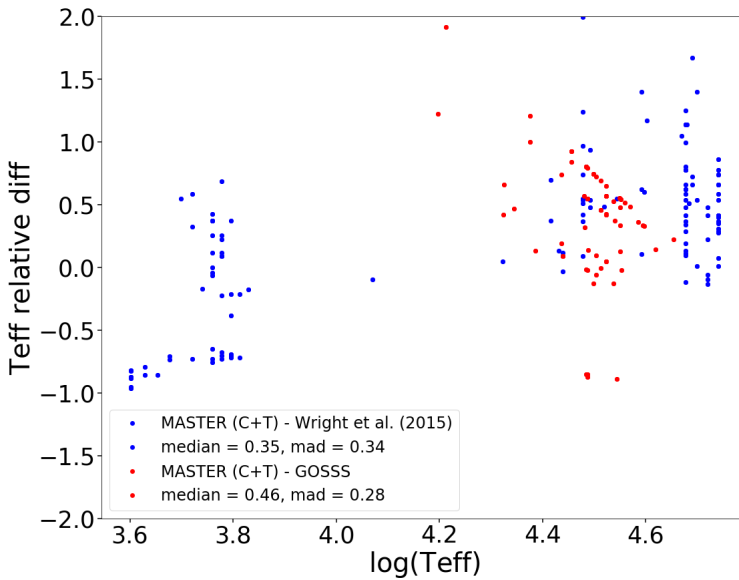


Fig. 7.18 Relative differences between T_{eff} from MASTER (C+T models), [Wright et al. \(2015\)](#) (blue dots) and the GOSSS (red dots) catalogues.

We plot in Figure 7.18 relative differences between T_{eff} GALANTE, [Wright et al. \(2015\)](#) and the GOSSS catalogue, same as in Figure 7.13. We first compare the results between GALANTE and the [Wright et al. \(2015\)](#) library (blue dots), where we see that in this case the range of relative temperature differences is more focused at 0.0 and that, on the other hand, many of the

temperatures below 10 000 K start to focus around 0.0, although there are still values below this that come from the misdetermination of A_V that we previously saw. If we now focus on the relative differences between GALANTE and the GOSSS library, we appreciate how we get results more concentrated in the 0.0 value than with the values tabulated by [Wright et al. \(2015\)](#). As with MASTER results using C+T models, we get differences around 1.0 or even higher for GOSSS blue supergiant stars due to the model gap and the effect produced in temperatures, which we previously explained. On the other hand, we recover the binary systems and the triple system listed in the GOSSS catalogue with differences close to the -1.0 value, obtaining in this case a better solution for the stars of luminosity type III, unlike the results we obtained with the K + T models, because the Coelho models have a coverage range of $\log g$ that includes this type of giant stars, as we saw in Chapter 5.

To summarize, Figure 7.19 shows T_{eff} , $\log g$ and E(B-V) comparison histograms for Cygnus OB2 in this work, using MASTER with K+T (blue colour) and C+T (red colour) theoretical libraries. The reddening-effective temperature degeneration is observed in the comparison of the results obtained with the K+T and C+T models. The number of objects with greater reddening is obtained when we fit to the C+T models, which leads to an increase in the estimated temperature for these objects. These results lead to a better agreement between the determination of physical parameters by spectroscopy from ([Wright et al., 2015](#)) and GOSSS catalogues and those determined from the GALANTE photometry.

We do not want to forget that we are using a SED defined by 6 normalized bands (colours) in the optical range, and whose uncertainty can reach the tenth of magnitude for some colours (see Chapter 4). On the other hand, the direct application of MASTER, using the whole range of parameters of the models and a reddening of up to 4 magnitudes, introduces errors and bias very dependent, not only on the uncertainty of the photometry, but on the value of the reddening itself, as seen in Figures 7.10 and 7.16. A more detailed

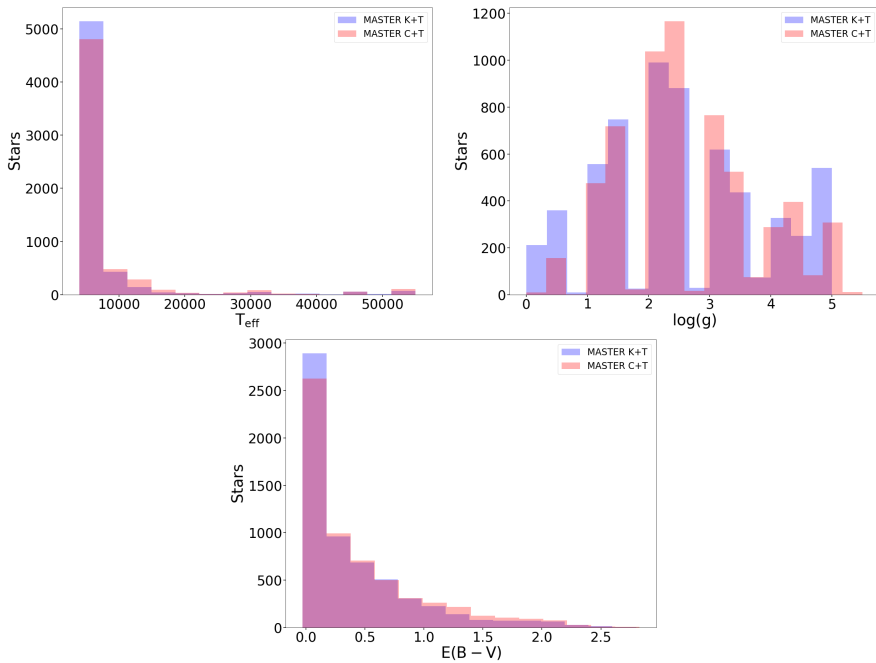


Fig. 7.19 T_{eff} , $\log g$ and $E(B-V)$ comparison histograms for Cygnus OB2 in this work, using MASTER with K+T and C+T theoretical libraries.

discussion of the capabilities and constraints of the method has been discussed above (see Chapter 5) using the NGSL spectroscopic observations catalogue as a test set.

7.4 Gaia DR2 comparison

We crossmatch with Gaia DR2 our 6765 stars from the GALANTE observations in the Cygnus association, giving as a result 6057 common stars with Gaia photometry. Figure 7.20 represents those objects with T_{eff} tabulated values in Gaia DR2 (black stars). We also superimpose hot objects ($T_{\text{eff}} > 10\,000$ K) derived from MASTER using K+T theoretical libraries (colour dots). For

them, we use a range of colours according to the temperature that we obtain from MASTER, giving colours from blue (the coldest) to red (the hottest).

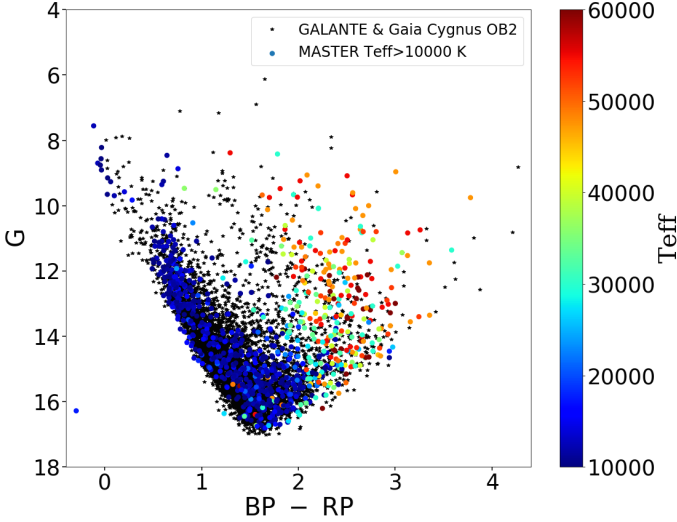


Fig. 7.20 Gaia DR2 colour-magnitude diagram with T_{eff} from MASTER using K+T theoretical libraries.

Figure 7.20 shows a wide range of spectral type for hot stars. Here we see a high concentration of OB stars with $(BP-RP) > 1.5$. Due to effective temperature and colour excess are correlated, we need to unredden these objects in order to make a better classification in this diagram. We adopt the value from the study by Wang & Chen (2019) to obtain a relationship between the colour excess $E(BP-RP)$ from Gaia DR2 and $E(B-V)$:

$$E(BP - RP) = 1.321 \cdot E(B - V) \quad (7.4)$$

Thus, we can obtain the value of G_0 and $(BP-RP)_0$ from the $E(B-V)$ derived from MASTER as:

$$\begin{aligned}
 G_0 &= G - A_G = G - 0.789 \cdot 3.1 \cdot E(B - V) \\
 (BP - RP)_0 &= (BP - RP) - 1.321 \cdot E(B - V)
 \end{aligned}
 \tag{7.5}$$

Figure 7.21 represents the same diagram of Figure 7.20, unreddening according to the Equation 7.5 for the obtained results with MASTER using K+T and C+T theoretical libraries. In both cases we represent the observed stars using colours according to their effective temperature derived with MASTER.

In both plots from Figure 7.21 we can see how, from $(BP-RP)_0 < 0.0$ we see a concentration of hot stars, which is a result compatible with the Cyg OB2 association. Again, we are seeing the results of the observation through the Local Arm, so that for distances very close to us we have old objects with a very low extinction, while the farther they are located and have a greater extinction, we observe a greater early-type stars concentration. Comparing both results, we have a higher OB determination using the Coelho theoretical catalogue, obtaining a better fitting using the TLUSTY library for some stars that have a best fitting using the Kurucz catalogue.

Now, if we attend to other physical parameter like it is $\log g$, we can complete this range of spectral class plotting Figure 7.22. Here we appreciate how the stars of the main sequence appear on the left with $(BP-RP)_0 < 0.0$ classified as OBA, mixing with giant and supergiant in $0.0 < (BP-RP)_0 < 0.8$ for both results derived by MASTER. We also see how another group of stars in the main sequence is in $(BP-RP)_0 = 0.5$. From the study in Cygnus OB2 of [Berlanas et al. \(2019\)](#), We think that this type of object can be part of a subgroup of stars located at 330 pcs, the same where the authors find a very bright star and that is taken as a contaminant of their sample. Giants and supergiants are ordered in this way for increasing values of $(BP-RP)_0$.

We can calculate the absolute magnitude referred to the G band (M_G) as

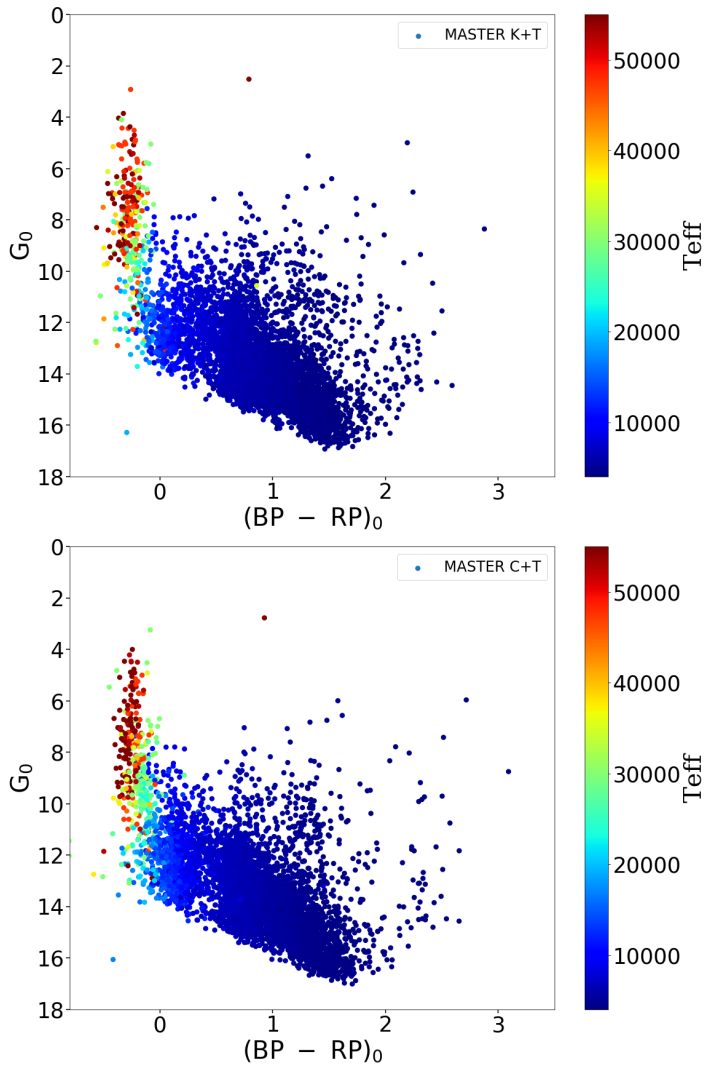


Fig. 7.21 Unreddened Gaia DR2 colour-magnitude diagram.

$$M_G = G_0 - 5 \cdot \log(d) + 5 \quad (7.6)$$

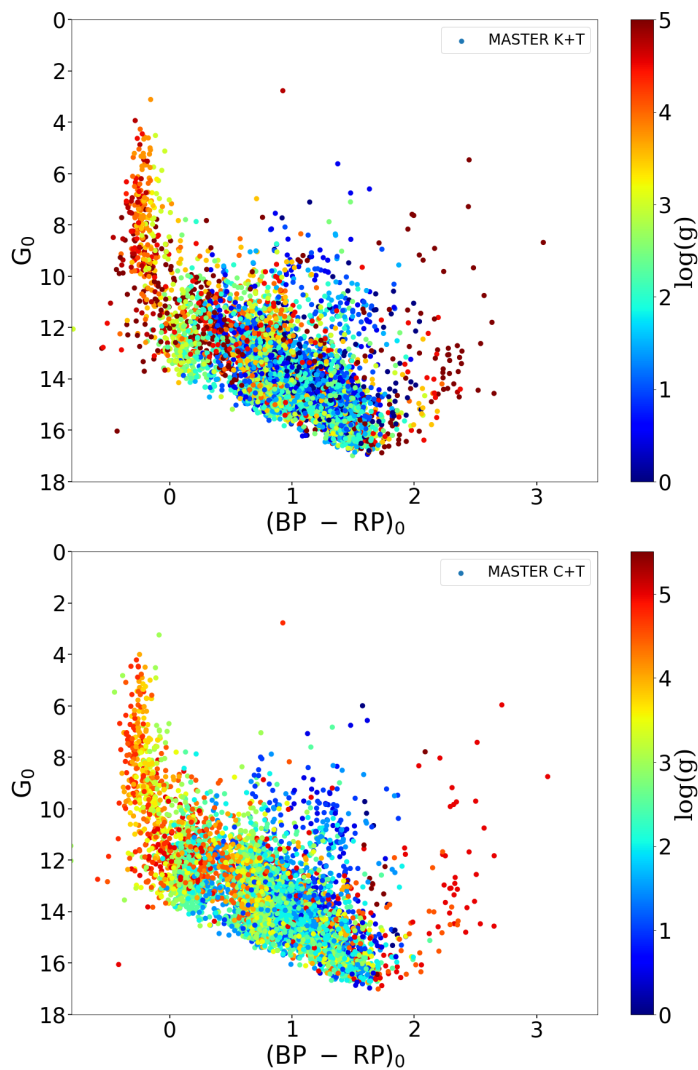


Fig. 7.22 Unreddened Gaia colour-magnitude diagram with $\log g$ from MASTER.

being d the distance estimated by [Bailer-Jones et al. \(2018\)](#) for the objects of Gaia DR2, whose author assumes that the members cover a small range of distances.

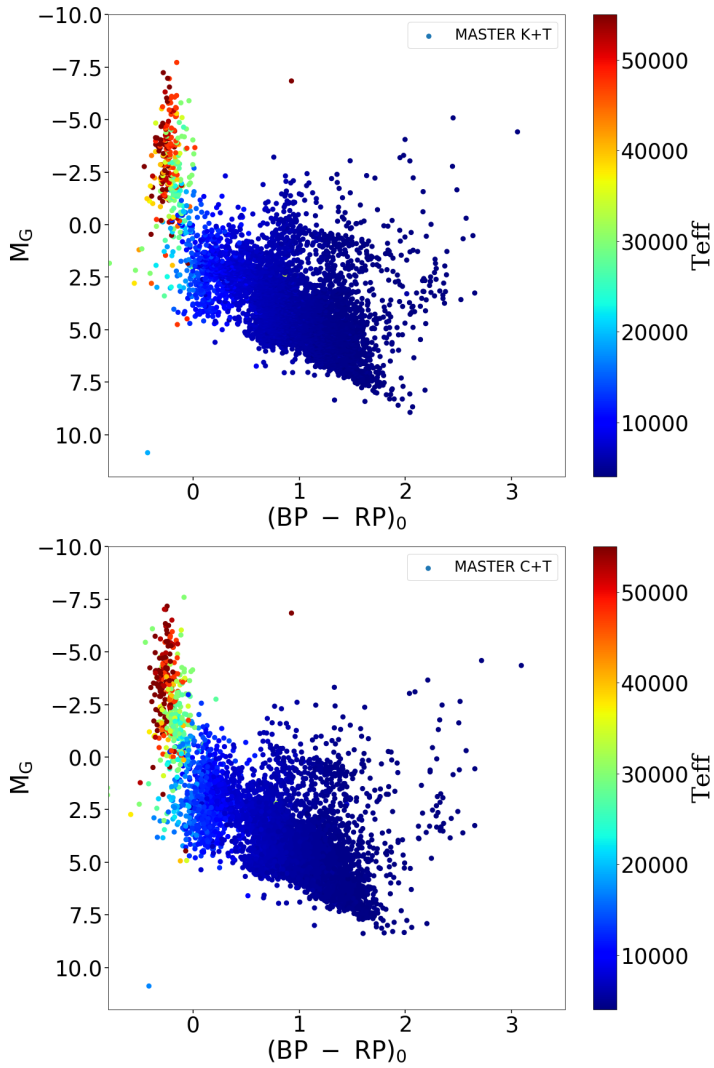


Fig. 7.23 Colour-absolute magnitude diagram for Gaia DR2 using reddening from MASTER, distances from [Bailer-Jones et al. \(2018\)](#) and extinction conversion from [Wang & Chen \(2019\)](#).

In this way, we represent on the top panel of the Figure 7.23 the colour-absolute magnitude diagram, in which we appreciate that OB stars are shown with negative values of M_G for both results with the two set of models. This arrangement in the diagram reflects that they are stars younger than the rest with $M_G > 0.0$, something that is consistent with its spectral type. The greatest differences between the two results can be seen in the number of O stars that are derived using the C+T models compared to the K+T results. In this figure we see how a branch of giants and supergiants appears located at $M_G \sim 0.0$ and $(BP-RP) > 0.8$, more pronounced in the use of models K+T. This effect we already saw in the number of stars of this spectral type in the comparison of the results of the Figure 7.22 for the use of both model sets.

As the main objective of this study, we focus on the Cygnus OB2 region to discuss these results. To do this, we represent the absolute magnitude thus obtained versus the distance, using a colour code according to its extinction $E(B-V)$ in Figure 7.24. These results show how, regardless of the set of models used in MASTER to derive the extinction $E(B-V)$ we use, we obtain a region and extinction increases as we move away, finding a group of young and hot stars at a distance $d \sim 1760$ pc (red line) according to the distance of Cygnus OB2 by recent authors (Berlanas et al., 2019; Wright et al., 2015) that use a spectrometric fitting. Other recent study (Maíz Apellániz et al. 2020, in preparation) uses the two hottest stars included in two clusters in this area, as they are Cyg OB2-8 and Cyg OB2-22, deriving a distance of 1690 pc for Cyg OB2. We also see what seems to be a cloud of gas starting at 900 pcs, which have to be another area where there is a star-forming region.

From both plots we select the stars in the rounded area which is centered in 1760 pc (Berlanas et al., 2019), drawing an absolute colour-magnitude diagram for this region. Figure 7.25 represents the same colour-absolute magnitude diagram from Figure 7.23, drawing different PARSEC MS and MIST PMS isochrones that can give us an idea of the age of this region.

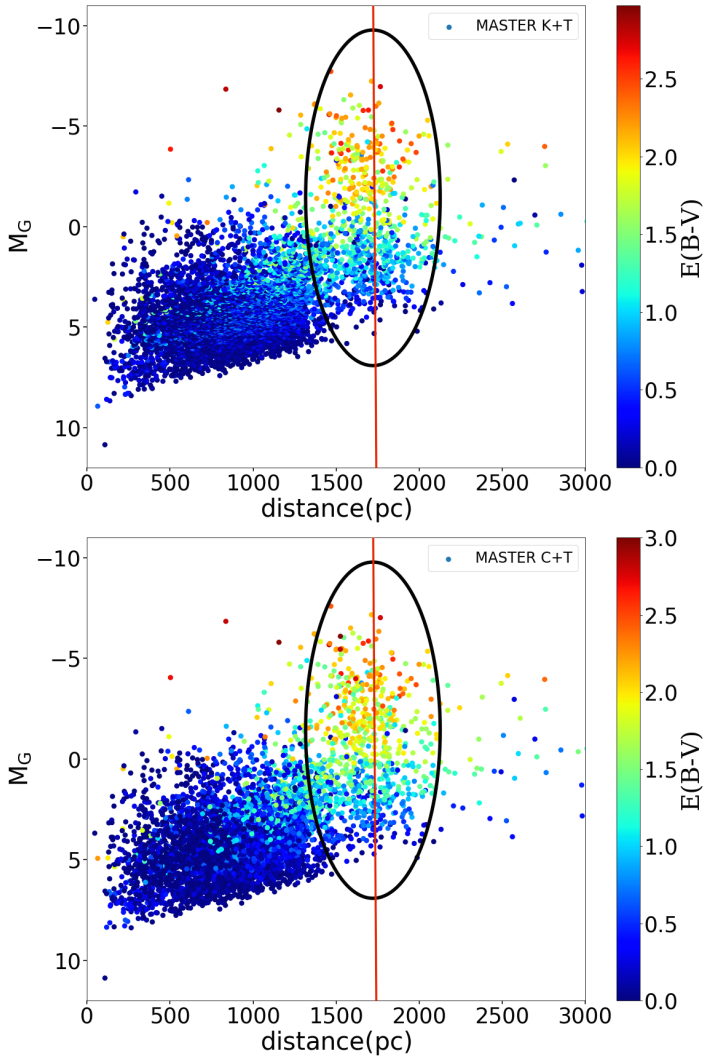


Fig. 7.24 Distance-absolute magnitude diagram for Gaia DR2 using reddening from MASTER, distances from [Bailer-Jones et al. \(2018\)](#) and extinction conversion from [Wang & Chen \(2019\)](#). Red line marks the Cyg OB2 distance from [Berlanas et al. \(2019\)](#).

Figure 7.25 shows in blue dots the subgroup previously selected for Cyg OB2 stars. We also represent both spectrometric catalogues, drawing in red dots the GOSSS common stars and in crosses those common objects from the Wright et al. (2015) library. In this case, green crosses mean those stars within the 2σ from A_V comparison, showing in black crosses those with a difference higher than 2σ . In colour dashed lines we represent those isochrones of PARSEC for ages 1 Myr, 6 Myr and 7.5 Myr. We also represent a MIST PMS isochrone for 0.3 Myr in order to see if we find some of this stars as we referred previously. Attending to our results in blue dots, we find that a group of OB stars with a high intrinsic brightness using C+T, it mixes with the branch of giants or PMS of lower brightness when using K+T. This is directly related to de extinction estimation due to, as we have seen in the A_V differences with Wright et al. (2015), many of them (black crosses) accumulate in this area for the K+T models. On the other hand, the GOSSS catalogue plotted in red dots, shows a high concentration of OB stars in the results with the C+T models, while these points are less accumulated in this part of the diagram, locating in $(BP-RP)_0 \approx 1$. This fact indicates that, depending on the models used for this region, we can derive different absorption values for each star. The use of the K+T models leads us to results with less reddening for a group of stars than C+T, thus deriving lower temperatures. We show this effect in Figure 7.25, where we see a group of OB stars obtained with C + T move towards PMS or MS stars with a lower brightness, somewhat erroneous in view of the results of the GOSSS and Wright et al. (2015) catalogues. If we focus on the position occupied by the common stars with the GOSSS library, we see that most of them are between the isochrones of 6 and 7.5 Myr for the brightest, which is consistent with the ages estimated by previous studies for Cyg OB2 (Berlanas et al., 2018; Comerón & Pasquali, 2012; Drew et al., 2008; Wright et al., 2015). On the other hand, some of these stars are being crossed by the PMS isochrone of 0.3 Myr in both this area and in $(BP-RP)_0 \approx 1$, which is pointing out that, given the star formation region in which we are

studying, we are finding stars that are still in the PMS (Hanson, 2003), both high mass $(BP-RP)_0 < 0$ and low mass $(BP-RP)_0 \approx 1$. In addition, we obtain an average distance of the subgroup associated with Cygnus OB2 for each case, obtaining a distance of 1.65 kpc for K+T and 1.67 kpc for C+T models, which suits better to the one found by Maíz Apellániz et al. (2020).

In both cases, the isochrones that best fit for these groups of Cygnus OB2 stars have a few Myr, as we expected to find in a formation region with a high population of OB stars. Histograms for T_{eff} y $\log g$ that we show in Figure 7.26 shows that not only these are very reddened OB stars, but that this subgroup also has A stars. An interesting result of this comparison is the greater obtention of OB stars from the use of the C+T models, which is totally consistent with the highest extinctions obtained with these models.

In view of the results associated with $\log g$, we see how the vast majority of these Cygnus stars are stars of the main sequence, although there is a non-negligible amount with a $\log g < 4.0$. This set can be classified as giants, but being the star formation region and once determined the age of Cygnus OB2, they can be young stars of PMS, as we have indicated previously.

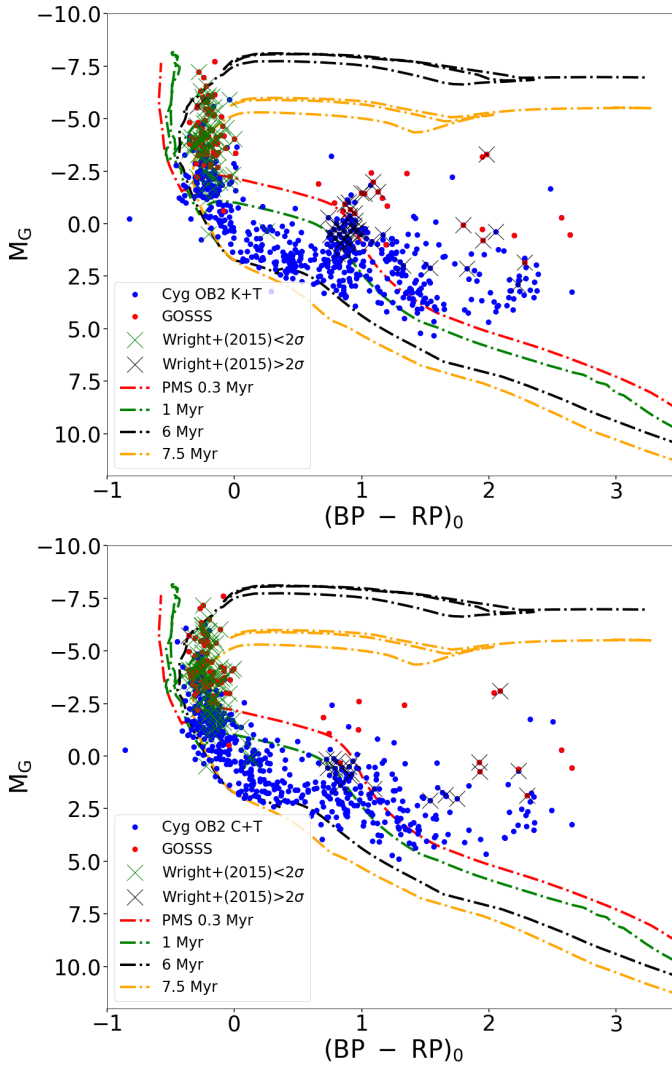


Fig. 7.25 In blue dots we represent the subgroup previously selected for Cyg OB2 stars for this work for our results using the K+T and C+T set models. Both spectrometric catalogues are also plotted, GOSSS in red dots and the [Wright et al. \(2015\)](#) library in crosses. Green crosses mean those stars within the 2σ from A_V comparison, in black crosses those with a difference higher than 2σ . Isochrones of PARSEC (MS) and MIST (PMS) for ages 0.3, 1, 6 and 7.5 Myr are drawn in colour dashed lines.

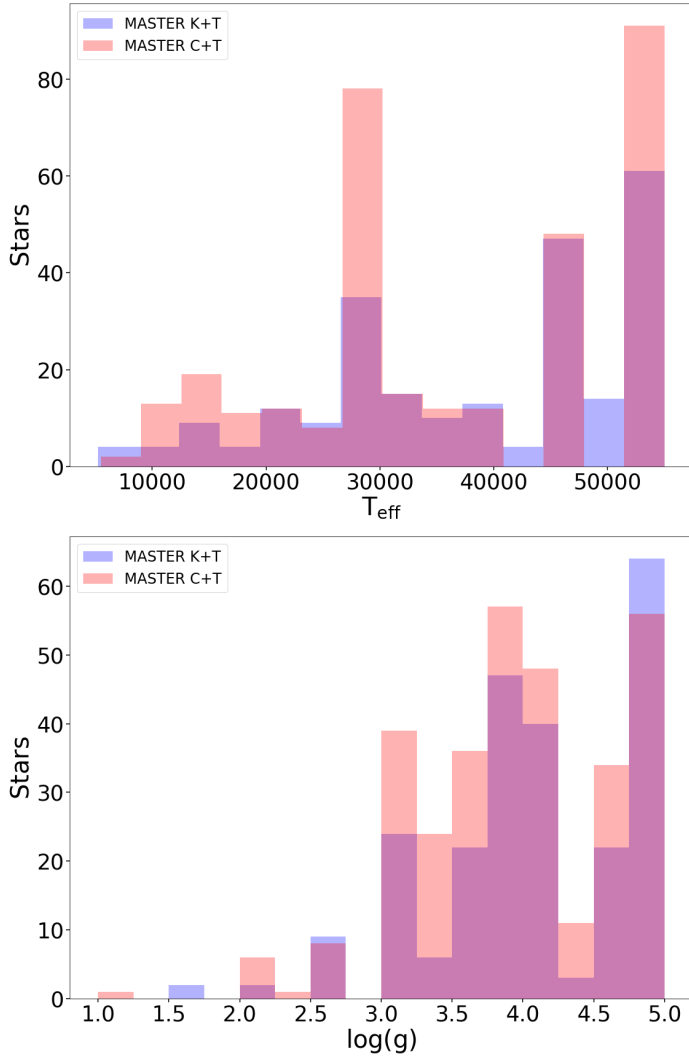


Fig. 7.26 Results of this study for T_{eff} and $\log g$ histograms in Cygnus OB2.

“¿Lo he conseguido Adrian!”

Rocky Balboa. (1979)

8

Summary and conclusions

The work of this thesis covers a wide range of fields. We begin with a new photometric system called GALANTE, making a description and characterization of it using synthetic photometry with 2 observational catalogues (NGSL and MAW) and obtaining the GALANTE transformation equations. We make a preliminary calibration in a small region of Cygnus OB2 before we complete a full 5.6 squared degrees region with a refined calibration. To do this, we develop a GALANTE pipeline in Python using aperture photometry based on IRAF packages. Next, we develop MASTER, which is an algorithm to derive stellar physical parameters from the GALANTE colours using the statistical χ^2 as figure of merit. We apply this method using the NGSL library to test

it, and after analyzing our results with those tabulated from the NGSL, we use MASTER to obtain these properties from observations in Cygnus OB2. According to our study in this thesis, we extract the following conclusions:

- We derive transformation equations from *SDSS* photometry to the GALANTE photometric system (and vice versa). To do this, we use the NGSL and MAW libraries, covering a wide range of T_{eff} , $\log g$, metallicity, and reddening.
- We obtain an rms level of 0.06 magnitudes in the worst case (the bluest GALANTE band), which means that our transformations, despite the noise, can be considered as unbiased.
- We use a single field of our pointing for Cyg OB2 region, obtaining the preliminary ZPs from *SDSS* DR8 and DR12, finding that u and g bands in these releases provide different ZP values.
- We make a comparison between the ZPs obtained from *SDSS* DR12 and *RefCat2*, finding that the distribution of the ZPs derived from *RefCat2* shows a better behavior, with more centralized values and shorter tails (see Figures 4.10 and 4.11). For this reason, we adopt the *RefCat2* ($griz$ bands) as the base catalogue, extending with the *SDSS* DR12 (u band) for the GALANTE calibration. Figure 4.12 shows our preliminar calibration with the Kurucz's fiducial lines corresponding to main sequence and giant stars of solar metallicity.
- We analyse the differences between several theoretical libraries, obtaining discrepancies between them for $T_{\text{eff}} < 10\,000$ K, highlighting a dependence on the catalogue that we use.
- We use the GALANTE normalized colours to test and study, using MASTER, the behaviour of the different models and how to work better

with them to obtain a lower bias in the derivation of physical stellar parameters. We see how the inclusion of this extrinsic parameter has great weight, showing an increase both in the medians of the differences and standard deviations in comparison with the same study carried out without applying extinctions

- Once we tested our methodology with models as input data, we use the NGSL catalogue as observational data in MASTER, using 3 theoretical libraries with extinctions (Kurucz, Coelho and TLUSTY catalogues). We expand these models with a WD library, checking whether our method is sufficiently robust when introducing spectral models that are not catalogued in the NGSL. We conclude that it can introduce some biased results by indistinguishability between the SEDs of MS and WD stars for temperatures higher than 30 000 K, so we will not use these models in our study of Cyg OB2.
- We derive, using aperture photometry, a new ZP calibration for a total of 5.6 square degrees with 6765 stars detected in the Cyg OB2 direction, making a comparison with [Comerón & Pasquali \(2012\)](#). Attending to colours, we obtain a better calibration for $(r-i)$, while we see a colour term in $(i-z)$, using only a linear calibration in GALANTE.
- In [Figure 6.7](#) we represent a bracket diagram with Cyg OB2 in this work represented in blue stars, which is the result of this GALANTE photometric calibration.
- Once we have a calibration for GALANTE, we use MASTER to derive the physical stellar parameters for our catalogue. Comparing the results between the K+T and C+T set of models with 2 spectroscopic catalogues (GOSSS and [Wright et al. \(2015\)](#)), the temperature that we obtain from the latter is always higher than the derived spectroscopically. We obtain better results using the C+T models (see [Table 7.1](#)).

- We can observe that effective temperature and extinction are correlated. Results from both sets of models confirm this fact, deriving a low temperature for a low extinction. Figure 7.11 shows a colour-colour diagram where we can obtain a real B0V star as a F or G spectral type.
- We compare A_V values derived from MASTER with GOSSS and Wright et al. (2015) (Figure 7.12 and Figure 7.17). Regarding these results we conclude that, for a pair of C and K models with the same physical parameters, same colours lead to a different values of stellar parameters.
- We derive similar A_V values for high extinction values comparing with these 2 spectroscopic catalogues, while we are not able to recover the values tabulated by Wright et al. (2015). This is due to degeneracy in temperature and extinction. We also see how Gaia DR2 is using a top value of 10 000 K in their fitting models, so extinction values in the Cyg OB2 are not correct obtaining higher differences in A_V as extinction increases (see Figure 7.10 and Figure 7.16).
- We use the Gaia DR2 catalogue and distances from Bailer-Jones et al. (2018) to characterize our catalogue. We see how a cloud of gas extends from 900 pc to the Cyg OB2 area, as we explain in Figures 7.6, 7.15 and 7.24, deriving a distance for Cyg OB2 ~ 1.65 kpc.
- We also plot in a colour-absolute magnitude diagram all the observed Cyg OB2 stars for GALANTE, comparing with common stars from GOSSS and Wright et al. (2015) catalogues (see Figure 7.25). Here we represent different isochrones, obtaining ages ranging from 6 to 7.5 Myr, but also some PMS younger than 1 Myr. This results is compatible with we expect and that we see in literature, being the Cyg OB2 region an area of star formation with very massive young stars.

References

- Allende Prieto C., 2016, *A&A*, 595, A129
- Allende Prieto C., del Burgo C., 2016, *MNRAS*, 455, 3864
- Andrae R., 2010, arXiv e-prints,
- Andrae R., Schulze-Hartung T., Melchior P., 2010, arXiv e-prints,
- Andrae R., et al., 2018, *A&A*, 616, A8
- Aparicio Villegas T., et al., 2010, *AJ*, 139, 1242
- Aparicio Villegas T., et al., 2011, in *Journal of Physics Conference Series*. p. 012004, doi:10.1088/1742-6596/328/1/012004
- Bailer-Jones C. A. L., 2011, *MNRAS*, 411, 435
- Bailer-Jones C. A. L., Rybizki J., Fouesneau M., Mantelet G., Andrae R., 2018, *AJ*, 156, 58
- Barlow R., 1989, *Statistics. A guide to the use of statistical methods in the physical sciences*
- Becker W., 1946, *Veroeffentlichungen der Universitaets-Sternwarte zu Goettingen*, 5, 159
- Benitez N., et al., 2014, arXiv e-prints,
- Berlanas S. R., Herrero A., Comerón F., Pasquali A., Bertelli Motta C., Sota A., 2018, *A&A*, 612, A50
- Berlanas S. R., Wright N. J., Herrero A., Drew J. E., Lennon D. J., 2019, *MNRAS*, 484, 1838
- Bessell M. S., 2011, *pasp*, 123, 1442

- Blaauw A., 1964, *ARAA*, 2, 213
- Bohlin R. C., 2007, in Sterken C., ed., *Astronomical Society of the Pacific Conference Series Vol. 364, The Future of Photometric, Spectrophotometric and Polarimetric Standardization*. p. 315 (arXiv:astro-ph/0608715)
- Bohlin R. C., Mészáros S., Fleming S. W., Gordon K. D., Koekemoer A. M., Kovács J., 2017, *AJ*, 153, 234
- Bonnarel F., et al., 2000, *AAPS*, 143, 33
- Casagrande L., VandenBerg D. A., 2014, *MNRAS*, 444, 392
- Castelli F., Gratton R. G., Kurucz R. L., 1997, *A&A*, 318, 841
- Cenarro A. J., J-PAS Collaboration J-PLUS Collaboration 2017, in *Highlights on Spanish Astrophysics IX*. pp 11–19
- Cenarro A. J., J-PAS Collaboration J-PLUS Collaboration 2018, *Commissioning and first scientific operations of the wide-field 2.6m Javalambre Survey Telescope*, doi:10.1117/12.2309520
- Cenarro A. J., et al., 2019, *A&A*, 622, A176
- Choi J., Dotter A., Conroy C., Cantiello M., Paxton B., Johnson B. D., 2016, *apj*, 823, 102
- Coelho P. R. T., 2014, *MNRAS*, 440, 1027
- Comerón F., Pasquali A., 2007, *A&A*, 467, L23
- Comerón F., Pasquali A., 2012, *A&A*, 543, A101
- Comerón F., Torra J., 2001, *A&A*, 375, 539
- Comerón F., et al., 2002, *A&A*, 389, 874
- Comerón F., Pasquali A., Figueras F., Torra J., 2008, *A&A*, 486, 453
- Commons W., 2018, *File:Astrology; various constellations. Coloured engraving by S. Wellcome V0024933.jpg* — Wikimedia Commons, the free media repository, [https://commons.wikimedia.org/w/index.php?title=File: Astrology;_various_constellations._Coloured_engraving_by_S._ Wellcome_V0024933.jpg&oldid=303520028](https://commons.wikimedia.org/w/index.php?title=File:Astrology;_various_constellations._Coloured_engraving_by_S._Wellcome_V0024933.jpg&oldid=303520028)

- Covey K. R., et al., 2007, *AJ*, 134, 2398
- Dotter A., 2016, *APJS*, 222, 8
- Drew J. E., Greimel R., Irwin M. J., Sale S. E., 2008, *MNRAS*, 386, 1761
- Ederoclite A., et al., 2017, in *Highlights on Spanish Astrophysics IX*. pp 640–645
- Ekström et al., 2012, *A&A*, 537, A146
- Elmegreen B. G., 2009, in Andersen J., Nordströara m B., Bland -Hawthorn J., eds, *IAU Symposium Vol. 254, The Galaxy Disk in Cosmological Context*. pp 289–300 (arXiv:0810.5406), doi:10.1017/S1743921308027713
- Elmegreen B. G., Efremov Y. N., 1998, arXiv e-prints, pp astro-ph/9801071
- Evans D. W., et al., 2018, *A&A*, 616, A4
- Finkbeiner D. P., 2003, *APJS*, 146, 407
- Fukugita M., Ichikawa T., Gunn J. E., Doi M., Shimasaku K., Schneider D. P., 1996, *AJ*, 111, 1748
- Gaia Collaboration et al., 2016, *A&A*, 595, A1
- Gaia Collaboration et al., 2018, *A&A*, 616, A1
- Golay M., ed. 1974, *Introduction to astronomical photometry Astrophysics and Space Science Library Vol. 41*, doi:10.1007/978-94-010-2169-2.
- Gratton L., 1963, in Gratton L., ed., *Star Evolution*. p. 243
- Gregg M. D., et al., 2006, in Koekemoer A. M., Goudfrooij P., Dressel L. L., eds, *The 2005 HST Calibration Workshop: Hubble After the Transition to Two-Gyro Mode*. p. 209
- Grisoni V., Matteucci F., Romano D., Fu X., 2019, *MNRAS*, 489, 3539
- Guarcello M. G., Wright N. J., Drake J. J., García-Alvarez D., Drew J. E., Aldcroft T., Kashyap V. L., 2012, *APJS*, 202, 19
- Gundlach B. S., et al., 2018, *Scientific Reports*, 8, 11971

- Gustafsson B., Edvardsson B., Eriksson K., Jørgensen U. G., Nordlund Å., Plez B., 2008, *A&A*, 486, 951
- Hanson M. M., 2003, *apj*, 597, 957
- Heap S. R., Lindler D., 2016, in Deustua S., Allam S., Tucker D., Smith J. A., eds, *Astronomical Society of the Pacific Conference Series Vol. 503, The Science of Calibration*. p. 211
- Hosey A. D., Henry T. J., Jao W.-C., Dieterich S. B., Winters J. G., Lurie J. C., Riedel A. R., Subasavage J. P., 2015, *AJ*, 150, 6
- Hu B., Menten K. M., Wu Y., Bartkiewicz A., Rygl K., Reid M. J., Urquhart J. S., Zheng X., 2016, *apj*, 833, 18
- Humphreys R. M., McElroy D. B., 1984, *apj*, 284, 565
- Jeffries R. D., Naylor T., Walter F. M., Pozzo M. P., Devey C. R., 2009, *MNRAS*, 393, 538
- Johnson H. L., Morgan W. W., 1951, *apj*, 114, 522
- Johnson H. L., Morgan W. W., 1953, *apj*, 117, 313
- Johnson H. L., Morgan W. W., 1954, *apj*, 119, 344
- Kenney J., Keeping E., 1947, *Mathematics of statistics*. No. parte 2 in *Mathematics of Statistics*, Van Nostrand, <https://books.google.es/books?id=UdILAAAAMAAJ>
- Kiminki D. C., et al., 2007, *apj*, 664, 1102
- Kiminki D. C., Kobulnicky H. A., Vargas Álvarez C. A., Alexander M. J., Lundquist M. J., 2015, *apj*, 811, 85
- Knödlseder J., 2000, *A&A*, 360, 539
- Koester D., 2010, *MEMSAI*, 81, 921
- Koleva M., Vazdekis A., 2012, *A&A*, 538, A143
- Kuhn M. A., Hillenbrand L. A., Sills A., Feigelson E. D., Getman K. V., 2019, *apj*, 870, 32
- Lanz T., Hubeny I., 2003, *APJS*, 146, 417

- Le Duigou J. M., Knödlseher J., 2002, *A&A*, 392, 869
- Leisawitz D., Bash F. N., Thaddeus P., 1989, *APJS*, 70, 731
- Lin Z., et al., 2017, *apj*, 842, 97
- Lorenzo-Gutiérrez A., et al., 2019, *MNRAS*, 486, 966
- Maíz-Apellániz J., 2005, *pasp*, 117, 615
- Maíz Apellániz J., 2006, *AJ*, 131, 1184
- Maíz Apellániz J., 2007, in Sterken C., ed., *Astronomical Society of the Pacific Conference Series Vol. 364, The Future of Photometric, Spectrophotometric and Polarimetric Standardization*. p. 227 (arXiv:astro-ph/0609430)
- Maíz Apellániz J., 2013a, in Guirado J. C., Lara L. M., Quilis V., Gorgas J., eds, *Highlights of Spanish Astrophysics VII*. pp 583–589 (arXiv:1209.2560)
- Maíz Apellániz J., 2013b, in Guirado J. C., Lara L. M., Quilis V., Gorgas J., eds, *Highlights of Spanish Astrophysics VII*. pp 657–657 (arXiv:1209.1709)
- Maíz Apellániz J., 2017, in *Early Data Release and Scientific Exploitation of the J-PLUS Survey*, held 2-3 October 2017 in Teruel, Spain, Online at <http://riastronomia.es/en/early-data-release-and-scientific-exploitation-of-the-j-plus-survey/> id. 15. p. 15, doi:10.5281/zenodo.1040919
- Maíz Apellániz J., Barbá R. H., 2018a, *A&A*, 613, A9
- Maíz Apellániz J., Barbá R. H., 2018b, *A&A*, 613, A9
- Maíz Apellániz J., Sota A., 2008, in *RMxAC*. pp 44–46
- Maíz Apellániz J., Weiler M., 2018, *A&A*, 619, A180
- Maíz-Apellániz J., Walborn N. R., Galué H. Á., Wei L. H., 2004, *APJS*, 151, 103
- Maíz Apellániz J., Sota A., Walborn N. R., Alfaro E. J., Barbá R. H., Morrell N. I., Gamen R. C., Arias J. I., 2011, in Zapatero Osorio M. R., Gorgas J., Maíz Apellániz J., Pardo J. R., Gil de Paz A., eds, *Highlights of Spanish Astrophysics VI*. pp 467–472 (arXiv:1010.5680)

- Maíz Apellániz J., et al., 2012, in Drissen L., Robert C., St-Louis N., Moffat A. F. J., eds, *Astronomical Society of the Pacific Conference Series Vol. 465, Proceedings of a Scientific Meeting in Honor of Anthony F. J. Moffat*, p. 484 (arXiv:1109.1492)
- Maíz Apellániz J., et al., 2014, *A&A*, 564, A63
- Maíz Apellániz J., et al., 2019a, in *Highlights on Spanish Astrophysics X*, pp 346–352 (arXiv:1810.12192)
- Maiz Apellaniz J., et al., 2019b, *VizieR Online Data Catalog*, p. J/ApJS/224/4
- Mann A. W., von Braun K., 2015, *pasp*, 127, 102
- Marigo P., et al., 2017, *apj*, 835, 77
- Martins F., Schaerer D., Hillier D. J., 2005, *A&A*, 436, 1049
- Massey P., Thompson A. B., 1991, *AJ*, 101, 1408
- McClure R. D., van den Bergh S., 1968, *AJ*, 73, 313
- Mermilliod J.-C., Mermilliod M., Hauck B., 1997, *AAPS*, 124, 349
- Moles M., et al., 2008a, *AJ*, 136, 1325
- Moles M., et al., 2008b, *AJ*, 136, 1325
- Moles M., Sánchez S. F., Lamadrid J. L., Cenarro A. J., Cristóbal-Hornillos D., Maicas N., Aceituno J., 2010, *pasp*, 122, 363
- Oke J. B., Gunn J. E., 1983, *apj*, 266, 713
- Padmanabhan N., et al., 2008, *apj*, 674, 1217
- Pancino E., et al., 2012, *MNRAS*, 426, 1767
- Pearson K., 1900, *The London, Edinburgh, and Dublin Philosophical Magazine and Journal of Science*, 50, 157
- Pietrinferni A., Cassisi S., Salaris M., Castelli F., 2004, *apj*, 612, 168
- Pietrinferni A., Cassisi S., Salaris M., Castelli F., 2006, *apj*, 642, 797
- Prugniel P., Soubiran C., Koleva M., Le Borgne D., 2007, *arXiv Astrophysics e-prints*,

- Reddish V. C., Lawrence L. C., Pratt N. M., 1966, *Publications of the Royal Observatory of Edinburgh*, 5, 111
- Reid M. J., et al., 2014, *apj*, 783, 130
- Rodrigo C., Solano E., Bayo A., Cortés-Contreras M., Jiménez-Esteban F., 2019, in *Highlights on Spanish Astrophysics X*. pp 430–430
- Román-Zúñiga C. G., Alfaro E., Palau A., Hasenberger B., Alves J. F., Lombardi M., Sánchez G. P. S., 2019, *MNRAS*, 489, 4429
- Saito R. K., Minniti D., de Oliveira C. M., 2018, in Chiappini C., Minchev I., Starkenburg E., Valentini M., eds, *IAU Symposium Vol. 334, Rediscovering Our Galaxy*. pp 358–359, doi:10.1017/S1743921317007025
- Sánchez-Blázquez P., et al., 2006, *MNRAS*, 371, 703
- Sánchez N., Añez N., Alfaro E. J., Crone Odekon M., 2010, *apj*, 720, 541
- Smith J. A., et al., 2002, *AJ*, 123, 2121
- Sota A., Maíz Apellániz J., Walborn N. R., Shida R. Y., 2008, in *Revista Mexicana de Astronomía y Astrofísica Conference Series*. pp 56–56 (arXiv:astro-ph/0703005)
- Sota A., et al., 2013, in *Massive Stars: From alpha to Omega*. p. 101
- Sota A., Maíz Apellániz J., Morrell N. I., Barbá R. H., Walborn N. R., Gamen R. C., Arias J. I., Alfaro E. J., 2014, *APJS*, 211, 10
- Straižys V., et al., 2014, *AJ*, 148, 89
- Strömngren B., 1966, *ARAA*, 4, 433
- Tody D., 1986, in Crawford D. L., ed., *PROCSPIE Vol. 627, Instrumentation in astronomy VI*. p. 733, doi:10.1117/12.968154
- Tokunaga A. T., Vacca W. D., 2005, *pasp*, 117, 1459
- Tonry J. L., et al., 2018, *apj*, 867, 105
- Trundle C., Dufton P. L., Hunter I., Evans C. J., Lennon D. J., Smartt S. J., Ryans R. S. I., 2007, *A&A*, 471, 625

- Varela J., Cristóbal-Hornillos D., Cenarro J., Ederoclite A., Muniesa D., Ramió H. V., Gruel N., Moles M., 2014, in Heavens A., Starck J.-L., Krone-Martins A., eds, IAU Symposium Vol. 306, Statistical Challenges in 21st Century Cosmology. pp 359–361, doi:10.1017/S1743921314010746
- Walraven T., Walraven J. H., 1960, BAIN, 15, 67
- Wang S., Chen X., 2019, *apj*, 877, 116
- Weiler M., 2018, *A&A*, 617, A138
- Wright N. J., Parker R. J., Goodwin S. P., Drake J. J., 2014, *MNRAS*, 438, 639
- Wright N. J., Drew J. E., Mohr-Smith M., 2015, *MNRAS*, 449, 741
- Wright N. J., et al., 2019, *MNRAS*, 486, 2477
- Yang K., et al., 2019, *APJS*, 241, 18
- Zhang B., Reid M. J., Menten K. M., Zheng X. W., Brunthaler A., 2012, *A&A*, 544, A42
- de Zeeuw P. T., Hoogerwerf R., de Bruijne J. H. J., Brown A. G. A., Blaauw A., 1999, *AJ*, 117, 354
- van Leeuwen F., 2007, *A&A*, 474, 653

